GROWTH AND CHARACTERIZATION OF THIN AND THICK GALLIUM NITRIDE

By

MICHAEL A. MASTRO

A DISSERTATION PRESENTED TO THE GRADUATE SCHOOL
OF THE UNIVERSITY OF FLORIDA IN PARTIAL FULFILLMENT
OF THE REQUIREMENTS FOR THE DEGREE OF
DOCTOR OF PHILOSOPHY

UNIVERSITY OF FLORIDA

2001

ACKNOWLEDGMENTS

The author wishes first to thank his advisor and department chair, Dr. Timothy J. Anderson, for providing five years of valuable advice and guidance. Dr. Anderson always encouraged the author to approach his research from the highest scientific level.

Secondly, the author wishes to thank the remaining committee members of Dr. Cammy Abernathy, Dr. Steve Pearton and Dr. Fan Ren. As highly respected scientists in the semiconductor field, one could not find better role models for a young scientist to strive towards.

The author cannot overstate how much the daily interactions with Dr. Olga Kryliouk have meant. During the past five years, Olga has played many positive roles in the author's life including instructor, colleague and close friend.

The list of professors, staff and graduate students in the Department of Chemical Engineering and Department of Materials Science and Engineering at the University of Florida who have aided the author is too extensive to list here. However, a few important individuals will be pointed out.

Thanks go to Dr. Mike Kaufman for instructing the author on the theory of TEM and to Dr. Kevin Jones for allowing the author access to his TEM preparation facilities. Another individual who needs recognition is visiting scholar Dr. Vladimir Demin of Moscow State University. In the year they spent working together, Vladimir taught the author to see the beauty in science.

ii

TABLE OF CONTENTS

Abstract of Dissertation Presented to the Graduate School
of the University of Florida in Partial Fulfillment of the
Requirements for the Degree of Doctor of Philosophy

GROWTH AND CHARACTERIZATION OF THIN AND THICK GALLIUM
NITRIDE

By

Michael A. Mastro

December 2001

Chairman: Dr. Timothy J. Anderson
Major Department: Chemical Engineering

The III-nitrides have received considerable attention in recent years for
applications that require a wide band gap semiconductor. Specifically, short wavelength
light emitters are required for full color displays, laser printers, high-density information
storage, and underwater communication. High-temperature and high-power devices are
needed for a number of applications including avionics, automobile engines and future
advanced power distribution systems.

Unfortunately, III-nitride substrates are not available. This dissertation explores
three alternative substrates ($LiGaO_2$, $LiAlO_2$, and Si) for the growth of thick and
potentially freestanding GaN substrates. The requirement to grow a protective layer of
GaN by metal organic chemical vapor deposition (MOCVD) and the need for high rate
deposition by hydride vapor phase epitaxy (HVPE) motivated the development of a
single deposition system capable of growing in both modes.

The successful growth of high quality GaN on LiGaO$_2$ by MOCVD was first demonstrated. Nitridation of the LiGaO$_2$ substrate using NH$_3$ prior to growth leads to the reconstruction of the substrate surface and to the formation of a thin layer of nitrided material having the same orientation as the substrate. It was found that the thick GaN layer grown by HVPE spontaneously separated from the underlying LiGaO$_2$ substrate upon cooling if proper nitridation was performed. This then eliminates the need for substrate removal by HCl etching and gives a reusable template substrate.

The related substrate LiAlO$_2$ is also closely lattice matched to GaN. LiAlO$_2$, however, is more stable, particularly in an HCl ambient making it suitable for thick HVPE growth of GaN.

Finally, it was shown that epitaxial GaN could be fabricated by a low-temperature deposition sequence on silicon substrates. Measurements revealed that a thin compliant SiO$_x$ layer was an effective intermediate layer for the GaN film grown epitaxially on Si. The deposition temperature of 560 ^{o}C is one of the lowest deposition temperatures reported for single crystal GaN by vapor phase epitaxy.

A study of GaN annealed in HCl, H$_2$, NH$_3$ and N$_2$ ambients was performed. It was found that films grown by MOCVD followed a dissociative sublimation mechanism, while HVPE films decomposed to yield liquid gallium.

CHAPTER 1
INTRODUCTION

1.1 Introduction to Gallium Nitride

The III-nitrides have received considerable attention in recent years for applications for which conventional III-V semiconductors cannot be used. Short wavelength light emitters are required for full color displays, laser printers, high-density information storage, and underwater communication. High-temperature and high-power devices are needed for a number of applications including avionics, automobile engines and future advanced power distribution systems [1].

Due to their wide, direct bandgaps and strong, interatomic bonding, III-nitrides are well suited for UV, blue and green light emitting devices and for high-temperature transistors. InN and AlN can be alloyed with GaN, allowing tuning of the bandgaps, resulting in emission wavelengths ranging from the UV to yellow. AlN and GaN contain a low concentration of thermally generated intrinsic carriers due to their wide bandgap making them well suited for high-temperature devices. Additionally, the high melting temperature of GaN allows these devices to function at high temperature although the decomposition temperature for InN is lower than GaN. The high melting temperature also allows high temperature processing but only under high over-pressures of nitrogen due to preferential loss of nitrogen [1].

GaN exhibits a high breakdown field that makes it ideal for high-power devices [2,3]. This high breakdown field (3×10^6 V/cm) of GaN allows for a range of devices not feasible for GaAs (4×10^5 V/cm) or Si (2×10^5 V/cm) based electronics.

The highest reported room temperature electron mobility in a GaN epilayer is 900 cm^2/V-s and the highest mobility reported for an AlGaN/GaN heterostructure is 1700 cm^2/V-s [4]. Both these values are much lower than typical values reported for GaAs (8500 cm^2/V-s) [5,6]. Monte Carlo simulations, however, indicate the saturated velocity of GaN is 3×10^7 cm/sec, which is much higher than either GaAs (1.9×10^7 cm/sec) or Si (1.1×10^7 cm/sec) [7].

1.1.1 Epitaxy

Epitaxy can be classified into three approaches: (1) liquid phase epitaxy (LPE), (2) vapor phase epitaxy (VPE), and (3) molecular beam epitaxy (MBE). VPE and MBE have further sub classifications depending on the sources used (e.g., chloride, hydride, elemental, and/or metalorganic) [8]. The simplest mode for growth is homoepitaxy where the deposited layer is the same as the underlying substrate. The substrate for heteroepitaxy is usually sliced from a larger bulk crystal. For most materials, bulk crystals are not available as is the case for GaN and related materials. In this situation, growth proceeds by heteroepitaxy where the deposited layer has a different composition than the underlying substrate.

1.1.2 Liquid Phase Epitaxy

In LPE, a nearly saturated liquid solution containing the source material is brought into contact with a clean substrate. This is a near equilibrium growth method in which the solution is supersaturated and the driving force for growth is a temperature

gradient. Except for an initial kinetically limited transition, the growth rate is controlled by liquid phase diffusion. LPE is advantageous for three reasons: (1) relatively high growth rates can be achieved (0.1 mm/min), (2) a low growth temperature can be used, and (3) the experimental setup is relatively simple.

Liquid phase epitaxy has been successful for fabrication of GaAs and InP to yield high quality material [8]. A major disadvantage is that LPE is highly sensitive to oxygen contamination and to substrate parameters (misfit, misorientation) making GaN epitaxy difficult. It does offer the significant advantage of lowering the growth temperature and high growth rate for thick film growth. The low solubility of N in liquid Ga, however, has limited its application.

1.1.3 Vapor Phase Epitaxy

In VPE, growth occurs by transport of species in the vapor phase in a high-purity carrier gas to the substrate surface. Molecules deliver atoms to the substrate surface where they are incorporated into the growing film. The absorbed species diffuse on the surface and combine to form a layer. The layer grows by either a step-flow mechanism or coalescence of nuclei forming on the surface [8].

The eight steps of VPE are as follows: (1) transport of precursors to the growth zone, (2) possible homogeneous vapor phase reactions to dissociate precursors, (3) mass transport of vapor phase species from the bulk gas to the substrate surface, (4) adsorption of vapor phase species on the substrate surface, (5) possible heterogeneous reaction of precursor products on the substrate surface, (6) desorption of volatile byproducts from the heterogeneous reaction, (7) transport of volatile heterogeneous reaction byproducts to the bulk gas phase, and (8) transport of volatile homogenous and heterogeneous reaction

byproducts out of the growth zone. Fabrication of compound semiconductor materials is normally carried out in a mass transfer limited regime where step (3) above is the slowest and therefore limiting step. For Si based structures, chemical vapor deposition (CVD) is usually carried out in the kinetic limited regime where step (5) above is the slowest step.

A simple model was developed by Grove in 1965 [8] to describe the growth rate during vapor phase epitaxy. The flux, J_1, across the boundary layer is written as

$$J_1 = h_g(C_g - C_1) \tag{1.1}$$

where h_g is the gas phase mass transfer coefficient, and C_g and C_1 are the concentrations of the species in the bulk gas phase and at the substrate surface. If the limiting surface reaction follows first order kinetics then the flux J_2 at the gas-solid interface is

$$J_2 = k_sC_1 \tag{1.2}$$

where k_s is the surface reaction rate constant. At steady state the fluxes are equal to give

$$C_1 = C_g / (1 + (k_s/h_g)) \tag{1.3}$$

When the reaction is kinetic limited (surface reaction controlled) then $h_g \gg k_s$ and C_1 approaches C_g. This typically occurs at lower temperature. When the deposition is mass-transfer controlled then $h_g \ll k_s$ and C_1 approaches zero. This occurs at high temperature where surface reactions are very rapid. The growth rate is

$$dL_T/dt = J_2/N \tag{1.4}$$

where N is the number of atoms per unit cell ($\sim 5 \times 10^{22}$ atoms/cm^3). With equation 1.4 and eliminating C_1 in equation 1.2 by using equation 1.3, the following expression is reached

$$dL_T/dt = [k_sh_g/(k_s+h_g)][C_g/N] \tag{1.5}$$

This equation can be simplified for the two limiting cases of mass transfer limited and kinetic limited. The mass transfer limited ($h_v \ll k_s$) case simplifies to

$$dL_T/dt = h_v C_v/N \qquad (1.6)$$

And the kinetically limited case ($h_v \gg k_s$) is described as

$$dL_T/dt = k_s C_v/N \qquad (1.7)$$

For the reaction-limited (kinetic) case, assuming the reaction is thermally activated, the surface reaction rate constant is

$$k_s = k_0 \, (-E_s/k_B T) \qquad (1.8)$$

where E_s is the activation energy associated with the step that controls the chemical reaction and $k_B T$ is the thermal energy.

Reactants transport to the substrate surface in the vapor phase. In the simplest model of mass transfer, the reactants diffuse through a boundary layer to reach the substrate. For a horizontal reactor the thickness of the stagnant boundary layer is δ

$$\delta = (\mu x/\rho v)^{1/2} \qquad (1.9)$$

where μ is the absolute fluid viscosity, x is the distance from the susceptor edge to the substrate, ρ is the fluid density, and v is the mass average fluid velocity.

On the substrate surface two mechanisms are involved to produce an epitaxial film: (1) the formation of stable nuclei of GaN on the substrate surface, and (2) their subsequent growth into a continuous film [8]. The probability of formation, p, of a critical size nucleus is

$$p \sim \exp[-\Delta G_{crit}/k_B T] \qquad (1.10)$$

where ΔG_{crit} is the free-energy change associated with the nucleation of a critical size nucleus. For heteroepitaxy, energy is expended in creating hetero-interfaces and

structural defects. The surface of a substrate contains terraces, steps, and kinks. There is a competition between the formation of nuclei on the terraces and the attachment of atoms at the step edges [8]. Three different growth conditions can occur. Layer-by-layer growth occurs when atoms can reach step edges before clustering to form nuclei. (Frank-van-der-Merwe mode). Stranski-Krastanow mode occurs when the layer grows pseudomorphically initially, then non-planar growth develops. If islands develop from the beginning of growth then the growth mode is known as Volmer-Weber.

For heteroepitaxy of thin films, differences in lattice constants and thermal expansion coefficients between the substrate and the epilayer can induce significant strain in the deposited layer. When the thickness of the epitaxial layer is less than the critical thickness, t_c, the misfit strain is accommodated in the epilayer. A compressive stress occurs when the lattice constant of the epilayer is larger than the lattice constant of the substrate. The strain is tensile if the lattice constant of the epilayer is smaller than that of the substrate. When the epilayer thickness exceeds the critical thickness this pseudomorphic strained layer begins to relax by introducing misfit dislocations. Strain influences many properties of nitride semiconductor epitaxial films, including defect formation, mobility and emission wavelength.

Metal organic chemical vapor deposition. Metal organic chemical vapor deposition (MOCVD) is a non-equilibrium growth process that relies on vapor transport of precursors to a heated zone with subsequent reaction of typically group III alkyls and group V hydrides [9]. The chemicals are transported as a dilute vapor to a hot growth zone where pyrolysis of the precursors occurs [10]. The precursor products react on the substrate surface to form GaN for example according to the overall reaction

$$(CH_3)_3Ga^v + NH_3{}^v \rightarrow GaN^s + 3CH_4{}^v \qquad\qquad (1.11)$$

This reaction can be generalized as

$$R_3M + EH_3 \rightarrow ME + 3RH \qquad\qquad (1.12)$$

where M = Al, Ga or In, R = CH_3 or C_2H_5 and E = N. These are overall reactions and do not allow for any intermediate steps that may occur. Pseudobinary alloys $M_{1-x}M_x'E$ may be formed (e.g., $In_{1-x}Ga_xN$) be supplying a second R_3M source to the reaction. The alloy composition, x, is determined by the relative incorporation rates of the two metal elements. This may either be related to the relative diffusion rates or the relative reaction rates according to the previously proposed. Gas phase reactions may occur such as formation of an adduct for the basic R_3M and EH_3 species.

$$R_3M + EH_3 \rightarrow R_3M\text{-}EH_3 \qquad\qquad (1.13)$$

The stability of the complex depends on the strength of the M-E bond. When non-volatile adduct or oligomer products are formed, the carrier gas can be depleted of reactants, resulting in a lowered growth rate.

The deposition process is dependent on the gas velocity and temperature gradients near the substrate. Alkyls are transported from the vapor to the growth interface mainly by diffusion through a boundary zone near the wafer.

Turbulence (non-laminar flow) can form at high gas velocities. Recirculating flows (buoyancy driven convection cells) can develop due to abrupt changes in reactor cross-sectional area or non-uniform temperature gradients. These convection cells can be suppressed by reducing the mass density of the vapor (e.g., using H_2 as the carrier gas), increasing the velocity or by reducing the reactor pressure.

Many reactors operate at low pressure. Low-pressure operation (~0.1 atm) decreases unwanted reactions between precursors by minimizing collision frequency.

The three most common reactor designs are the vertical impinging jet (stagnation point flow), rotating disk and the horizontal reactor with wedge shaped susceptor. For fully developed laminar flow (low to moderate flow velocity) the gas velocity at the walls is zero, and a parabolic profile exists with a maximum velocity at the centerline.
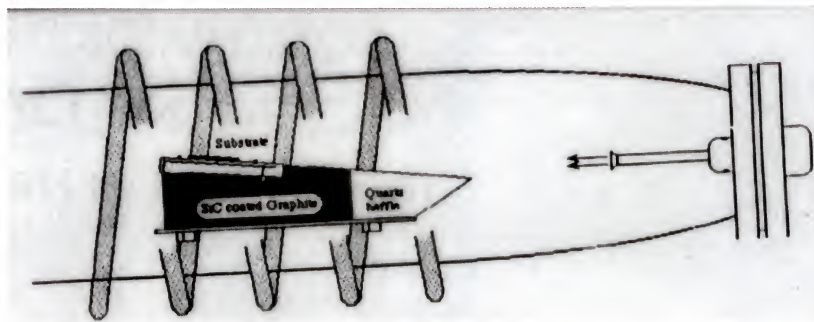
Figure 1-1. Picture of horizontal, cold-wall MOCVD system

Component mass flow rates are controlled with mass flow controllers, and a mixing flow of most often H_2 is used to ensure proper flow profiles and growth rates. The organometallics are stored in stainless steel cylinders (bubblers). A carrier gas bubbles through these cylinders to transport the species to the reactor. The temperature of the bubbler controls the vapor pressure of the organometallics. The most common dopant materials are liquid cyclopenta dienyl magnesium (Cp_2Mg) for p-type GaN, and the hydrides silane or disilane (Si_2H_6) for n-type GaN. The substrate sits on a graphite block called a susceptor. Heat is generated by an RF coil, a resistance heater, or radiatively by use of a strip heater.

Several reaction pathways may occur during MOCVD of GaN. Pyrolysis and diffusion of the group III source through boundary layer is the primary mechanism. Parasitic side reactions such as oligomer formation from the adduct will limit the flux of the group III source to the substrate surface, decreasing the growth rate.

Three growth regimes are observed for GaN MOCVD. The growth rate is limited at typically less than 600 $^{\circ}$C by surface kinetics, and above 1100 $^{\circ}$C by desorption of reactants from the surface. Typically GaN MOCVD is carried out in the mass-transport-limited regime between 850 and 1100 $^{\circ}$C. Diffusion through the boundary layer is approximately independent of temperature; therefore in the mass-transport-limited regime a plateau is seen in the growth rate. The flux of group III elements to the growth interface controls the rate of growth and can be described by Fick's law as

$$J = D(dC_g/dX) \tag{1.18}$$

where D is the diffusion coefficient of the growth species and C is the vapor phase concentration. Solving for flow across a boundary layer (dX = δ) gives

$$J_{Ga} = [D_{Ga}(P^o_{Ga} - P_{Ga})] / [\delta RT] \tag{1.19}$$

where P^o_{Ga} is the input gas stream partial pressure and P_{Ga} is the gallium partial pressure at the vapor-solid interface. Metal-alkyls will undergo complete pyrolysis above 600 $^{\circ}$C; hence $P^o_{Ga} \sim P_{TMGa}$. The input pressure (P_{TMGa}) is much larger than the gallium pressure at the interface ($P_{TMGa} >> P_{Ga}$); consequently the gallium flux is simplified to

$$J_{Ga} = [D_{Ga}P_{TMGa}] / [\delta RT] \tag{1.20}$$

where J_{Ga} is proportional to the growth rate of GaN.

Detailed kinetics of MOCVD. Sun *et al.* developed a fundamental reaction-transport model describing MOCVD of GaN from TMG and ammonia [11]. The kinetics

of adduct formation, decomposition, oligimerization and dissociation are the four essential growth routes that control the composition of the molecules reaching the growth surface. The model was developed at typical MOCVD growth temperatures where surface reactions are rapid so that the deposition processes are diffusion-limited.

The possible significant reactions are listed in table 1-1 and the predicted reaction steps are shown in table 1-2.

To reach the deposition of GaN in step five (table 1-2), the reaction is assumed to be optimized with no unwanted side reactions considered for this model.

Table 1-1. Possible reactions for MOCVD of GaN

Reaction Name	Rxn #	Equation	$k = A_p \exp(-E_a/RT)$	
			A_p (cm^3/mol-s)	E_a (kcal/mole)
Adduct Formation	G1	$TMG + NH_3 \rightarrow TMG:NH_3$	1.0×10^{12}	0
Adduct Decomposition	G2	$TMG:NH_3 \rightarrow TMG + NH_3$	9.5×10^9	19
	G3	$TMG:NH_3 \rightarrow DMGNH_2 + CH_4$	1×10^{13}	32
Oligimerization	G4	$3DMGNH_2 \rightarrow TGNC$	1×10^{21}	0
Product of Oligimerization Decomposition	G5	$TGNC \rightarrow 3GaN + 6CH_4$	4×10^{15}	60

Source: Sun et al. [11]

Table 1-2. Reaction steps for GaN deposition

Step #	Reactions
1	No Vapor Phase Reactions
2	Adduct Formation (G1)
3	Step 2 + Adduct Formation (G1, G2, G3)
4	Step 3 + Oligimerization (G1, G2, G3, G4)
5	Step 4 + Oligimer Decomposition (G1, G2, G3, G4, G5)

Source: Sun et al. [11]

Hydride vapor phase epitaxy. Hydride vapor phase epitaxy (HVPE) has been important in the development of a variety of semiconductors including the III-arsenides, III-phosphides and III-nitrides. Hydride VPE occurs in a hot wall reactor at atmospheric

pressure. The Ga source is gallium monochloride, which is synthesized upstream in the reactor by reacting HCl gas with liquid Ga metal in the temperature range 800 to 900 ^{o}C. The source for nitrogen is ammonia gas, NH_3. Overall, GaN is formed in the growth zone where GaCl is mixed with NH_3 at 900 to 1100 ^{o}C by

$$2Ga^{l} + 2\,HCl^{v} -> 2\,GaCl^{v} + H_2^{v} \qquad \text{(source zone)} \qquad (1.21)$$

$$GaCl^{v} + NH_3^{v} = GaN^{s} + HCl^{v} + H_2^{v} \qquad \text{(deposition zone)} \qquad (1.22)$$

The Ga boat temperature and the flow rate of the HCl control the delivery rate of GaCl.

760 Torr, 900 to 1100 °C
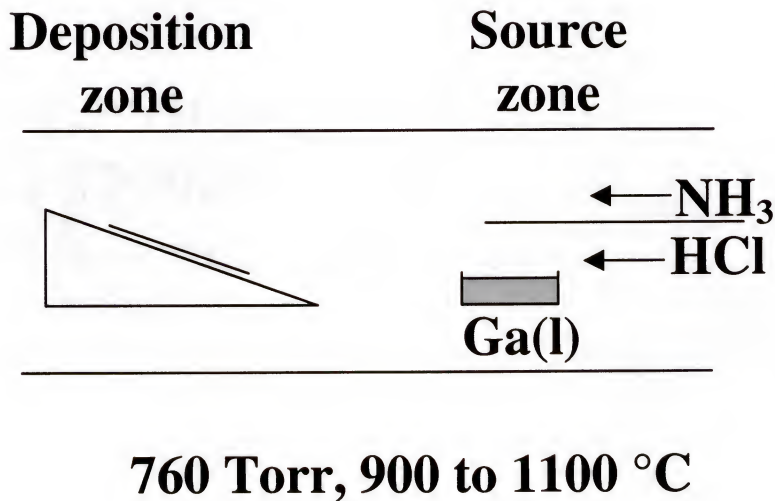
Figure 1-2. Picture of horizontal hot-wall hydride vapor phase epitaxy chamber

A maximum growth rate of up to 100 μm/hr is typically found from 950 to 1050 ^{o}C. A plateau in growth rate vs. temperature is observed in the temperature range from 700 to 1100 ^{o}C indicating a mass-transport-limited regime. In this limit, the growth rate is linearly dependent on the input partial pressure of GaCl and independent of NH_3 partial pressure (excess reactant) over 100 mbar. At lower temperature the growth rate decreases exponentially due to decreasing GaCl and NH_3 pyrolysis, indicating a kinetic-

limited regime [10]. Finally, at higher temperature, in the thermodynamic-limited regime, thermal decomposition decreases the growth rate.

A hot wall reactor with in-situ GaCl synthesis (GaCl + HCl = GaCl + ½H$_2$) is needed because metal chlorides tend to deposit on unheated surfaces due to their low vapor pressure. The substrate holder is maintained at temperatures over 1000 ^{o}C in an aggressive atmosphere making it a source of impurities. Theoretically the chlorine in the HVPE chemistry should segregate most impurities into the vapor phase, rather than the solid film since the metal chlorides are volatile. Nevertheless, silicon and oxygen impurities from the quartz tube (SiO$_2$ + HCl = SiCl$_x$H$_{4-x}$ + H$_2$O + H$_2$) and, leaky seals or contaminated reactants can cause highly n-type films.

NH$_3$ dissociation forms N$_2$ molecules that are extremely stable and considered inert. Gas phase adducts tend to form during HVPE of GaN films causing unwanted vapor-phase reactions, particles and wall deposition. In the HVPE process, large amount of ammonium chloride, NH$_4$Cl, condense on cooler walls and clog exhaust lines.

Detailed kinetics of HVPE. Gallium precursors are produced by these two reactions [12].

$$Ga^l + HCl^v = GaCl^v + \tfrac{1}{2}H_2^v \tag{1-23}$$

$$GaCl^v + 2HCl^v = GaCl_3^v + H_2^v \tag{1-24}$$

Ban estimated that at growth temperatures the efficiency of equation (1-23) is 99.5% [13]. Although ammonia is thermodynamically unstable at high temperature, it was estimated that only 3% of the NH$_3$ molecules decompose into H$_2$ and N$_2$ at 950 ^{o}C [13]. Therefore two overall reactions approximate the deposition of GaN by HVPE.

$$GaCl^v + NH_3^v = \mathbf{GaN^s} + HCl^v + H_2^v \tag{1-25}$$

$$3GaCl^v + 2NH_3^v = 2\mathbf{GaN}^s + GaCl^v + 2HCl^v + 2H_2^v \qquad (1\text{-}26)$$

A more detailed analysis of HVPE was developed by Cadoret [14]. In the model the growth process contains the following steps: adsorption of NH_3 molecules (equation 1-27), adsorption of N atoms decomposed from NH_3 (equation 1-28) and adsorption of GaCl molecules on N atoms (equation 1-29).

$$\text{Surface vacancy} + NH_3^v = NH_3 \text{ (adsorbed)} \qquad (1\text{-}27)$$

$$NH_3 \text{ (adsorbed)} = N\text{(adsorbed)} + 3/2\ H_2^v \qquad (1\text{-}28)$$

$$N\text{(adsorbed)} + GaCl^v = NGaCl \text{ (adsorbed)} \qquad (1\text{-}29)$$
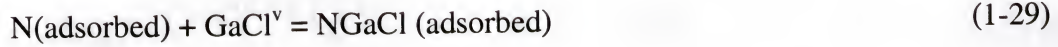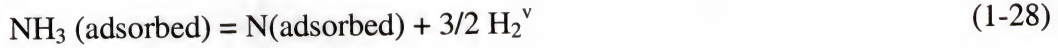
where vacancy is a vacant surface site.
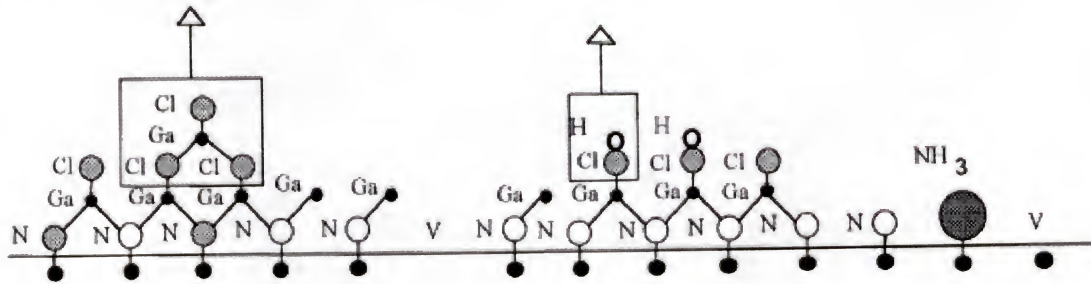
Figure 1-3.   Steps of adsorption and desorption processes involved in the H_2 and $GaCl_3$ mechanisms with schematic representation of impinging and surface fluxes [14]

Two alternate routes for desorption of chlorine are possible as seen in figure 1-3. They are desorption of $GaCl_3$ following absorption of GaCl on two underlying GaCl molecules (equation 1-30 and 1-31) and desorption of HCl following a surface reaction with H_2 (equation 1-32 and 1-33).

$$2NGaCl^s + GaCl^v = 2NGa\text{-}GaCl_3^s \qquad (1\text{-}30)$$

$$2NGa\text{-}GaCl_3^s = 2\mathbf{GaN}^s + GaCl_3^v \qquad (1\text{-}31)$$

$$2NGaCl^s + H_2^v = 2NGa\text{-}ClH^s \qquad (1\text{-}32)$$

$$2NGa\text{-}ClH^s = GaN^s + HCl^v \tag{1-33}$$

The two reactions corresponding to $GaCl_3$ and H_2 growth mechanisms are seen in figure 1-3.

1.1.4 Molecular Beam Epitaxy

Molecular beam epitaxy is a common technique for depositing thin epitaxial structures consisting of semiconductors, metals, and insulators. MBE has the capability of growing device quality layers of semiconductors with atomic resolution. The low growth temperature (300 to 600 $^{\circ}$C) ensures negligible dopant diffusion. The apparatus consists of an UHV cold-wall chamber, independently controlled thermal or e-beam cells to supply the sources, in situ heating and cleaning, and in-situ monitors of growth and chemical analysis.

The simplest method for generating molecular beams is from heated Knudsen cells containing Ga, In, Al, or dopant material. Shutters open to allow the molecular beams to leave the cells and the beams are directed at a heated substrate. Thermal beams of atoms or molecules react on a clean substrate surface to grow an epitaxial film under UHV conditions. The atomic species undergo adsorption and migration on the surface.

Typically, MBE systems are equipped with a number of in-situ probes that monitor the growth in real time. The standard technique is reflective high-energy electron diffraction (RHEED) where high-energy electrons are diffracted off the growing surface and imaged to describe the stages and quality of the epitaxy.

Elemental group V sources can be difficult to control due to variation in vapor pressure between different forms (e.g., P_4 and P_2). An alternative is gas-source molecular beam epitaxy (GSMBE) where hydrides of group V elements are cracked to produce

beams of group V atoms. These gaseous sources do not readily decompose at the substrate. So a thermal cracker is placed in the source stream to decompose the hydride. The advantage of this approach is that the flux (gas flow rate) can be independently controlled from the impinging species composition.

Using a reactive species of N_2 obtained by electron cyclotron resonance (ECR) or radio frequency (RF) plasmas is an alternate to ammonia sources. The plasma is generated by inductively coupling the RF energy into a discharge chamber filled with nitrogen gas to generate N_2, N_2^+ and atomic nitrogen species [1]. Unfortunately this produces highly energetic species that damage the deposited film. A better substitute is to use ECR microwave plasma to produce nitrogen beams at low energies.

When organometallic sources replace the group-III elemental source, the technique is termed organometallic molecular beam epitaxy (MOMBE). The chemical reactions occurring at the growth surface are complex since the organometallics do not pyrolize until the gaseous species reach the heated substrate surface [8]. The variations of MBE are summarized in Table 1-2.

Table 1-2. MBE Classification

Technique	Group III Source	Group V Source
MBE	Elemental	Elemental
CBE (Chemical Beam)	Gaseous	Gaseous
MOMBE	Gaseous	Elemental
GSMBE	Elemental	Gaseous

1.2 Synopsis of the Development of GaN

There has been steady progress in growth techniques to synthesis III-nitride materials. Still, a key issue remaining to commercialize these nitride devices is improving the quality of the epitaxial film. III-nitrides are remarkable in that they

possess large, direct bandgaps and are very stable materials. II-VI semiconductors have produced green light emitting devices but they exhibit extremely short lifetimes due to their chemical and mechanical instability. The polytypes of SiC have indirect bandgaps that make light emission inefficient. III-nitrides are also well suited for high-temperature/high-power electronics due to GaN's high electron saturation velocity, high thermal conductivity and wide bandgap.

In the earliest investigation into GaN powder, Johnson *et al.* converted metallic gallium with NH_3 gas at 1000 ^{o}C by the reaction

$$2Ga^l + 2NH_3^v \rightarrow 2GaN^s + 3H_2^v \qquad (1.34)$$

to produce a black GaN powder [15]. Ejder filled an open sintered alumina boat with Ga and passed a mixture of N_2 and NH_3 to produce whiskers, needles and prisms of GaN on the edges of the boat and on the walls of the surrounding silica glass tube [16]. Juza *et al.* in 1938 passed ammonia over hot liquid gallium to synthesize GaN needles [17]. By this method in 1959 Grimmeiss and Koelmans successfully produced small crystals of GaN [18]. Maruska and Tietjen produced the first large area GaN layers in 1969 by HVPE [19]. Manasevit *et al.* demonstrated the first successful MOCVD growth of GaN in 1975 [20]. In 1981, Gotoh *et al.* first demonstrated reactive MBE growth of GaN [21].

In 1983, Yoshida *et al.* were the first to use a two-step method of growth [22]. Amano *et al.* [23,24,26] and Akasaki *et al.* [25] introduced the idea of an AlN buffer layer to improve the quality of the following epitaxial layer. In 1988, Akasaki and co-workers [25,27-29] demonstrated that by depositing a thin buffer layer of aluminum nitride on sapphire at low temperature before depositing GaN, both the electrical and structural properties were improved. The GaN layer was free of cracks and exhibited a

reduction in the residual electron concentration of approxiamately two orders of magnitude.

Following this, Amano and co-workers made the first p-n junction GaN LED in 1989 [30]. Once high quality GaN was available, progress was made quickly. Nakamura at Nichia commercialized blue and green LEDs starting in 1994 [31]. Nakamura and coworkers reported the first GaN based laser diode in 1996 [32]. By 1999, laser diodes were reported by Nakamura with 10000 hr of continuous operation [33].

1.3 Issues in GaN Epitaxial Growth

The unavailability of sufficiently large (> 1 cm) GaN single crystals for use as substrates for homoepitaxial growth leaves sapphire and silicon carbide as the most popular substrate materials. For growth on sapphire and silicon carbide, high densities of misfit and threading dislocations are observed in the GaN epilayer due to thermal and lattice mismatch. There is a continual push to improve device reliability, and to do so requires improving the quality of the GaN film. Homoepitaxy or lattice matched heteroepitaxy are the two most obvious ways to achieve this goal. Homoepitaxy requires the development of bulk III-nitride crystals.

1.3.1 Bulk GaN

GaN possesses a very high melting point (2791 K) with a corresponding high equilibrium vapor pressure of nitrogen (~4 GPa), which prevents bulk crystals of GaN from being produced by conventional growth procedures such as Czochralski or Bridgman methods in which stoichiometric melts are used. Therefore growth from solution at a lower growth temperature is used. Polish groups have shown promising

results but still have not achieved large size bulk crystals to date. The largest GaN boule they reported to be single crystal was 3 x 2 x 0.2 mm [34].

Another high growth rate technique is a variant of VPE called sublimation sandwich method [35]. GaN films were grown from metallic Ga and activated ammonia on (0001) 6H-SiC or (0001) Al_2O_3. A graphite crucible containing the metallic Ga is positioned facing the substrate and an inductive RF coil delivers heat. Ammonia flow is parallel to the substrate surface and the Ga vapor diffuses across the narrow gap. In the growth range of 1170 to 1270 ^{o}C single crystal GaN is produced with growth rates over 300 μm/hr. The substrate is subsequently etched off to leave bulk free standing GaN.

Freestanding AlN wafers were fabricated at the Ioffe Institute (St. Petersburg, Russia) by HVPE [36]. AlN thick layers were grown on Si substrates by HVPE with growth rates up to 60 μm/hr reported. After the growth of AlN layers, initial substrates were removed resulting in freestanding AlN wafers. The maximum thickness of AlN layer was about 1 mm.

Recently, TDI fabricated 2.5-inch diameter GaN crystals by the melt-solution technique [37]. The crystals were grown in a stainless steel water-cooled chamber in an ambient pressure less than 2 atm with a resistively heated growth zone held at 900 ^{o}C. An x-ray study indicated that the sample consisted of both large grain single crystal regions and highly-textured domains. The FWHM values for ω scan x-ray rocking curves ranged from 13 to 87 arcmin.

1.3.2 HVPE of GaN

Hydride VPE was the first process to epitaxially deposit GaN in 1969 [19]. Until the early eighties, HVPE was the most successful technique for depositing GaN films.

The quality of the available source materials prevented commercialization of this process and the research focus shifted to MBE and MOCVD. Alternatively, HVPE is a promising approach to provide quasi-bulk substrates of GaN [10].

Hydride VPE is a carbon free process allowing growth of high purity films easier than MOCVD. The halogen species removes metal contaminants from the system and prevents the formation of phase-separated Ga droplets. GaCl has fast adatom velocity allowing high growth rates compared to MOCVD. Additionally the chlorine molecule will remove excess metallic Ga preventing the formation of a metal rich film. Thus extremely high ammonia over-pressures are not needed to prevent the formation of Ga droplets as is seen in MOCVD.

The Molnar group first demonstrated that HVPE could produce films on sapphire substrates with excellent structural and electronic properties. The sapphire substrates were pretreated with GaCl and ZnO to wet the surface. Growth rates over 15 μm/hr were observed to produce films up to 74 μm thick. Relatively low dislocation densities yielded electron concentrations of 7×10^{16} cm^{-3} with a high mobility of 845 cm^2/V-sec [38,39].

Attaining high quality nucleation on the substrate is important for growing high quality materials in HVPE as well as other growth techniques. Of all the substrates used for HVPE of GaN including MgAlO$_4$ (spinel), SiC, Si, GaAs, and ZnO (sputter deposited), sapphire has proven to be the most successful. HVPE allows deposition of thick GaN. In HVPE it is difficult to incorporate dopants such as (Mg, Zn) or to deposit the ternary compound AlGaN due to control issues and metal-oxide reactions with the quartz reactor [10]. The decomposition temperature for InN is far below typical growth temperatures, thus requiring extremely high NH$_3$ overpressures to prevent InGaN from

decomposing. Aside from these shortcomings, HVPE and SSM are well suited for preparing n-type substrates for subsequent homoepitaxial growth by MOCVD or MBE [10].

Processing devices on free standing HVPE GaN would improve heat sinking, current injection and allow simpler processing. A ZnO buffer layer on sapphire induces the thick GaN layer to delaminate upon cool down and yield pieces of free standing GaN [38]. Other successful techniques, such as laser ablation and wet or dry etching, to remove the underlying substrate have been developed to yield thick free standing GaN.

1.3.3 MOCVD of GaN

The most common technique for deposition of GaN is MOCVD. MOCVD growth of group III-nitrides involves the transport of gas phase organometallic precursors, hydrides such as NH_3, and carrier gasses to a heated substrate on which the precursors are pyrolysed and the nitride film is deposited [10].

Employing hydrogen as a carrier gas during the pyrolysis of NH_3 causes a high concentration of molecular and atomic hydrogen near the substrate surface. High growth temperature causes rapid decomposition of the organometallic compound and their hydrocarbon ligands. The products of methyl or ethyl radicals can lead to H and C incorporation at the growth front. Yoshida *et al.* found the decomposition point of Me_3Ga in H_2 and N_2 to be 400 and 500 ^{o}C respectively while Et_3Ga in H_2 and N_2 to be 260 and 300 ^{o}C respectively [22]. In both cases, hydrogen reduced the decomposition temperature. The decomposition mechanisms are hydrolysis for Me_3M in H_2, homolytic fission of Me_3M in N_2, and β-elimination for Et_3M in both N_2 and H_2 [10].

The reaction temperature and the reaction mechanism of the metalorganic precursor control the partial pressure of hydrogen, which influences the deposition rate and structural properties of the film. In general, MOCVD films grown in H_2 had smoother surfaces and sharper XRD rocking curves, indicating improved structural quality.

The relatively high thermal stability of NH_3, although still low compared to N_2, requires high substrate temperature, typically greater than 900 ^{o}C for GaN and AlN and more than 550 ^{o}C for InN to sufficiently crack the NH_3. The high growth temperature and resulting high equilibrium nitrogen vapor pressure leads to the problem of nitrogen loss from the Ga_1N_{1-x} film and to carbon contamination from the decomposition of the organic radical during metalorganic pyrolysis. To avoid this, extremely high V/III gas ratios (e.g. > 1000) are employed. Only conventional precursors such as Et_3M or Me_3M are commercially available in the quantity and purity necessary to produce epitaxial films with good structural properties and low impurity concentration to allow control of conductivity and doping [10].

The use of a nitrogen precursor that decomposes at lower temperature is expected to result in a more efficient process and to allow growth of alloys at a lower temperature. The liquid precursor 1,1-dimethylhydrazine has been tested as such an alternative precursor. GaN epilayers were grown on c-plane sapphire using a low V/III ratio [40]. A single source precursor, bisazido dimethylaminopropyl gallium (BAZIGA) has shown promise in producing single crystal GaN at low deposition temperatures [41].

1.3.4 Substrates for GaN

Epitaxial growth of nitrides is difficult due to the non-availability of high-quality, single-crystal GaN substrates or other single-crystal substrates with similar lattice parameters as GaN. Sapphire and SiC substrates are industry standards for epitaxy of group III-nitrides. These substrates are preferred due to their thermal and chemical stability at high temperature, excellent structural and surface morphology, and availability in large volumes. Unfortunately, there is lattice mismatch as well as thermal mismatch between GaN and these substrates. A comparison of available substrates is listed in table 1-3.

Table 1-3. Structural Properties of Various Substrates for GaN Epitaxy

Substrate	E_g (eV)	Lattice parameter a (Å)	Lattice parameter c (Å)	Lattice mismatch (%)	Thermal expansion coefficient (10^{-6} K^{-1}) a	c
GaN – wurtzite	3.36	3.189	5.18	0	5.6	3.17
AlN – wurtzite	6.2	3.112	4.98	2.5	4.2	5.3
6H-SiC – wurtzite	2.9	3.08	15.1	3.5	4.2	4.7
Al$_2$O$_3$ – wurtzite	6.8	4.758	12.991	16.1	7.5	8.5
ZnO - wurtzite	3.35	3.21	5.21	1.94	2.9	4.8
LiAlO$_2$ – tetragonal	6.1	5.1687	6.2679	1.5	7.1	7.5
LiGaO$_2$ – orthorhombic	4.1	5.402	5.007	0.9	6	7
GaN – zinc blende	3.17	4.53		16.57	5.20	
3C-SiC – diamond	2.3	4.36		3.9	2.7	
GaAs – zinc blende	1.42	5.65		19.87	6.0	
Si (111) - cubic	1.12	5.83		20.5	6.2	

Sapphire. For growth of the III-nitrides, sapphire is the most extensively used substrate. Sapphire is available in high volumes of large area crystals that are transparent in the UV and stable at high temperature. Sapphire, however, has a rhombohedral

structure; a hexagonal unit cell that is larger than the basic rhombohedral cell can describe it. The GaN crystal orientation is parallel to sapphire but the unit cell is rotated by 30° about the c-axis with respect to the sapphire unit cell.

Growth of III-nitrides on sapphire occurs by domain matching where integral multiples of lattice constants or major lattice planes match across the film/substrate interface [42,43]. This epitaxial growth habit is dictated by Al-O bonding that results in a 30° in-plane rotation of the nitride lattice with respect to the sapphire substrate [1]. The large lattice mismatch is accommodated by domain matching (7a-Al_2O_3 / 6a-GaN) of the lattice constants, where seven (-12-10) planes of sapphire approximately match six planes (01-10) of GaN [44,45]. The lattice mismatch between GaN and sapphire is so large that the critical thickness is less than a monolayer [46]. Strain is relieved by generation of misfit dislocations. When the initial monolayers are deposited, confined misfit dislocations are generated before the entire substrate is covered with GaN [10]. These dislocations originate at island borders and then start to glide beneath the islands. These confined dislocations lead to a relaxation of the misfit and thermal strain.

It is known that surface nitridation of sapphire, and low-temperature AlN or GaN buffer layers can alter the growth process and film properties. These pretreatments form nucleation layers that limit columnar islands formation and prevent secondary grain growth.

6H-SiC. SiC has several advantages over sapphire. Its lattice mismatch is only 3.5% with GaN and nearly zero with AlN. Large, high-quality SiC substrates are available commercially. SiC has good electrical conductivity and thermal conductivity,

which is important for devices. Presently the high cost of SiC wafers is a major limitation to SiC replacing sapphire as the industry standard.

Alternative Substrates. Several alternative substrates have been used that offer better thermal and lattice matching to GaN. The room temperature lattice constants of wurtzite ZnO (a = 3.32 Å, c = 5.213 Å) are nearly identical to GaN but ZnO is not thermally stable at growth temperature. Cubic 3C-SiC and MgO are both nearly-lattice matched to cubic GaN but growth tends to produce polycrystalline films [9].

Recently a renewed interest has developed in the epitaxy of GaN on Si substrates. The use of Si substrates is desirable because large, inexpensive, high-quality Si substrates are readily available. Unfortunately, between (111) Si and (0001) GaN, a 20.5% lattice mismatch and a large difference in thermal expansion coefficients exist. A thorough review of growth on silicon is provided in section 1.5.

Identifying a high quality substrate thermally compatible and lattice matched with GaN would alleviate many of the difficulties associated with growing device quality material. Two promising materials are lithium gallate, $LiGaO_2$, and lithium aluminate, $LiAlO_2$.

The structure of $LiGaO_2$ is similar to the wurtzite structure but Li and Ga have different ionic radii, thus the crystal has an orthorhombic structure. The (001) face has a hexagonal atomic arrangement that promotes epitaxial growth of (0001) GaN. In fact, hexagonal GaN is nearly lattice matched (0.9%) to orthorhombic (wurtzite-like) $LiGaO_2$.

$LiAlO_2$ substrates possess a small 1.5% lattice mismatch and 21% mismatch in thermal expansion coefficient with GaN [47]. Although $LiAlO_2$ has a slightly larger

lattice mismatch than $LiGaO_2$, $LiAlO_2$ substrates are more stable at elevated temperature. More information on $LiGaO_2$ and $LiAlO_2$ properties is provided in chapter two.

1.3.5 Buffer Layers and Nucleation Layers

GaN deposited directly on sapphire has a rough surface attributable to three-dimensional growth. A major breakthrough occurred in 1986 when Amano *et al.* succeeded in remarkably improving the surface morphology as well as the electrical and optical properties of GaN by first depositing a 50 nm thick AlN nucleation layer on c-sapphire by MOCVD at 600 °C [24]. The following high-temperature MOCVD film of GaN showed a smooth surface (AFM RMS roughness < 1 nm) that was free from cracks and had good structural quality (FWHM of the double crystal x-ray rocking curve (0002) was 110 arc-sec). The low-temperature buffer layer supplies nucleation centers that have the same orientation as the substrate and promotes lateral growth of the GaN film by inducing a decrease in the interfacial free energy between the film and the substrate [10].

This buffer layer provides a high density of nucleation centers that promote lateral growth of the subsequently grown high temperature epitaxial layer. Atomic force microscopy (AFM) showed the buffer layer to proceed in a three-dimensional mode generating columnar films that are coherent with the substrate [1]. This growth mode is advantageous as three-dimensional growth decreases the strain contained in the film. A 20 min anneal at 1000 °C recrystallizes the buffer layer providing a template for epitaxial growth.

Nakamura extended the same concept to GaN buffer layers to produce LEDs [48,49]. The crystal quality of the GaN buffer layer was poor but improved during heating to the growth conditions of the epitaxial layer. Keller *et al.* theorized that the

optimal nucleation layer is a balance between internal defect structure and surface roughness [50]. The nucleation layer allows large grains of GaN to form during the annealing step, giving the GaN epitaxial film a template of strain free GaN.

Additionally, it was found that an initial nitridation of the sapphire surface using NH_3 or N radicals remarkably improved that structural quality of the GaN epitaxial layer [51-53]. By exposing the sapphire surface to a nitrogen plasma at 550 ^{o}C produced in an ECR, Moustakas *et al.* found a relaxed AlN buffer layer formed [54]. It is believed an amorphous layer of AlN_xO_{1-x} forms on the sapphire surface during nitridation that provides a compliant template to remove strain from the next layer deposited [55]. Typically this nitridation is followed by a thin (~20 nm) AlN or GaN buffer layer.

1.3.6 Lateral Epitaxial Overgrowth (LEO)

The accepted technique to attain the crystalline quality needed for laser diodes is lateral overgrowth of GaN by MOCVD. This technique proceeds by partially masking a substrate or seed layer and subsequently regrowing over the masked region. The approach of heteroepitaxial overgrowth is well known and has been shown for GaAs on Si [56,57], InGaAs on GaAs [58], and InP on Si [59]. Similarly, selective epitaxial growth allows the controlled deposition of low-dimensional microstructures such as quantum wires and dots [60,61].

To fabricate an LEO structure, a 0.2 μm GaN layer is grown on (0001) sapphire. Following this a 0.1 μm SiO_2 layer is patterned to form 7 μm-wide SiO_2 stripes separated by 4 μm-wide stripe windows. GaN epitaxy commences again with growth occurring only in the GaN window region. When the thickness of the epitaxial layer exceeds the mask thickness, the GaN film grows laterally over the SiO_2 stripes [1]. As the two

growth fronts meet and coalesce to form a continuous GaN layer, typically 10 μm thick. Threading dislocations propagate horizontally into the overgrown area from the initial seed GaN. As growth continues in the overgrown layer, the threading dislocations do not propagate vertically. The dislocation density in the overgrown area is less than 10^7 cm^{-2}. Since devices are fabricated only in these overgrown areas, the size of the device is limited to the width of the mask.

The GaN deposits selectively within the windows due to the higher sticking coefficient of the Ga adatoms on the GaN surface than on the dielectric mask. It is unfavorable for Ga adatoms to bond to the mask surface due to differences in bond energies [62]. Therefore Ga adatoms attaching to the dielectric would either evaporate or diffuse along the surface until the atom reached the GaN window area. At the initial growth stages, however, nucleation is more rapid at the edges of the window area. Source vapor diffusion over the dielectric region causes the reactant concentration to be higher at the edge of the window region [63].

1.4 Thermodynamics and Phase Equilibria of GaN

Information on the thermochemical properties of the gallium nitride system can provide insight into a number of III-nitride issues including crystal growth optimization and thermal limits during device processing. A brief review is needed on the pressure-temperature-composition (P-T-x) phase diagrams of the group III-nitrogen systems.

Davydov *et al.* [64] calculated the P-T-x phase diagram of the Ga-N system using the CALPHAD (CALculation of PHAse Diagrams) method [65,66]. The T-x projection of a phase diagram with dashed isobaric lines is displayed in figure 1-4. A liquid-liquid

miscibility gap is seen above 2792 K in the Ga-rich melt. The GaN congruent melting

temperature is predicted in figure 1-4 to be 2792 K at a nitrogen pressure of 4.9 GPa.
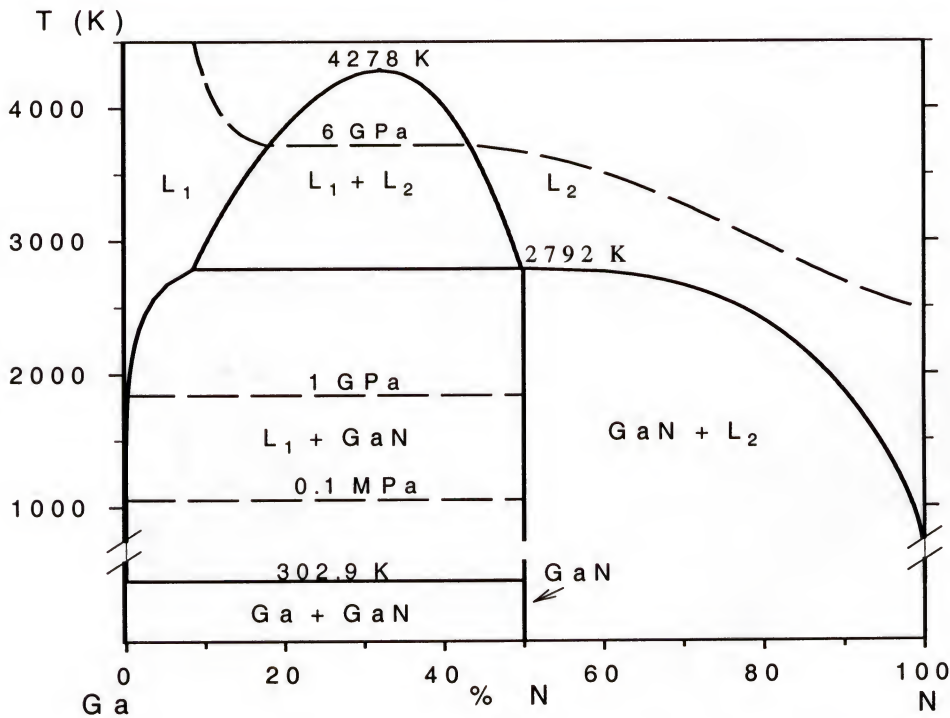
Figure 1-4. Predicted T-x projection of the P-T-x phase diagram with equilibrium
pressure lines of nitrogen (isobaric dashed lines) [64]

Figure 1-5 shows the effect of pressure on the thermal stability of GaN. The

decomposition temperature of GaN is calculated to increase from 1052 to 2791 K for an

increase in pressure from 0.1 MPa to 7.6 GPa. Generally, gallium nitride is

thermodynamically predicted to sublime incongruently into nitrogen-rich vapor and

gallium-rich liquid. At extremely high pressures (P > 4.9 GPa) gallium nitride is

thermodynamically favored to melt congruently (figure 1-5d).

The pressure dependence of GaN thermal stability is exhibited in figure 1-6.

Experimental three phase equilibria (GaN + liquid + vapor) data are displayed in this

figure and the calculated stability limit is seen as a solid line. Clearly from figure 1-6, high nitrogen pressure is needed to prevent GaN decomposition.
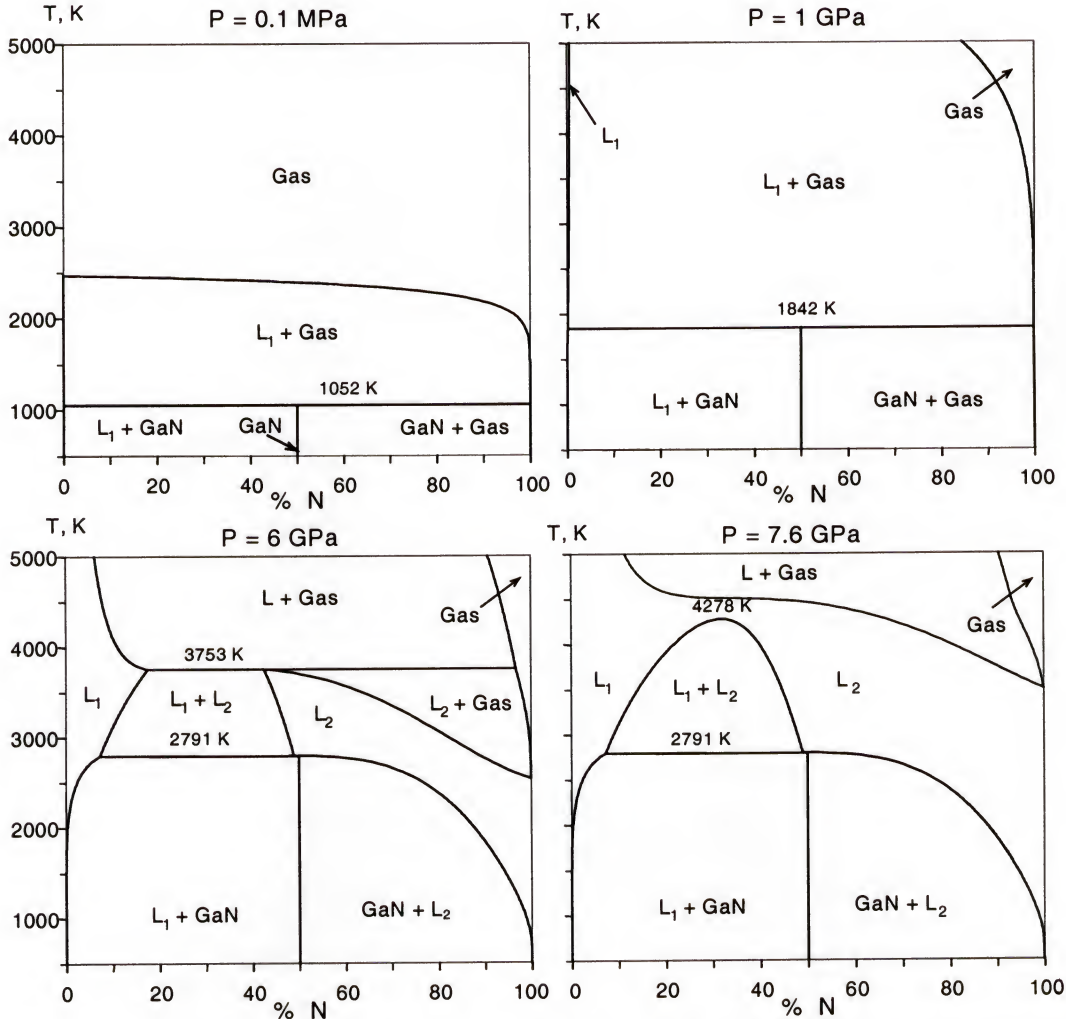
Figure 1-5. Calculated $(T-x)_p$ isobaric sections of the P-T-x diagram displaying the effect of pressure a) 0.1 MPa b) 1 GPa c) 6 GPa d) 7.6 GPa [64]

1.5 Current Status of Epitaxy of III-Nitrides on Si Substrates

Buffer layers. The start of the epitaxial process is crucial to obtain device quality GaN layers. Similar to GaN on sapphire growth, the most studied buffer layer for the growth of GaN on Si is AlN. Direct deposition of a thin GaN or AlN buffer layer on Si,

however, is often impeded by the formation of amorphous SiN_x on the surface [67].

Aside from AlN, several other buffer layers as descried below are currently under

investigation.
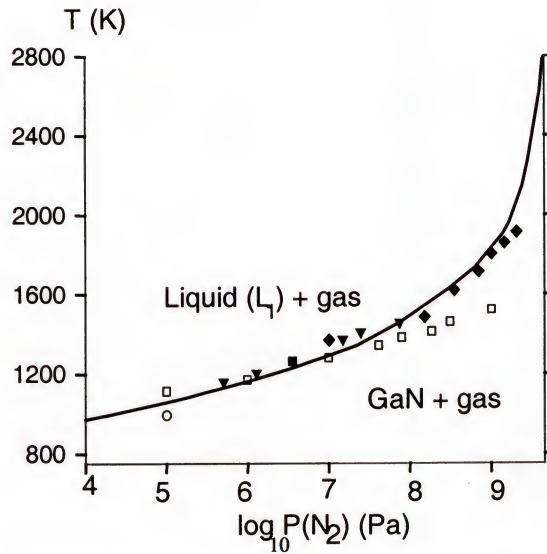
Figure 1-6. GaN thermal stability limit as a function of N_2 partial pressure [64]

AlN buffer layers. Using GSMBE, Nikishin *et al.* grew AlN buffer layers at

1160 K on (111) Si. Once the AlN buffer layer changed to two-dimensional growth, a

thick GaN layer was grown with low dislocation density. Nikishin and coworkers further

showed that a short period superlattice of AlGaN/GaN on the AlN buffer layer blocks

defects from propagating into the GaN epilayer [68].

For samples 1.5 μm thick, the high resolution $\omega/2\theta$ XRD FWHM by was as

narrow as 14 arc-sec. At room temperature, the line width of the GaN exciton

recombination peak was less than 40 meV, typical of the best-grown samples on sapphire

[68].

The layers of GaN grown on Si are known to crack during the cool-down cycle. Cracking occurs along the equivalent <1100> GaN planes and splits the sample into small areas, where the distance between cracks can be as small as 50 mm. Cracking is believed to be an intrinsic phenomenon due to the thermal-expansion coefficient mismatch between GaN and Si. Many studies have shown, however, that cracking of GaN can be completely eliminated by suppressing formation of SiN islands and assuring uniform nucleation of AlN at the Si–AlN interface [69].

Hellman *et al.* studied Si substrates for MBE of GaN and found the Si (111) surface to be advantageous for nucleating AlN because of its inertness and the relative stability of the (7x7) reconstructed surface [70]. AlN nucleated above the (7x7) to (1x1) transition temperature (above 830 °C) is found to contain 30 degree misoriented grains.

Despite the 23.4% misfit in the AlN/Si system, Hellman found that the (7x7) reconstructed (111) surface of Si is excellent for the nucleation of epitaxial aluminum nitride, and films nucleated below the transition temperature are single orientation. Examining the (7x7) surface illustrates that its large unit cell has several sites where extra GaN planes (i.e., edge dislocations) can be accommodated. The 14Si:17GaN match results in a +1.6 degree mismatch, small enough to support lattice matched growth.

Semond *et al.* reported that epitaxy of GaN films on Si (111) substrates by MBE had compact morphologies and flat surfaces [71]. GaN and AlGaN alloys showed two-dimensional growth by RHEED intensity oscillations. Photoluminescence (PL) properties of an AlGaN/GaN QW on Si were similar to PL obtained on equivalent structures grown on sapphire [71].

Semond *et al.* later grew a GaN/AlGaN multiple quantum well (MQW) structure consisting of five undoped GaN QW (30, 20, 15, 10, 5 monolayers (ML)) sandwiched between $Al_{0.20}Ga_{0.80}N$ barrier layers of 10 nm. An 10 K PL spectra of this MQW structure shows that each QW exhibits a clearly resolved emission peak. Compared to emission from a thick relaxed layer (3.471 eV), the 193 and 33 meV blue shifts for the 5 and the 10 MLs GaN QW, respectively, are evidence of the quantum confinement effect. The three other QW PL energy peaks are lower than the band-edge emission energy of the thick relaxed layer. This is attributed to the presence of a strong built in electric field (piezoelectric + spontaneous polarization) [72].

Zhang *et al.* described InGaN/GaN MQW that were grown on Si (001) substrates with specially designed composite intermediate layers (CIL) with single or double GaN/AlGaN(x=0.2) multilayered buffers (MLB) by MOCVD [73]. The CIL consisted of an ultra-thin amorphous silicon film and a single mutilayered buffer (S-MLB).

After thermal cleaning at 1030 °C, hydrogen-diluted silane (SiH_4) was used for depositing an ultra-thin (less than 5 nm) amorphous Si film at 525 °C on the surface of the (001) Si substrate to form a "soft" buffer. Subsequently, a 50 nm thick AlN film was grown on the top of the amorphous Si film, followed by a three-period GaN/AlGaN MLB. The temperature was ramped to 1000 °C and a 300 nm unintentionally doped thick GaN film was deposited. A second CIL was then deposited to produce a double MLB (D-MLB). Finally a six period $In_yGa_{1-y}N$/GaN MQW structure was grown on the surface. Zhang *et al.* also produced MQWs on top of the S-MLB for comparison.

The intermediate layer grown at low temperature provides seed crystals that act as nucleation sites with low orientation fluctuations to promote epitaxy of the III-nitride

epitaxial layers [74]. The double CILs provide more interfaces for the misfit dislocations to terminate than does a conventional single (GaN or AlN) buffer or the CILs with S-MLB.

The InGaN/GaN MQWs on D-CILs gave narrower and enhanced InGaN QW exciton emission and suppressed GaN band edge emission [74]. Excessive amounts of seed crystals with orientation fluctuations were produced if the CILs are thicker than the optimal value thereby decreasing the epilayer quality.

Sánchez-García *et al.* reported GaN:Mg/AlGaN single heterojunction LEDs on Si (111) substrates by plasma assisted MBE (PAMBE) [75]. Optimization of the growth parameters indicated that the initial coverage of the Si surface with a few monolayers of Al was necessary to prevent the formation of amorphous Si_3N_4 at the interface. The surface quality of the GaN grown on the $Al_{.15}Ga_{.85}N$ layer was superior to GaN grown directly on AlN/Si (111). Sánchez-García *et al.* reported that CW intense room-temperature ultraviolet electro-luminescence centered at 365 nm (FWHM of 8 nm) was obtained, under a current injection of 15 mA, a turn-on voltage of 5 V, and an estimated optical ultraviolet output power of 1.5 mW at 35 mA.

ZnO buffer layers. Strittmatter described low pressure (LP)-MOCVD of GaN on silicon (111) substrates using ZnO (10 nm to 40 nm) nucleation layers [76]. Following the ZnO nucleation layer, a thin low-temperature GaN buffer layer was found to improve the GaN crystal quality. Growth of GaN with the ZnO buffer layer without the use of a low temperature GaN buffer layer was not single crystal. The texture of the (0001) ZnO grains was found to directly influence the crystal quality of the GaN layer. The ZnO texture was independent of the Si(111) or Si(100) orientation, allowing for

single crystalline growth on both types of surfaces. TEM investigations revealed that the thin ZnO nucleation layer disappeared during epitaxial growth.

Al_2O_3 buffer layers. Sapphire (α-Al_2O_3) and γ-Al_2O_3 may serve as an insulating layer between the GaN and the Si substrate. AlO_x appears to contain several modifications of Al_2O_3 in an amorphous/fine-grain structure. Results of single crystal α-GaN grown on AlO_x formed on Si(111) are presented below.

Wang *et al.* investigated wurtzite GaN films grown by LP-MOCVD on (100) Si substrates using Al_2O_3 as an intermediate layer [77]. Deposition of the Al_2O_3 film was performed in a separate reactor by the LPCVD method using trimethylaluminium (TMA) and N_2O for source materials. A RHEED pattern had both spots and rings, implying a highly oriented polycrystal. Wang *et al.* determined that the Al_2O_3 was γ-phase, that is a tetragonal distortion of the spinel arrangement. Measurements revealed that the thin, compliant γ-Al_2O_3 layer was an effective intermediate layer for the GaN film grown epitaxially on Si. The reported narrowest linewidth of the $\omega/2\theta$ x-ray rocking curve for (0002) diffraction of the 1.3 μm GaN sample was 54 arc-sec.

GaN buffer layers of 20 nm to 80 nm were prepared between 450 and 600 °C and subsequent epilayer were grown at a temperature of 1000 °C. The GaN films had good adhesion and no films were observed to peel off the substrates although there were mosaic structures on the surface. The γ-Al_2O_3 layer on Si acted as a ''compliant'' substrate, and there is a lower lattice mismatch for GaN on γ- Al_2O_3 compared to the GaN on Si.

The crystallite nuclei in γ-Al_2O_3 provide the template for the GaN buffer layer deposited at low temperature. Because the γ-Al_2O_3 layer remained stable even at high

temperature, the thermal fluctuations of crystallite nuclei in γ-Al_2O_3 were relatively small and the GaN buffer layer was easily crystallized to allow epitaxy on these crystallite nuclei. Thus γ- Al_2O_3 is favorable for nucleation of the GaN buffer layer [78].

Cubic GaN on cubic buffer layers. While a cubic epitaxial relationship exists for GaN on (100) Si, single crystal growth is impeded by the growth of Si_xN_y inclusions at the interface, which act as nucleation cores for the formation of the more stable hexagonal GaN phase. GaN condensing on Si covered with Si_xN_y does not experience an epitaxial constraint and thus grows in its hexagonal modification with some cubic grains. Further growth leads to largely columnar growth of hexagonal GaN that rapidly overgrows the initial cubic GaN grains. This phase transformation is unavoidable unless the Si surface is protected against impinging nitrogen [79]. A possible cubic template that avoids the formation of Si_xN_y inclusions is a thin cubic GaAs or SiC insertion layer.

GaAs buffer layers. Yang *et al.* reported the use of GaAs buffer layers to prevent the formation of Si_xN_y during growth of GaN films on (001) Si substrates by PA-MBE [80]. GaN films grown on this GaAs/Si(001) structure were predominantly cubic and exhibited the characteristic band-edge photoluminescence of cubic-GaN up to room temperature. The PL efficiency from these samples, however, was low compared to that of cubic-GaN layers directly grown on GaAs(001). Yang explained the lower PL efficiency by the presence of additional structural defects. The high dislocation density in the films was attributable to epitaxy of polar materials on nonpolar substrates and the metastable nature of cubic GaN.

SiC buffer layers for SOI. To minimize the structural and thermal mismatch, SiC is an ideal substrate for GaN as it can be grown on Si substrates or silicon-on-

insulator (SOI) substrates. Incorporation of high quality GaN, SiC, and Si layers together could result in a new generation of heterojunction devices.

The electrical advantages of the Si SOI structure (e.g., absence of latch up, reduced parasitic capacitance, shallow junctions) can hopefully be transferred to SiC SOI devices. In addition, the relatively plastic oxide layer is beneficial in absorbing stress and dislocations.

By itself, hexagonal 6H-SiC has a smaller lattice mismatch (~3%) than Si, and in principle is a more suitable substrate, but SiC is available only in small diameters and is very expensive. Therefore the fabrication of SiC SOI structures is desirable for large area, low cost substrates for GaN growth.

Steckl and co-workers constructed a Si SOI structure consisting of a thin Si (111) device layer (900-1000 Å), a 1 μm SiO_2 layer and a (100) substrate [81]. The orientation of the Si (111) layer was tilted 2.4 to 4° off axis. The Si SOI was produced by thermal bonding and etch back. The final step involved a specialized plasma etching process [82] to provide the Si with high uniformity over the entire wafer area. Growth on the (111) plane was chosen for two reasons: (a) superior results with growth of 3C-SiC directly on (111) Si substrates [83] and (b) the (111) SiC surface, which is essentially identical to the c plane of 6H-SiC, is a better match for subsequent growth of III-N films.

A similar approach to obtain high quality GaN on Si and SiC-on-SOI by MBE was investigated by Yang *et al.* [84]. Due to the large difference in chemical bond strength between Si-N (9.5 eV) and III-N (e.g., Al-N, 2.98 eV), it is easier to form amorphous silicon nitride on the Si substrate surface than GaN or AlN. To avoid the formation of silicon nitride a thin layer of Al was first deposited before introduction of

the nitrogen plasma. The MBE growth sequence was a nucleation layer of 10 nm of AlN at 500 °C followed 0.3 μm of GaN at 740 °C. The GaN film exhibited no cracking but the film had a broad ω/2θ HRXRD FWHM of 25 arcmin.

Silicon nitride buffer layers. Nakada and Aksenov reported growth of wurtzite GaN films grown by RF-PAMBE on silicon nitride buffer layers formed on Si (111) substrates [85]. Measurements indicated that the single crystalline wurtzite GaN grown on buffer layers (amorphous SiN_x) took the following relationship with the substrate: GaN(0001)//Si(111) and GaN (-1-120)//Si(1-10). The silicon nitride buffer layer was found to be flat and sharp when the thickness of the buffer layer was approximately 1.5 nm. For this film, efficient-bound exciton emission was observed at 3.46 eV.

When silicon nitride was formed on the Si (111) surface by nitridation at 950 °C, a mixed layer of the single crystalline and amorphous silicon nitride was formed. When the Si (111) was nitrided at a lower temperature, only amorphous silicon nitride was formed. Auger (AES) measurements showed that the composition of silicon nitride formed at 700°C is Si_3N_4, whereas the silicon nitride formed at 950 °C is SiN. The observed difference in the composition of the silicon nitride layer is caused by a higher desorption rate of nitrogen species from the growing surface at 950 °C than at 700 °C.

Nakada *et al.* stated two mechanisms allowed single crystal wurtzite GaN to grow on the partly amorphous silicon nitride buffer layer. First, since some portions of the silicon nitride buffer layer crystallized, the crystal orientation of the Si substrate is transferred to the grown GaN layers through the crystallized areas; and second, if the short-range tetrahedral coordination of each atom is maintained, the short-range order may retain the epitaxial relation [85].

Lateral epitaxial overgrowth. LEO is a promising method to obtain GaN-based material with reduced dislocation density (i.e., less than 10^7 cm^{-2}). The most successful application of LEO is on basal plane sapphire. LEO on (0001) Al_2O_3 has been successfully used to reduce dislocations and enhance lifetimes in GaN-based laser diodes. Because LEO can be applied to any substrate, it is important to investigate the possibility of GaN LEO on Si substrates due to its current commercial and technological potential [86].

Recent studies have shown that the density of threading dislocations (TDs) is reduced by 3 to 4 orders of magnitude in the LEO material grown on 6H-SiC and sapphire substrates [62,63]. Studies on the optical properties of LEO GaN and InGaN quantum wells have revealed that TDs in these films act as non-radiative recombination centers. Fortunately, the minority carrier diffusion length is less than 200 nm, which is smaller than the average distance between TDs in overgrown GaN. The emission mechanisms of the carriers that do recombine radiatively appear to be unaffected by moderate TD densities ($\sim 10^6$ cm^{-2}) [87-92].

Marchand investigated LEO on (111) Si by depositing a 60 nm or 180 nm AlN buffer layer followed by a 200 nm-thick, 5 μm-wide stripes of SiO_2 oriented to GaN in the <1-100> direction [93]. The widths of the mask regions were 35 μm. The surface morphology of the samples measured by AFM indicates that the overgrown regions are free of step terminations, which indicates that the density of screw-component TDs at the surface of the LEO GaN is markedly reduced compared to the seed regions. For the LEO region, screw component TD density at the surface of LEO GaN was 3×10^6 cm^{-2} [93].

The arrangement of the depressions suggest that the GaN in the seed region has a columnar structure with a grain size on the order of 0.2 μm, which is typical for GaN films grown on unpatterned AlN/Si(111) substrates [93].

Pendeo-Epitaxy. The Davis group developed an approach where GaN growth is forced to selectively begin on the sidewalls of a tailored microstructure comprised of forms previously etched into the seed layer [94]. Pendeo-epitaxial growth continues until coalescence over and between these forms results in a complete layer of low defect-density GaN. This is accomplished in one regrowth step, eliminating the need to align devices or masks for the growth of a second layer. Results indicate that the ability to grow GaN by pendeo-epitaxial on silicon substrates is a promising alternative.

Future of growth of GaN on Si. This review has focused on promising techniques available for MOCVD of III-nitrides on Si(111) or Si(100). The benefits of incorporating GaN into Si technology are obvious particularly for cost reduction and the possibility of integration with existing Si technology. The choice of technology is dependent on the quality of GaN needed to meet the device demands. As GaN processing advances, GaN growth on Si is expected to be similar to current GaN/sapphire technology. For GaN LEDs and simple pseudo-GaN substrates grown on Si substrates, an AlN buffer layer should provide sufficient quality GaN. GaN/Si LEDs may require GaN/AlN multi buffer layers to improve the film quality. GaN/Si laser devices will need to employ ELO to obtain the necessary crystal quality. Many GaN based electronic devices such as FETs, need the development of an insulating buffer layer on Si. The achievement of GaN layers with surface areas limited only by the size of the available silicon substrates is now conceivable.

1.6 Polarity

Wurtzite III-nitrides do not possess a center of inversion. Thus the crystal exhibits crystallographic polarity. The geometric structure factor is different in opposite directions of the polar axis. A (Ga) or B (N) face of GaN may be identified by x-ray scattering or by convergent beam electron diffraction. Also, based on differences in chemical properties other techniques have been developed to delineate the polarity of wurtzite nitride structures. Growth, etching, defect generation, and piezoelectricity, among other properties depend on the polarity of the material [95].

1.6.1 Comparison of Polarity Literature

GaN typically grows in the thermodynamically stable wurtzite structure. Similar to many compound semiconductors, GaN is typically grown along a polar axis. The growth of this hexagonal crystal proceeds normal to the {0001} basal plane, where the atoms are arranged in bilayers of alternating Ga and N hexagonal layers. Alternating the anion and cation layers induces onto the bilayer a polarity of either Ga-face or N-face (figure 1-7). Ga-face indicates Ga on the top position of the Ga/N bilayer. Whereas a semiconductor may be terminated by a single monolayer, polarity implies a bulk ordering in the orientation of alternating layers of anions and cations [96]. Thus a crystal may be terminated by a row of N atoms and still be of Ga-face polarity. The typical notation is to indicate the [0001] direction as a vector pointing from a Ga atom to a nearest neighbor N atom. Wurtzite GaN nearly always grows either [0001] Ga-face or [000-1] N-face. Various techniques have been used to identify the polarity of GaN grown under various conditions [96]. A brief description of these techniques is provided below.
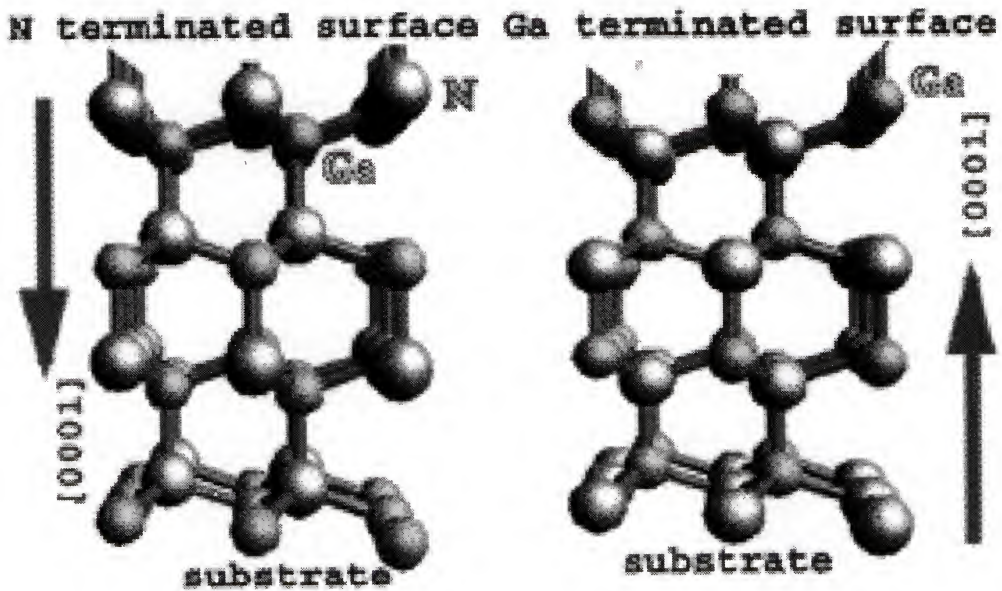
Figure 1-7. Alternating anion and cation layers induces onto the bilayer a polarity of Ga-face or N-face [96]

Several groups attempted to use AES or XPS to determine the polarity of GaN [97-99]. As AES and XPS are surface techniques, it is inconclusive as whether these measurements were determining polarity or termination. Groups at Lawrence Berkley Lab and Xerox, as well as the University of Bristol, first approached the determination of the polarity of GaN by the use of TEM [100,101].

Ponce *et al.* examined MOCVD growth of GaN with a GaN buffer layer and determined the smooth film to be Ga-face, while films grown without the buffer layer were N-face. N-face GaN was found to form hexagonal pyramids with mesas containing inversion domains.   Ponce *et al.* showed that the smooth facets in single crystals correspond to the {0001}, Ga-terminated, lattice planes, whereas the rough facets correspond to the {0001}, N-terminated, planes. Generally, MOCVD GaN retains the polarity of the substrate [101].

An initial pre-nitridation or a low-temperature buffer layer growth is used to establish the polarity of the surface [102]. This step is typically followed by a high temperature anneal which establishes that the surface of the substrate is covered completely with cation-face nuclei, ensuring smooth Ga-face GaN epitaxy.

Vermaut *et al.* determined that Ga-face GaN grows on Si-face 6H-SiC and that N-face GaN grows on C-face 6H-SiC. Similarly In-face InN grows on Si-face 6H-SiC and N-face InN grows on C-face 6H-SiC [103].

Similar results, in terms of the role of substrate polarity on film quality and on the polarity of the epitaxial film on sapphire, were reported for SiC [103], ZnO [104,105] and GaAs [106-108].

A straightforward technique used to reveal the orientation of the polarity of GaN is simply to study its chemical properties. Sasaki *et al.* found that rough MOCVD films oxidize rapidly as compared to smooth GaN films [109]. Weyher *et al.* studied the etch rates of MOCVD films in KOH and NaOH [110]. The rough films with hexagonal crystallites tended to etch much more rapidly than did the smooth films. The hexagonal pyramidal hillocks were reported to be the polar (10-11) and (10-1-1) surfaces [111].

This agrees with the earlier findings of Nowak *et al.* who studied bulk GaN and found the N-face to be less stable than the Ga-face [112]. The best results of bulk GaN growth have been seen when the N-face is in contact with the Ga solution, and the Ga-face is exposed to a nitrogen rich atmosphere [112]. Sun *et al.* have shown through surface stability measurements that when bulk crystals are exposed to the opposite conditions the crystal quality deteriorates [113]. Limited work has been done on MOCVD growth on GaN bulk substrates [114].

Hellman *et al.* reported on MBE growth using RHEED to analyze the influence of polarity on surface structure [104]. Typically RHEED patterns of the GaN surface show a (3x3) reconstruction for N-face, while a (2x2) reconstruction is seen for the Ga-face. For MBE, the growth rate is usually less when the (3x3) reconstruction is seen because there is a high decomposition rate of N-face GaN at the high growth temperature and ultra high vacuum condition of MBE.

Rapcewicz *et al.* performed calculations using first principles to predict the arrangement of the GaN surface during growth [115]. It was found that the ionic character of the Ga-N bond and the strength of the N-N bond strongly influence the surface reconstructions observable during MBE growth. They predicted that under gallium-rich conditions, a gallium-adatom reconstruction is energetically favored. In contrast, under nitrogen-rich conditions, a nitrogen-adatom reconstruction is favored [115].

X-ray Standing Wave (XSW) measurements were used to determine the polarity of GaN grown by MBE on sapphire [116]. XSW combines the structural sensitivity of x-ray diffraction with the chemical elemental sensitivity intrinsic to x-ray spectroscopy. Although XSW is a powerful technique, access to a synchrotron light source is required.

1.6.2 Spontaneous and Piezoelectric Polarization

Depending on the type of substrate, initial nucleation, and growth and annealing conditions, the strain contained in an epitaxial film can be either compressive or tensile. This interfacial stress induces a piezoelectric field normal to the surface. Additionally the wurtzite structure of GaN causes a spontaneous polarization, which combines with the piezoelectric field to induce a total polarization ($P_{tot} = P_{pe} + P_{sp}$).

Components of both spontaneous and piezoelectric polarization result from the symmetric wurtzite structure. The piezoelectric tensor has three independent non-vanishing components for the crystal structure of GaN. For the III-nitrides the absolute values of these piezoelectric constants are up to ten times larger than in conventional II-VI and III-V compounds. The direction of spontaneous polarization is determined by the crystal structure whereas the piezoelectric polarization direction is dependent on the crystal structure as well as whether the material is under tensile or compressive stress. Even at zero strain, where the piezoelectric polarization is zero, the spontaneous polarization of III-nitrides is still large.

Both spontaneous and piezoelectric polarization generate electric fields that influence the shape of the band edges and the carrier distribution. Thus the spontaneous and piezoelectric fields influence the electrical properties of transistor structures and the radiative recombination in light-emitting devices. A simple illustration of this effect is that the Ga-face $Al_xGa_{1-x}N$/GaN interface has an enhanced 2-dimensional electron density [117]. Still, compensating defects and impurities can reduce the polarization-induced electric fields in films with high carrier concentration [118].

Karrer *et al.* studied the influence of spontaneous polarization on GaN devices through band bending of the conduction and valence bands. The observed behavior was predicted theoretically by analyzing derivations of the Schrödinger-Poisson equations [118].

Experimentally, Karrer *et al.* found that the polarity of PAMBE GaN films could be selected by the deposition of a thin AlN nucleation layer. MBE growth of GaN on oxygen terminated sapphire substrates is found to have N-face polarity. The spontaneous

polarity points from the substrate towards the surface while a biaxial compressive strain orients the piezoelectric polarization in the opposite direction. The large spontaneous polarization dominates the total polarization inducing a negative bound sheet charge at the GaN surface and a positive bound sheet charge at the GaN/substrate surface [118].

Pre-depositing an AlN buffer layer before GaN growth causes the orientation of the piezoelectric and spontaneous polarization to be flipped. This leads to the opposite result of a positive bound sheet charge at the GaN surface and a negative bound sheet charge at the GaN/substrate surface. This positive bound sheet charge at the surface is partially compensated in n-type GaN by free electrons [118].

Karrer *et al.* found that if the polarization charge at the surface is not completely compensated, an enhancement/lowering of the electron affinity, χ_s, occurs at the N-/Ga-face surface. This in turn influences the Schottky barrier height, which is the difference between χ_s and the work function of the metal, Φ, found at the metal-semiconductor interface [119].

Karrer *et al.* measured the influence of different barrier heights from Pt contacts on Ga-face and N-face n-type GaN by I-V and C-V measurements. It was found that the Ga-face diodes had better performance than the N-face diodes due to higher Schottky barriers (1.1 for Ga-face vs. 0.9 eV for N-face GaN) and lower reverse currents. The difference in the electronic behavior was due to the difference in the spontaneous polarization [118].

1.7 Thermal Stability of GaN

Group III-nitrides are well suited for high power and high temperature applications due to their large metal-nitrogen bonding energies. It is important to

understand an upper limit of stability for group III-nitrides for growth and processing, as well for device operation.

Johnson *et al.* gave the first description of GaN decomposition in 1932 [120]. It was reported that heating GaN to elevated temperature resulted in the production of liquid gallium and nitrogen vapor. Searcy in 1964 reported congruent vaporization of GaN into nitrogen and gallium vapor [121].

Schoomaker *et al.* determined by a torsion-effusion method that the vaporization coefficient for the decomposition is much less than unity [122]. Comparatively they found that the addition of liquid gallium to the system markedly increased the decomposition rate [122].

Thurmond *et al.* [123] and Logan *et al.* [124] first studied the decomposition of GaN in hydrogen ambient. Liquid gallium and ammonia vapor were reported to be the products of decomposition. This reaction is believed to be close to the calculated thermodynamic equilibrium judging from the close agreement to the measured ammonia and hydrogen partial pressures. Similarly, Jacob *et al.* measured the decomposition temperature for GaN as 970 °C in Ar/N_2 and 600 °C in H_2 [125]. Ambacher *et al.* measured the nitrogen flux upon GaN decomposition with a quadruple mass spectrometer [126]. From analysis of the time evolution of this flux, an activation energy of 379 kJ/mol was calculated for the reaction $2GaN^s \rightarrow 2Ga^v + N_2^v$.

Fortado and Jacob found that GaN was stable when annealed in nitrogen for 30 min at 1070 °C. Conversely, hydrogen anneals at 950 °C resulted in the formation of liquid gallium droplets on the surface [127]. Koleske *et al.* [128] and Pisch *et al.* [129] confirmed the enhanced decomposition of GaN in the presence of liquid gallium.

Hong *et al.* studied the stability limits of powdered nitrides using rapid thermal annealing [130]. For a ten-second anneal the stability limit was found to be 1050 ^{o}C for GaN, 1150 ^{o}C for AlN and 550 ^{o}C for InN.

1.8 Overview and Scope of Present Work

The development of heteroepitaxial GaN during the last decade has permitted the development of nitride-based visible and UV emitters as well as high power and high temperature electronic devices. The scaling of current production processes to larger areas (e.g., wafer diameters beyond 50 mm) will be difficult because of increased wafer bowing produced by the lattice mismatch between GaN and the current substrates (i.e., sapphire and SiC). Additional issues such as cleavage planes, defect densities in scaled wafers, electrical conductivity type and ranges, thermal conductivity, and surface finish further motivate research on the growth of large area GaN substrates.

This is a strong rationale for the production of large area GaN single crystal substrates. The growth of large GaN single crystals, however, is one of the most difficult challenges in crystal growth. The combination of high melting temperature and equilibrium pressure has precluded practical melt growth by conventional approaches.

The second chapter describes a technique for the growth of high quality, freestanding GaN wafers (1 cm^2) delaminated from both LiGaO$_2$ and LiAlO$_2$ substrates by hydride VPE. The production of GaN wafers would provide a major advance for the nitride industry.

Chapter 3 describes the optimization of the merged-hydride deposition system. Using this information, the reactor was recently scaled-up to accept two-inch wafers.

Chapter 4 details the development of low-temperature GaN epitaxy on silicon substrates. As silicon substrates are relatively inexpensive, available in high quality and large quantity, they present many manufacturing advantages over other available substrates such as sapphire and SiC.

The thermal and chemical stability of GaN and related materials is important to growth and device processing, and is not well understood. Chapter 5 gives the experimental results on a series of vaporization experiments in various ambient gasses. The results reveal decomposition or sublimation of GaN depending on the nature of the ambient gas, annealing temperature, and growth technique.

The sixth chapter gives a theoretical description of the sublimation of MOCVD GaN and the decomposition of HVPE GaN. The results of this derivation are confirmed by comparison to experimental data from chapter 5.

Lastly, the seventh chapter provides conclusions and recommendations for future work.

CHAPTER 2
GALLIUM NITRIDE GROWTH ON LITHIUM GALLATE AND LITHIUM ALUMINATE

2.1 GaN Growth on LiGaO$_2$

2.1.1 LiGaO$_2$ Properties

A promising substrate for growth of GaN is LiGaO$_2$ (LGO). Hexagonal GaN is nearly lattice-matched (0.9%) to orthorhombic (wurtzite-like) LGO. The lattice-match along the a-axis is more critical for the GaN deposition than the c-axis because the preferred growth direction of GaN epitaxy is [0001]. This lattice-matched substrate is attractive because it would allow growth of high quality GaN films without the need for multiple buffer-layers, or lithographic patterning.

LGO has the superstructure of a complex oxide on a wurtzite-type crystal structure [131]. The crystal structure of LGO consists of alternating stacked metallic-atom and oxygen-atom layers on a wurtzite superstructure. The slight deviation from exact hexagonal symmetry is due to the need to accommodate metallic atoms of different sizes (Li = 1.55 Å vs. Ga = 1.41 Å). LGO is polar along the c-axis and has a Pna2$_1$ space group. An InGaN compound could be alloyed to exactly lattice-match LGO. Conventional Czochralski can pull single crystal LGO ingots. LGO does not possess a natural cleavage plane [132].

LGO is terminated by metallic cations (Li and Ga) or oxygen anions. Due to its polarity, LGO substrates sliced from an ingot will possess a cation-side and an oxygen-side.
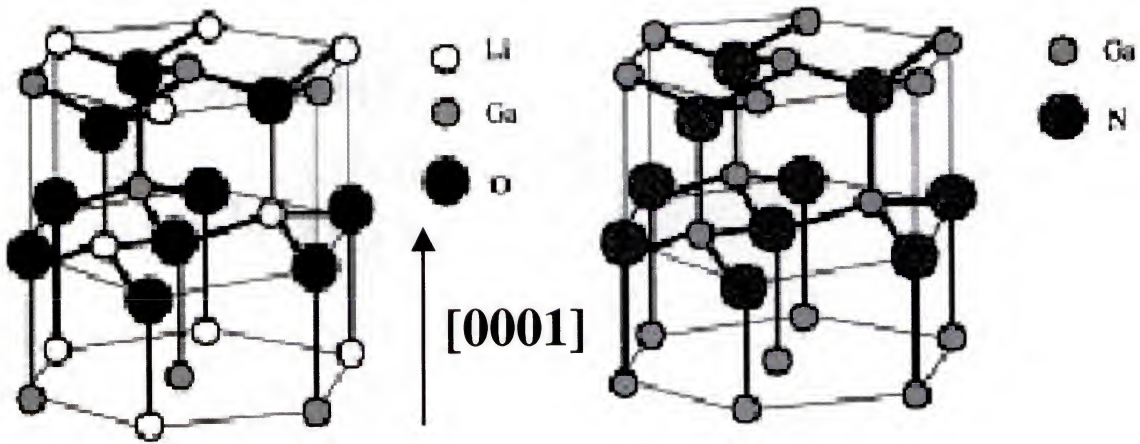
Figure 2-1. Crystal structure of a) LiGaO$_2$ b) GaN [132]

The (0001) surface atoms are triply bonded while the bulk atoms are tetragonally bonded. Marino and Hanneman calculated that the surface oxygen atoms have two dangling bonds while the surface metallic atoms have no dangling bonds [133]. This explains the observed etching rates. The metallic-terminated side etches slowly due to its absence of exposed electrons while the oxygen-terminated side with dangling bonds etches rapidly.

The LGO substrate was found to be very unstable in a hydrogen ambient. Many groups believed LGO was unsuitable as a substrate due to its lack of thermal stability in hydrogen. Employing nitrogen as the carrier gas was the first step to producing high quality films on LGO.

2.1.2 Nitridation of LiGaO$_2$

Pre-growth, in-situ nitridation of LGO was found to be crucial for preparing the substrate for GaN epitaxy. By flowing ammonia gas over a clean substrate, the near surface region reconstructs to form a compliant interfacial product. This surface

reconstruction is evident the high-resolution cross-sectional transmission electron micrograph shown in figure 2-2.
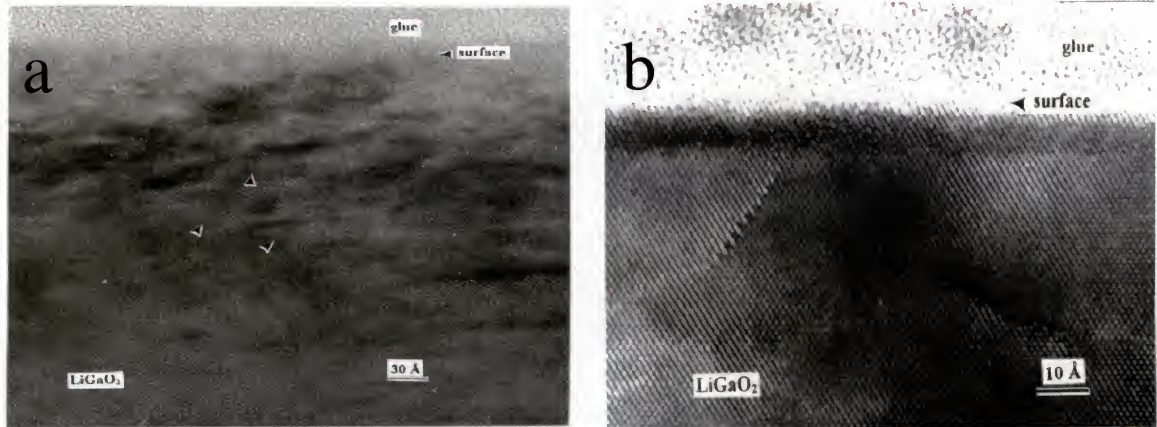

Figure 2-2. HTEM a) as received b) post nitridation at 900 °C, 10 min

From the AFM micrograph shown in figure 2-3, it is evident a surface smoothing mechanism occured. The pictures (figure 2-3) show the RMS roughness significantly decreased after nitridation at 850 °C from 3.4 to 0.04 nm.
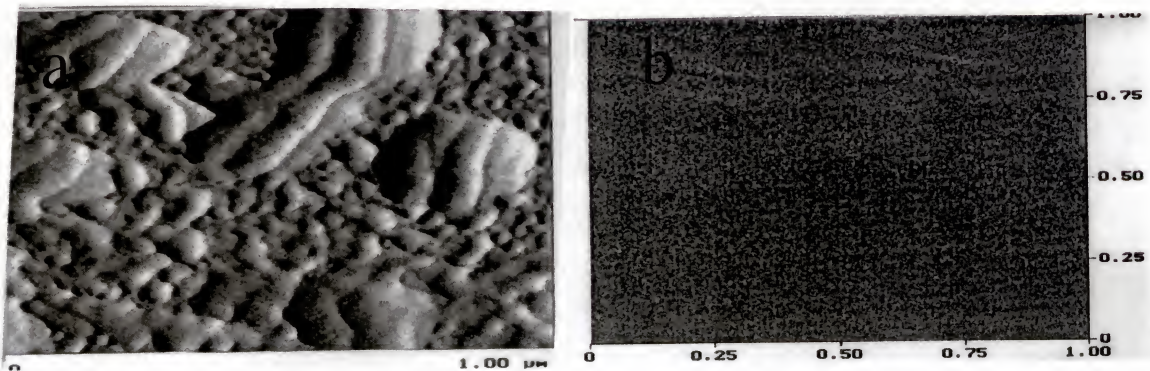

Figure 2-3. AFM of LGO surface a) as received b) post nitridation at 900 °C for 10 min

The AES spectra (figure 2-4) show that after nitridation a definite N_{KLL} peak is present [134]. This indicates that nitrogen was incorporated into the LGO surface. Also, after nitridation there is no increase in the lithium signal. It appears that the interfacial layer acts as a barrier that prevents lithium from inter-diffusing into the GaN epilayer. The thin layer of nitrided material has the same orientation as the substrate. This interfacial layer supplies nucleation centers that decrease the interfacial stress between the substrate and the subsequent epilayer of GaN.
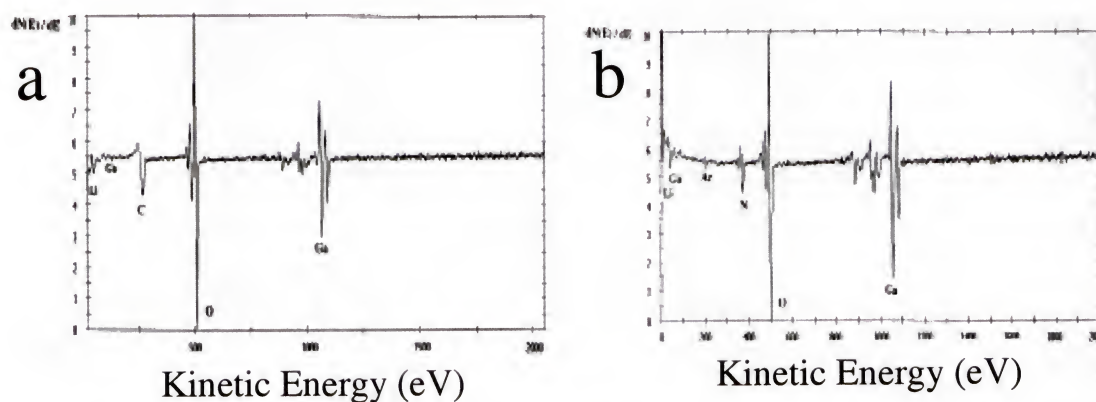

Figure 2-4. AES of LGO surface a) as received b) post nitridation at 900 °C for 10 min

As described, the cation-terminated side reacts with the incoming ammonia to prepare the surface for epitaxial growth. For the oxygen-terminated side, the metallic atoms are not available to form this interfacial layer. Instead the ammonia forms an oxy-nitride on the surface. Many groups growing on the "wrong" side of LGO had mediocre results. In this situation, thin films were observed to crack and peel.

2.1.3 MOCVD of GaN on LGO

Dr. Kryliouk and T. Dann carried out all MOCVD work in the Nippon Sanso conventional cold-wall MOCVD horizontal reactor. Once proper surface preparation was

determined, high quality layers of GaN (n-type) on LGO were deposited by MOCVD (temperature = 850 °C, pressure = 76 torr, V/III ratio= 3000).   In fact, for a GaN film grown at 850 °C, a double-axis ω-scan FWHM of 21.6" was measured (figure 2-5a), one of the lowest values ever reported for GaN. The surface was smooth as seen by figure 2-5b indicating a two-dimensional growth mode.
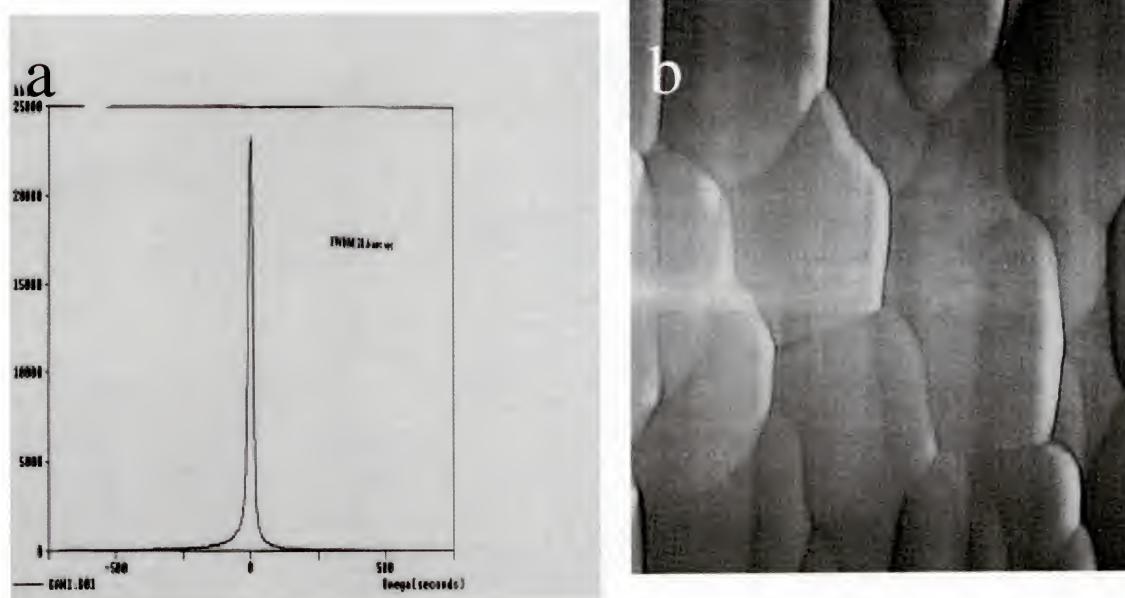

Figure 2-5. A GaN deposited on LiGaO$_2$ at T=850 °C. a) HRXRD measured a FWHM = 21.6" b) AFM measure surface roughness, R$_g$ = 0.036 nm [134]

The low defect density is seen in the XTEM in figure 2-6. The dislocation density at the interface was 10^9 cm^{-2}, comparable to interfaces in homoepitaxy of GaN. At a distance of greater than 0.3 μm from the interface a dislocation density of less than 10^7 cm^{-2} is observed, excellent for bulk microstructure.

Figure 2-6. XTEM of GaN deposited on LiGaO$_2$ (T$_{Growth}$ = 850 ^{o}C) [134]

2.2 Merged H-MOVPE GaN Growth on LiGaO$_2$

A hybrid MOCVD/hydride vapor phase epitaxy (H-MOVPE, merged-hydride) reactor was built that has the capability of growing by hot-wall MOCVD or HVPE (figure 2-7). MOCVD growth uses the customary chemistry of TMGa and NH$_3$ to deposit GaN. The HVPE chemistry is slightly different as the conventional liquid Ga source is replaced with TMGa, with GaCl produced by reacton between HCl and TMGa instead of the liquid Ga. The source reaction that is isolated upstream from the NH$_3$ line is

$$Ga(CH_3)_3{}^v + HCl^v \rightarrow GaCl^v + 3CH_4{}^v \qquad (2.1)$$

It is anticipated that there should be no carbon contamination from the group III source since the methyl radicals are instantly converted to essentially inert methane gas. As in conventional HVPE, the GaCl stream is then mixed with the NH$_3$ stream and passed over

the substrate located in the hot growth zone, where the following deposition reaction occurs

$$GaCl^v + NH_3^v \rightarrow GaN^s + HCl^v + H_2^v \qquad (2.2)$$

The advantages of this design include: 1) MOCVD or HVPE in the same reactor thus not exposing the surface to ambient, 2) in-situ cleaning, 3) improved NH_3 cracking since the residence time at temperature is increased, 4) rapid reactant switching, and 5) HVPE deposition with low background impurities and high growth rates [134]. This design allows an initial smooth MOCVD film to provide a template for thick HVPE growth and to protect the substrate from attack by HCl or H_2. Once GaN of sufficient thickness is grown, a final device layer or structure could be grown by MOCVD.
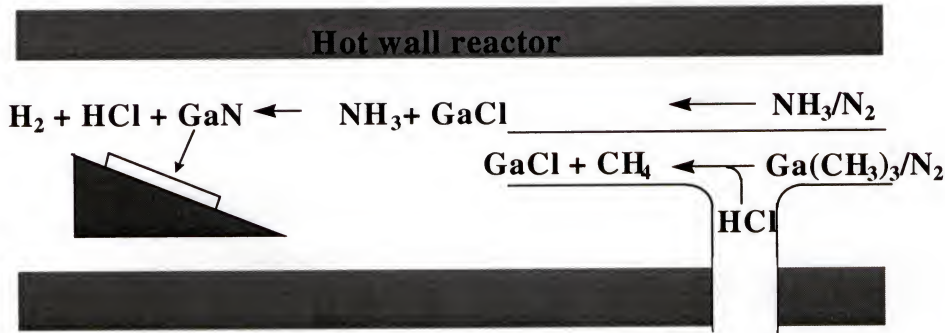

Figure 2-7. Schematic of the merged hydride CVD system [134]

This reactor (figure 2-7) was used to grow large, single-crystal, thick films of GaN on LGO by a sequence of growth steps shown in figure 2-8. GaN and $LiGaO_2$ are nearly lattice-matched, but not entirely chemically compatible. To protect the $LiGaO_2$ surface from HCl attack, a thin layer of single crystal GaN film is first grown on a

LiGaO$_2$ wafer by MOCVD, followed by the fast but corrosive HVPE process. A MOCVD capping layer is then grown to smooth the surface. During cool-down, the thick GaN was found to delaminate from the LiGaO$_2$ substrate. The reaction layer at interface allows easy separation of thick film from the substrate. Growth conditions for the films were as follows: pressure: MOVPE @ 760 Torr, HVPE @ 760 Torr; V/III ratio: MOVPE 3000, HVPE 125; temperature: MOVPE 900 ^{o}C, HVPE 560 to 900 ^{o}C.
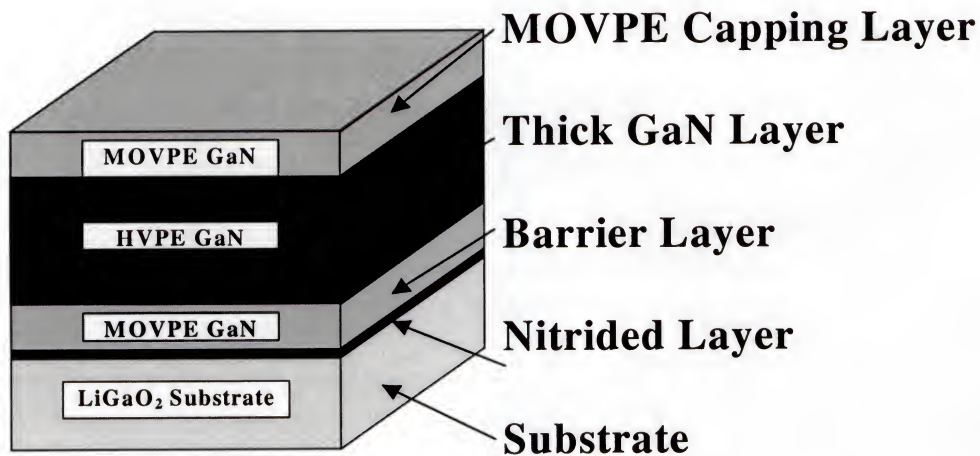

Figure 2-8. Growth sequence to produce thick H-MOVPE GaN on LGO [134]

Figure 2-9 shows a free-standing GaN wafer grown using the H-MOVPE system. The pictured film is 300 μm thick. It was found that the self-separation process is critically dependent on nitridation time and cooling procedure. A 10 min nitridation time was shown to produce GaN films with the highest crystalline quality. During the 3 hr cool down, ammonia flow was maintained until the reactor was less than 700 ^{o}C to suppress decomposition of the GaN surface.

This film was relatively smooth (RMS roughness, R_g = 0.3 nm) by AFM, and a FWHM of 46.7 arcsec (figure 2-10b) showed that the GaN had relatively high crystal quality. Also, the free-standing GaN had uniform composition on both sides when depth profiled with AES (figure 2-10).

Figure 2-9. H-MOVPE growth of thick GaN; size: 10 x 10 x 0.3 mm³ [134]
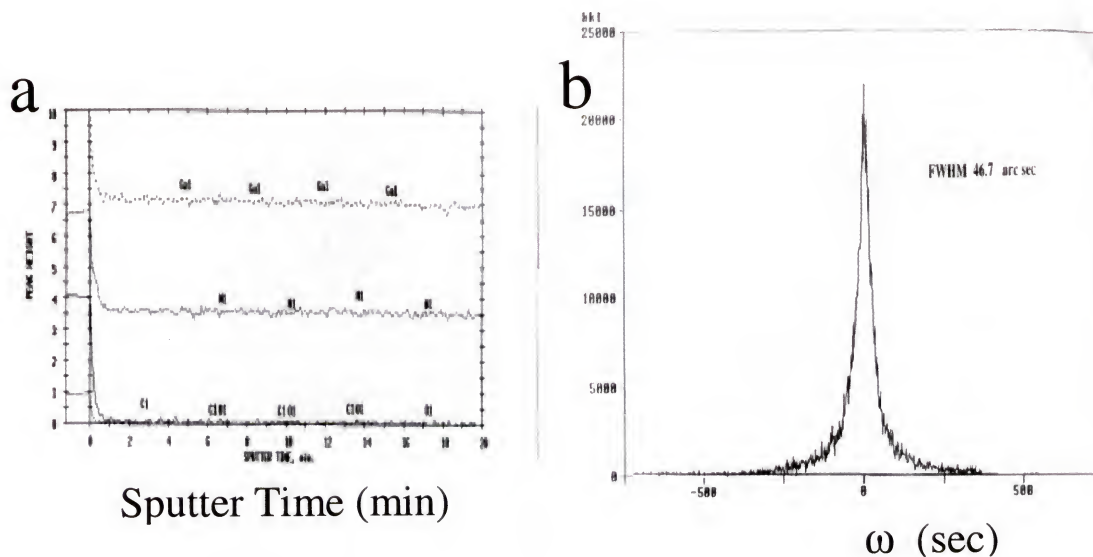

Figure 2-10. Free-standing GaN a) AES depth profile b) (002) double-axis X-ray rocking curve; ω scan; FWHM = 46.7 arcsec [134]

Micro-Raman scattering (figure 2-11) exhibited no shift on the peak position of the strain-sensitive phonon E_2 (570 cm^{-1}). This indicates the crystal is residual-deformation-free [134]. Using the 514 nm line of an argon laser, the Raman spectra were excited in the back-scattered geometry. The scattered light was detected by Jobis-Yvon RAMANOR U-1000 double monochromator with a slit width of 100 μm, with a resolution better than 1.0 cm^{-1}.
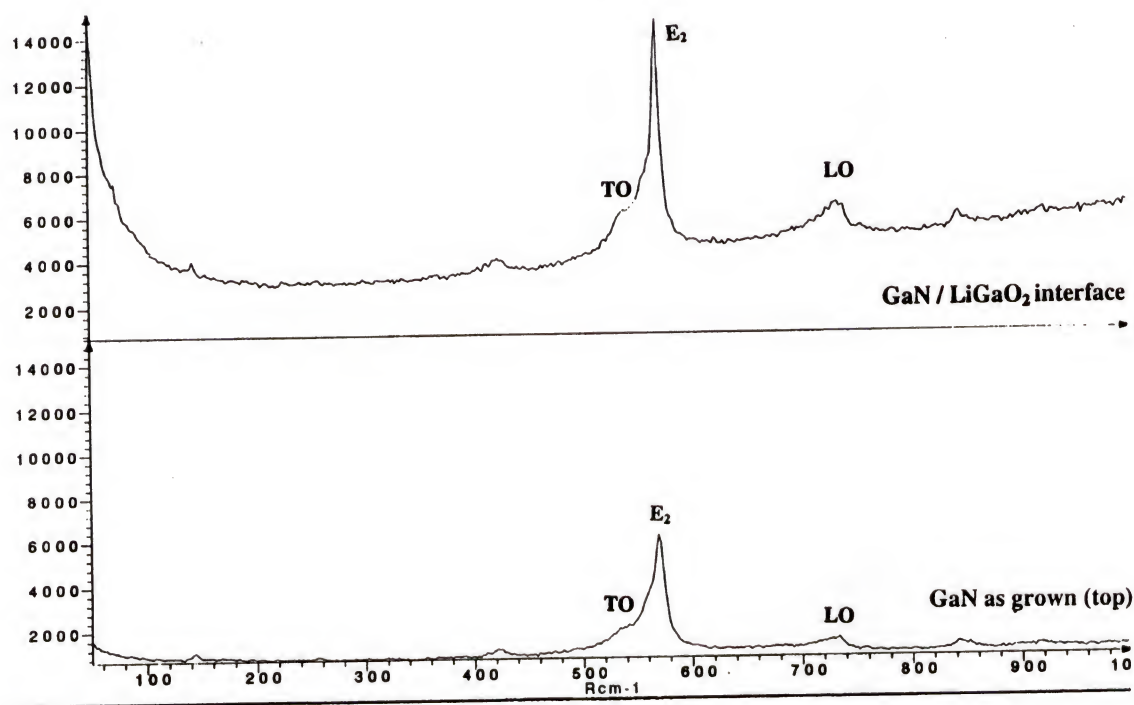
Figure 2-11. Raman spectra of bulk single crystal GaN [134]

HVPE growth on MOCVD LGO showed signs of LGO decomposition even when a protective MOCVD layer was used. The substrate when removed from the reactor was cracked and brown or black in color. It was postulated that HCl was attacking the backside of the LGO wafer. A two-step MOCVD sequence that deposited a protective layer on both sides of the LGO wafer was employed. This technique prevented LGO

decomposition during HVPE growth, and higher quality and reduced impurity GaN was attained.

Clearly $LiGaO_2$ is a promising substrate for growth of GaN. To demonstrate this fact, growth on a 2-inch LGO wafer was performed. It has been reported [135], however, that LGO (001) substrates cut from c-axis pulling usually have two different domains separated by straight lines, frequently belonging to <110>. These are attributed to polarity domains [136]. For this reason, the GaN film grown on 2-inch LGO prematurely peeled during growth. If LGO crystal growth technology improves, LGO would be well suited for large area, device-quality thin films or free-standing thick GaN.

2.3 GaN Growth on $LiAlO_2$

An alternative to LGO is (1 0 0) $LiAlO_2$ (LAO). Although the lattice mismatch between (0 0 0 1) GaN and (1 0 0) $LiAlO_2$ (1.9 %) is slightly larger than GaN/LGO (figure 2-12), LAO substrates are extremely stable under growth conditions. QuIn particular, LAO is resistant to hydrogen, presumably due to the strong Al-O bond. LAO is tetragonal with a $P4_12_12$ space group. An AlGaN compound could exactly lattice-match LAO. LAO congruently melts at 1600 °C, and single crystal LAO ingots can be pulled by conventional Czochralski growth. LAO does not possess a natural cleavage plane [70].

HVPE GaN films grown in a nitrogen carrier gas showed possible signs of oxygen contamination. Typically films that were yellow in color had high oxygen levels when probed by AES or XPS. Switching to 100% hydrogen as the carrier gas was found to give excellent quality HVPE films on LAO. As these films showed no sign of oxygen contamination, it is likely the hydrogen getters the residual oxygen out of the system.
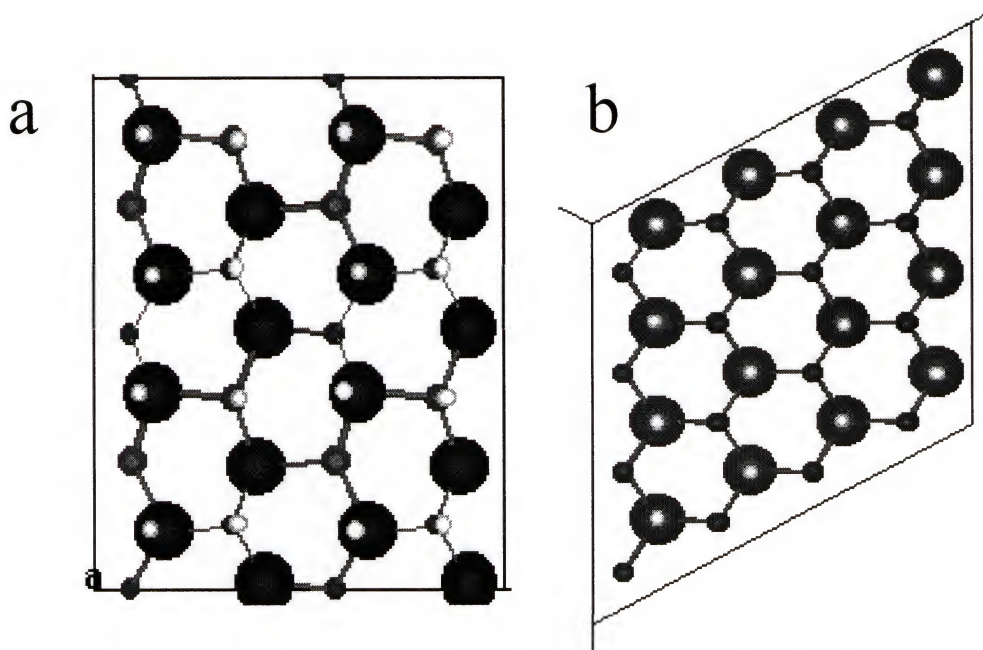
Figure 2-12. Crystal structure a) (100) LiAlO$_2$ b) (0001) GaN [70]

Similarly it was found that MOCVD GaN/LAO films grown with a nitrogen carrier gas suffered from oxygen contamination. Switching to hydrogen as the carrier gas, however, caused the TMGa to decompose in the inlet region rather than in the vicinity of the substrate (chapter 1), introducing carbon contamination into the films. The merged H-MOVPE system is a hot wall reactor, and sharp temperature gradients seen in cold-wall MOCVD systems are not possible to produce. Dr. Kryliouk proposed a 4%-H$_2$/basis-N$_2$ mixture for the carrier gas to getter the oxygen and to prevent decomposition of the TMGa until it reached the vicinity of the substrate. Results of growths that used H$_2$/basis-N$_2$ mixture for the carrier gas are presented below.

Thick HVPE and thin MOCVD GaN/LAO have been grown in the H-MOVPE system. Thick films on LAO were successfully produced using various sequences

including HVPE, MOVPE/HVPE, and MOVPE/HVPE/MOVPE. Although somewhat gray in color from surface roughness, the films showed no sign of carbon contamination. This GaN deposited on 5x5-mm LAO delaminated during the cool-down to yield free-standing GaN. Presently from LAO, the thickest free-standing GaN fabricated was 60 μm thick.

Figure 2-13 shows a low-resolution XRD spectrum of free-standing GaN grown on an LAO substrate, and the results indicate that the film is single crystal. The sharpest FWHM measured by high-resolution XRD was attained for a structure consisting of 30-min MOCVD/2-hr HVPE/15-min MOCVD capping-layer. Growth conditions for the films were as follows: pressure: MOVPE @ 760 Torr, HVPE @ 760 Torr; V/III ratio: MOVPE 3000, HVPE 125; temperature: MOVPE 900 °C, HVPE 900 °C.
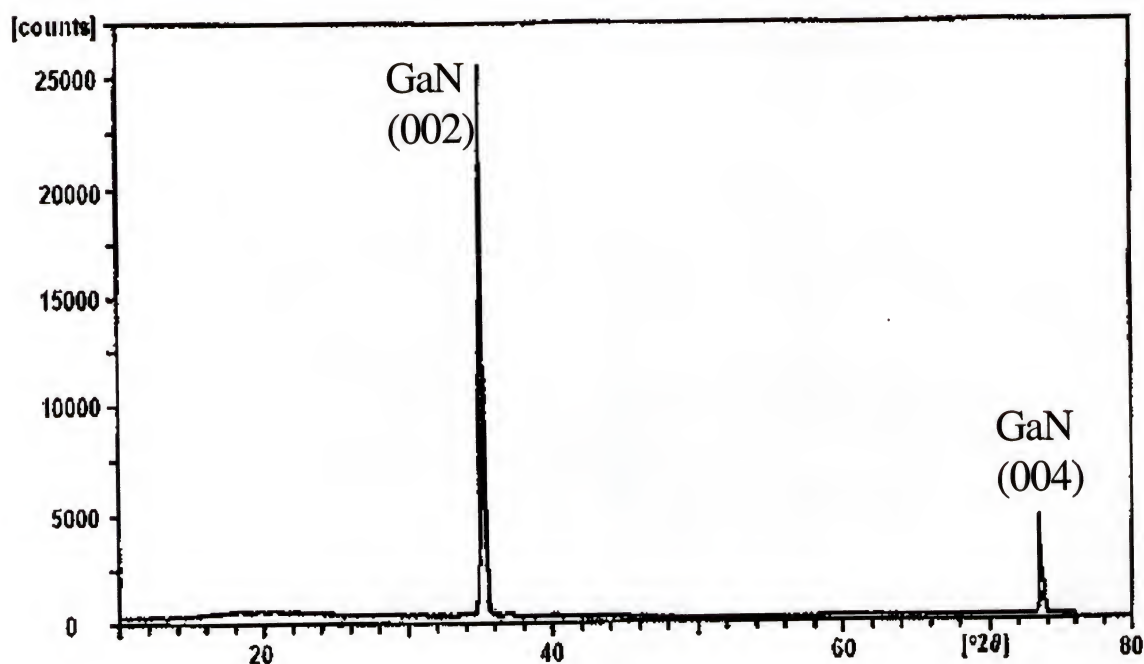

Figure 2-13. XRD of free-standing GaN grown from an LAO Substrate

Figure 2-14 displays Raman measurements for free-standing GaN grown for various MOCVD growth times followed by a 2 hr HVPE growth. When a Raman system is operating in Stokes mode, the E_2 (asymmetric stretching, second harmonic) peak wave-number will increase due to an decrease in compressive stress. In figure 2-14, the strain-sensitive E_2 peak slightly increased in wave-number (~562 cm^{-1}) for increasing MOCVD growth time. This result confirms the benefit of increasing the thickness of the MOCVD buffer-layer up to a 30-min growth-duration.

Furthermore, this result compares to GaN/LGO Raman measurement that reported an E_2 peak at 570 cm^{-1} (figure 2-10). As GaN/LGO is more closely lattice matched than GaN/LAO, GaN/LGO has less residual stress and thus an E_2 peak occurs at a higher wave-number.
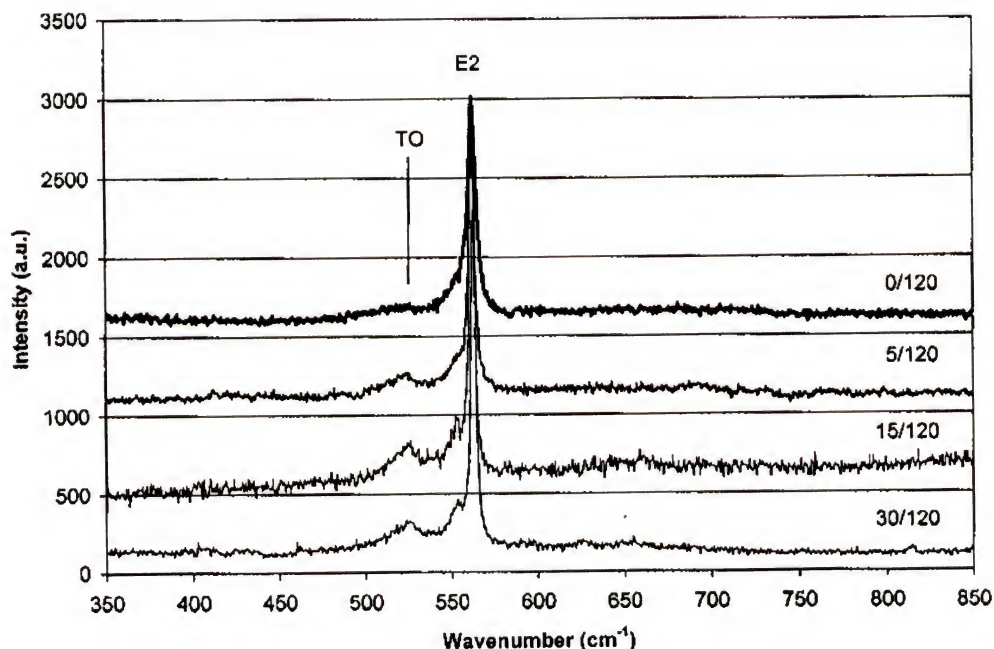

Figure 2-14. Raman measurement of free-standing GaN for different MOCVD growth-time (min)/120 min HVPE growth time. The spectrum shows a shift in strain sensitive E_2 peak

Furthermore, the strength of the TO (Transverse Optical) peak is a qualitative measure of crystalline quality. Increasing the MOCVD growth time improves the quality of the GaN crystal structure as is seen in an increase in signal strength of the TO peak .

2.5 Conclusions

This chapter described the successful growth of single crystal GaN substrates by combining the rapid growth rates possible in HVPE with the nearly lattice matched crystal structure of $LiGaO_2$ and $LiAlO_2$ substrates. Keys to obtaining high quality GaN films on $LiGaO_2$ are an initial surface nitridation step followed by growth of an MOCVD buffer layer.

A self-separating technique was developed that leaves free-standing smooth single crystal, and strain free GaN without mechanical or chemical treatment. It was determined that surface nitridation and cooling process are critical to delaminating. The surface morphology of the GaN films was determined by AFM, the structural quality was analyzed by XRD and TEM. Negligible amounts of oxygen and carbon impurities incorporated into the film as judged by AES, ESCA and SIMS.

The LAO substrate has many of the same qualities as LGO, however, LAO is stable in an HCl atmosphere and insensitive to hydrogen as the carrier gas, making LAO ideal for thick HVPE growth of GaN.

CHAPTER 3
TWO-INCH REACTOR SCALE UP

3.1 Introduction

Recently, the H-MOVPE (merged-hydride) reactor was scaled up to accept 2" diameter substrates. Details of the reactor construction and support system are described in Appendix A. The large increase in reactor cross-sectional area dramatically affected reactor flow profiles and temperature gradients. For these reasons, a parametric study was performed on the system jointly with Mike Reed [136] to clarify optimal growth conditions. The reactor was optimized for use of LAO, LGO and sapphire. The most extensive study performed used sapphire substrates due to their moderate cost. Therefore a detailed description on the optimization of GaN on sapphire will be provided below. The optimization study was performed for MOCVD and HVPE; however, this report will focus on HVPE, as it is the method used to grow thick films. The effects of substrate temperature, V/III ratio, HCl/III ratio, and wafer position on substrate structural and chemical quality for both MOCVD and HVPE films were examined. Film characterized by AFM, XRD, PL, and AES.

3.2 Optimization

Changing the reactor diameter has a significant impact on the reactor geometric aspect ratio, flow profiles, and temperature profiles. Only one of the variables investigated (temperature, TMGa flow-rate, NH_3 flow-rate, III/Cl ratio, V/III ratio and carrier gas) was changed at a time. In these experiments when a

species flow-rate (e.g., NH$_3$) was changed, a constant total flow rate was maintained by adjusting the carrier gas flow-rate. Sapphire substrates were used because they tended to produce the most reproducible GaN in the merged-hydride system. The sapphire samples were prepared by immersion sequence of trichloroethylene/acetone/methanol at 50 °C then blown dry with nitrogen. The pertinent results are presented below.
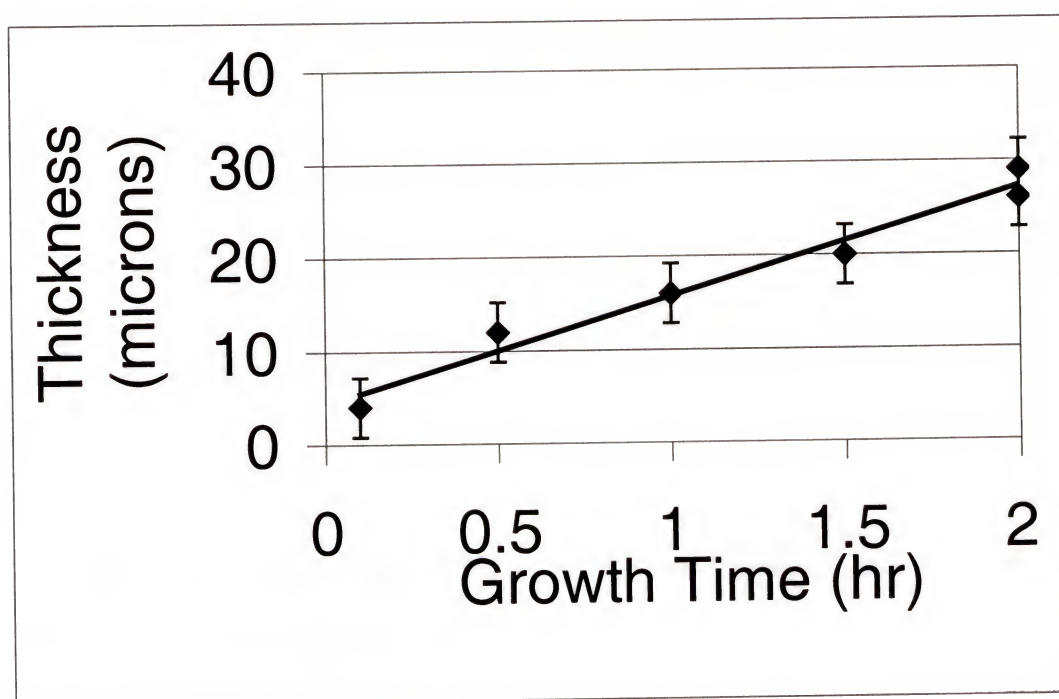
Figure 3-1. HVPE GaN film thickness as a function of time

Figure 3-1 shows a nearly linear growth rate as a function of growth time (T$_{growth}$ = 950 °C, HCl/Ga = 2.0, F$_{NH3}$ = 500 sccm). Typically a peak in growth rate is seen in the first few minutes of growth.

Figure 3-2 indicates linear dependence on growth rate on TMGa mole flow rate is seen under standard growth conditions. The upper limit of TMGa flow is limited by excessive gallium deposition inside the reactor inlet. Furthermore, at

extremely high TMGa flow-rates, the resulting GaN film was poly-crystalline. At high TMGa flow-rates where growth-rates exceeded 25 μm/hr, non-uniformity was observed on 2-inch diameter substrates. Likely, proper mixing of the vapor phase was not occurring at high TMGa flow-rates as the inlet can act like a point source.
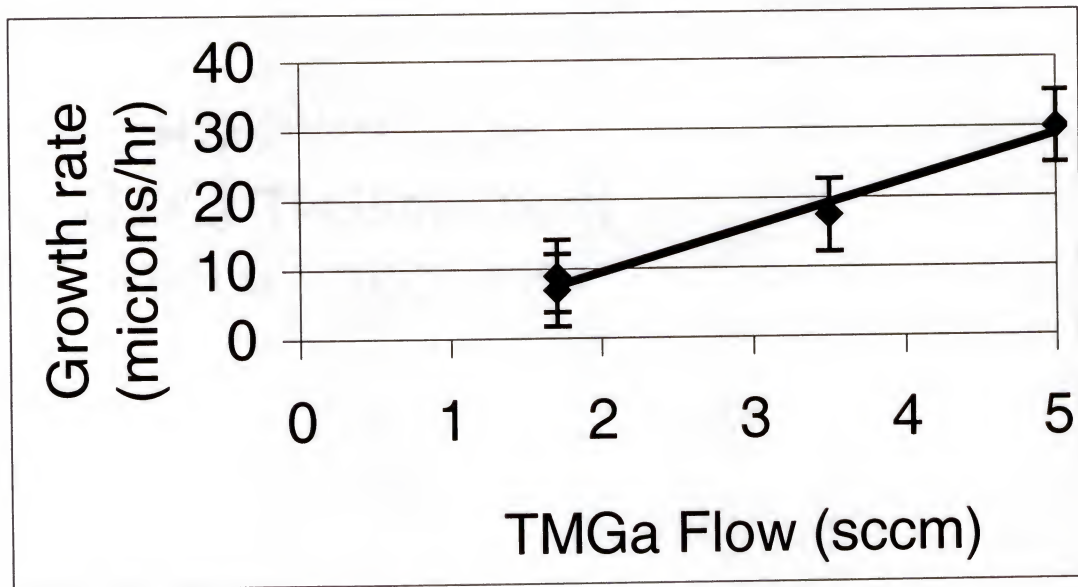
Figure 3-2. Linear dependence of HVPE growth rate on TMGa flow

The transition from kinetic controlled growth mode to a diffusion one at around 700 °C is apparent from the growth rate data depicted in figure 3-3. This figure also shows the growth rate in the kinetic controlled regime (500 to 700 °C) increases exponentially with temperature. A fairly level plateau in growth rate (10 μm/hr) is seen in the diffusion controlled growth regime (700 to 965 °C).

It was found from XRD analysis that films grown under 500 °C were amorphous, over 850 °C were single crystal and between 500 and 850 °C were poly-crystal [136].

Figure 3-3. HVPE GaN growth rate versus growth temperature (K)
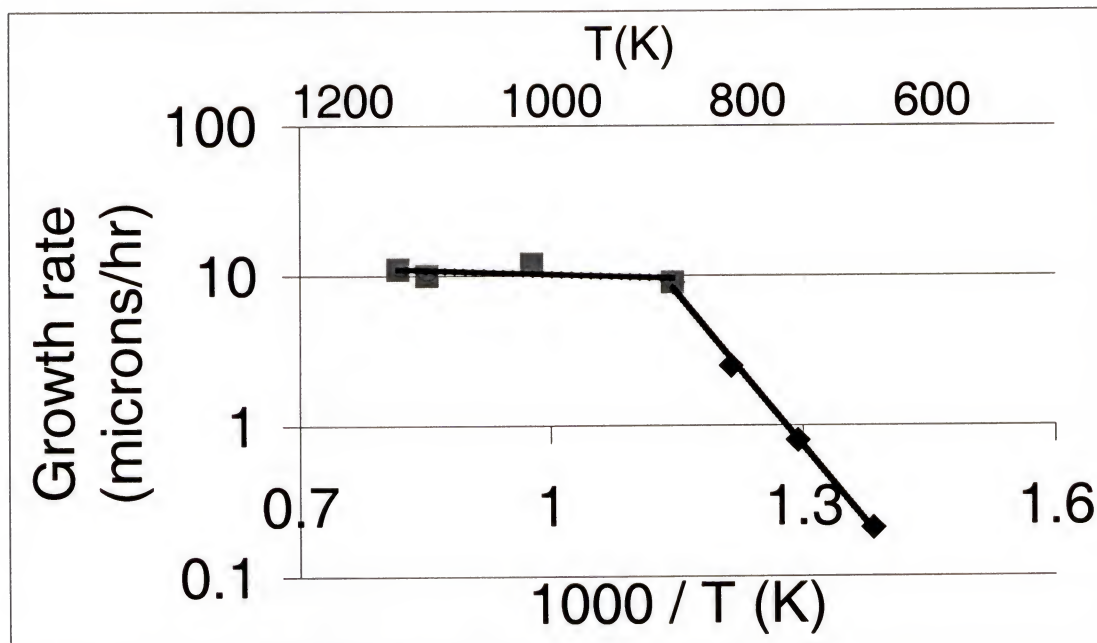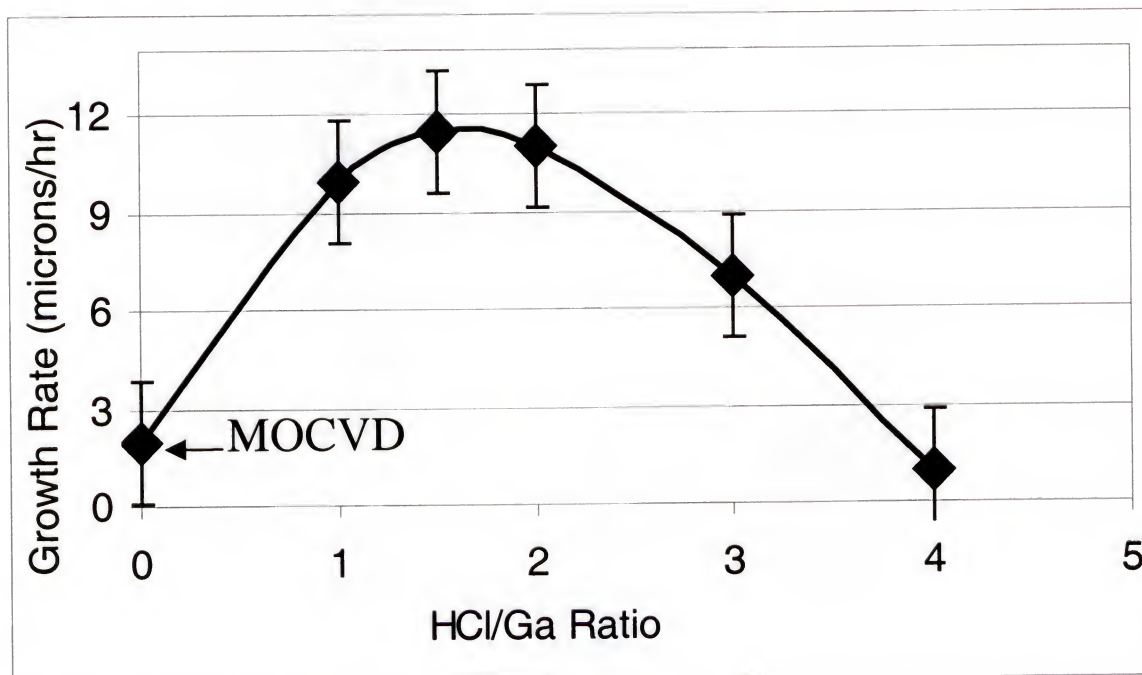

Figure 3-4. Growth rate of HVPE GaN versus HCl/Ga Ratio

Figure 3-4 shows an increase in growth rate as the HCl/Ga ratio increases

from zero. This indicates the reaction is changing from MOCVD to HVPE in this

HCl/Ga range. Thus the increase in growth rate with increasing HCl/Ga ratio can be explained on the generation of more GaCl molecules available to diffuse to the growth surface through the boundary layer.

A plateau in growth rate is seen at an HCl/Ga ratio of one to two followed by a decrease in growth rate at higher ratios (figure 3-4). At extremely high ratios (> 5), no growth is seen. At an HCl/Ga ratio of zero, the merged-hydride reactor is essentially operating in MOCVD mode. Normally for MOCVD in the merged-hydride system, different temperature profiles are used for MOCVD vs. HVPE. The inlet region is usual held at a lower temperature for MOCVD (~600 $^{\circ}$C) than HVPE (~750 $^{\circ}$C) to prevent premature decomposition of the TMGa.
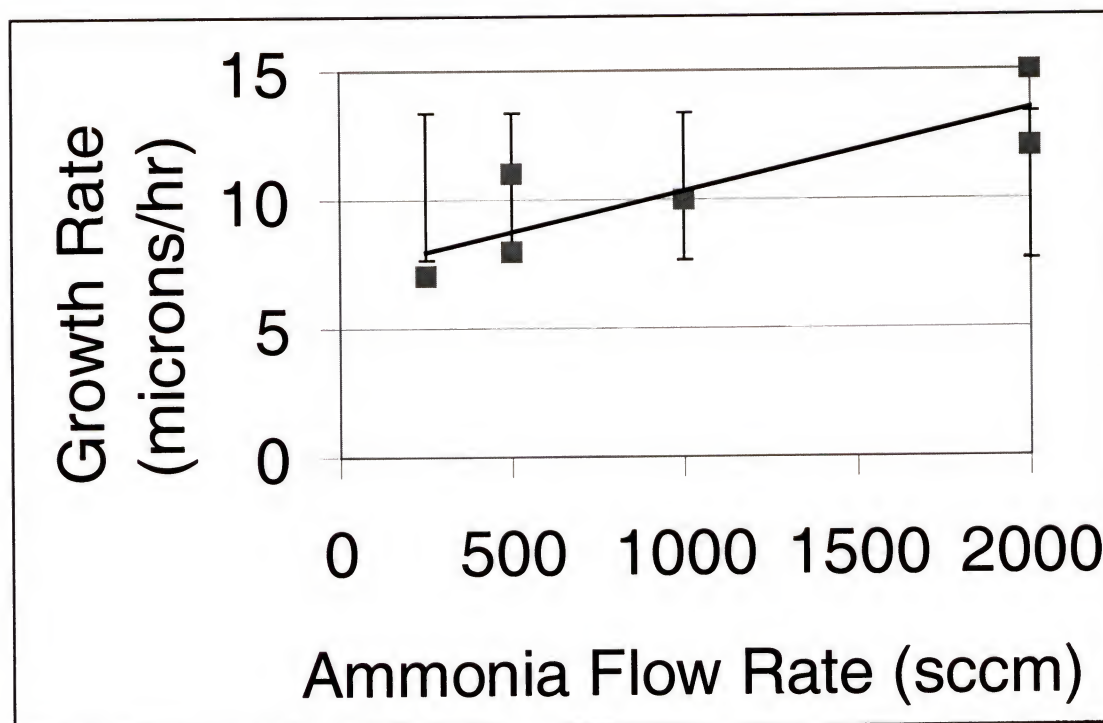

Figure 3-5. Growth rate of HVPE GaN as a function of NH$_3$ flow-rate

Figure 3-5 illustrates a near zero order dependence of growth rate on the NH$_3$ flow-rate. This indicates that the growth rate is dependent on the arrival rate of

gallium to the growth surface. At ammonia flow-rates less than 100 sccm, a poly-crystal/metallic gallium mixture formed instead of single crystal gallium nitride.

Film thickness was mainly determined by XSEM, gravimetric and XTEM analysis. Further confirmation was provided by carbon painting a small area of the sample and measuring a step height with a mechanical profiler.

3.3 Comparison of MOCVD and HVPE Films

As the scale-up was performed used sapphire substrates, a comparison of the quality of GaN films grown on sapphire in the merged-hydride system using either the MOCVD or the HVPE modes. It is noted that the hot-wall furnace has a long ramp time for heating (on the order of a few hours). Attempts to grow buffer layers at low temperature resulted in poor quality films that were subsequently grown at high temperature. Likely the amorphous buffer layer decomposes during the long ramp time. Thus all films reported below do not have a low temperature buffer layer; a feature that has been required to produce high quality GaN on sapphire [10]. A general analysis of the crystalline and chemical properties of MOCVD and HVPE films is given below.

Raman Measurements. Figure 3-6 shows the results of Raman scattering measurement. In figure 3-6a, the position of the strain sensitive E_2 (Stokes mode, asymmetric stretching, second harmonic) peak is plotted as a function of depth. In Raman a depth profile can be generated, by changing the wavelength of the probe light, which changes depth of excitation. The wavelength is selected based on the absorption properties of the solid sample. Figure 3-6a illustrates the E_2 Raman shift measured from the GaN surface to the GaN/sapphire interface. It was found that the

GaN layer near the interface was under compressive stress and the film became relaxed near the GaN surface. The relaxation process was faster in the MOCVD films judging from the slopes of E_2 shift vs depth. Similarly, the decreasing FWHM (figure 3-6b) with increasing distance from the interface shows the film quality is higher near the film surface. Overall, the crystallinity of MOCVD GaN was slightly worse than HVPE GaN as judged by the FWHM of the E_2 peak (figure 3-6b).

X-ray Photoelectron Spectroscopy. The peak energy position in a photoelectron energy spectrum is a signature of a specific element, while its relative concentration can be estimated from the measured intensity of the peaks.

Measurements by XPS shown below illustrate the chemical composition of MOCVD (figure 3-7) and HVPE (figure 3-8) films. Surface contaminants such as oxygen and carbon observed in figure 3-7 and 3-8 likely formed when the sample was exposed to the atmosphere.

Photoluminescence (PL). In PL, laser light is used to induce excitation and subsequent relaxation of electronic states in the sample to measure physical and chemical properties. PL spectra illustrated in figures 3-9 and 3-10 show a strong band edge peak at 3.39 eV for MOCVD and 3.42 for HVPE. The measured FWHM was approximately the same for the MOCVD (162 meV) and the HVPE (161 meV).

X-ray Diffraction. As shown in figure 3-11, the crystallinity as detected by high resolution $\omega/2\theta$ XRD of MOCVD grown (0002) GaN peak (1597 arcsec) was slightly poorer than HVPE grown (0002) GaN peak (899 arcsec). This agrees with the results of the Raman measurements (figure 3-6) that the MOCVD films were of slightly lower crystalline quality compared to the HVPE films.

(a)
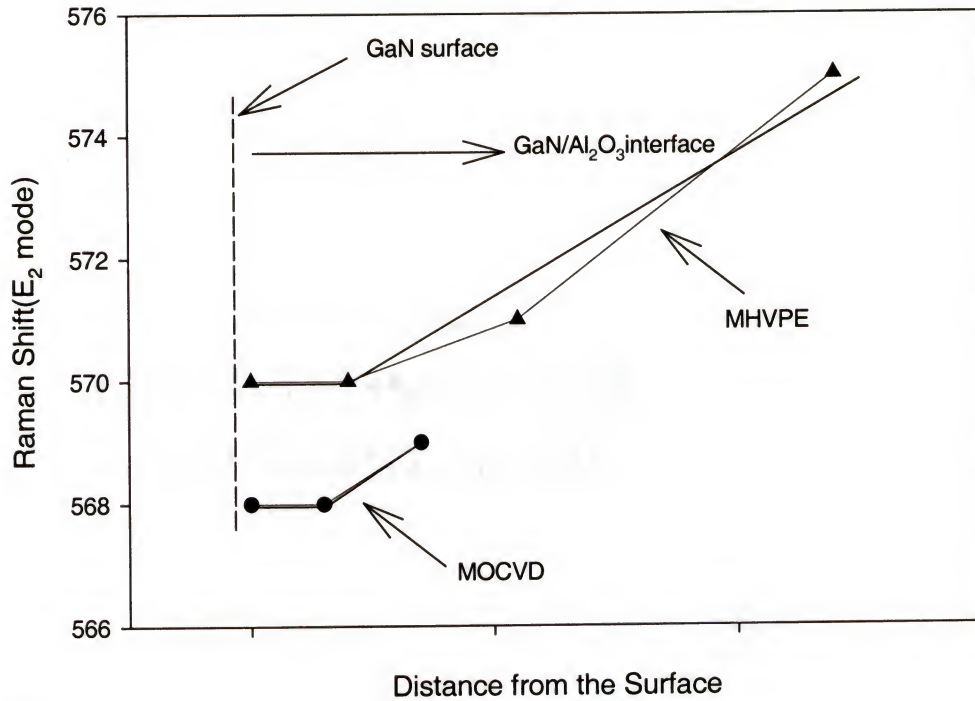
(b)
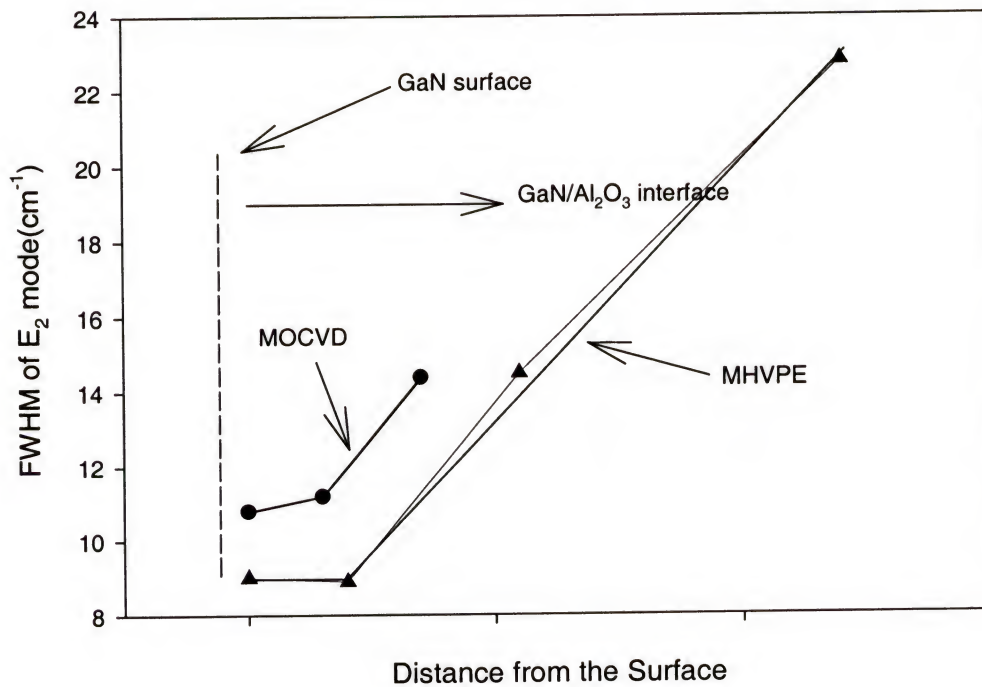
Figure 3-6. Raman scattering measurements as a function of depth for E_2 line a) Raman shift b) FWHM of the E_2 line
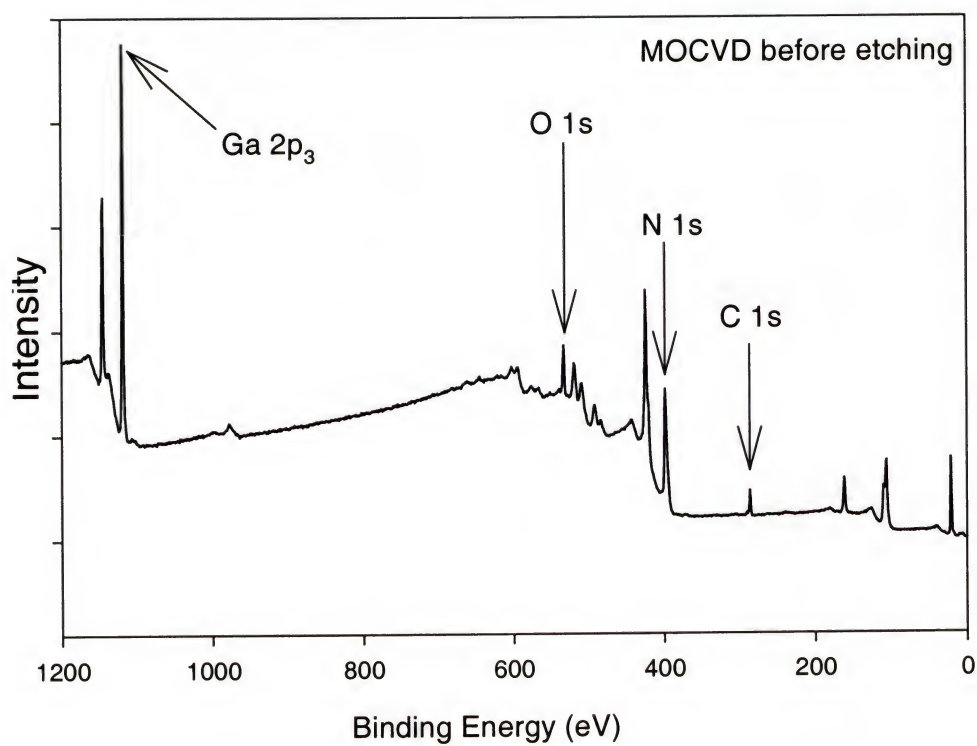
Figure 3-7. X-ray photoelectron spectrum of MOCVD GaN
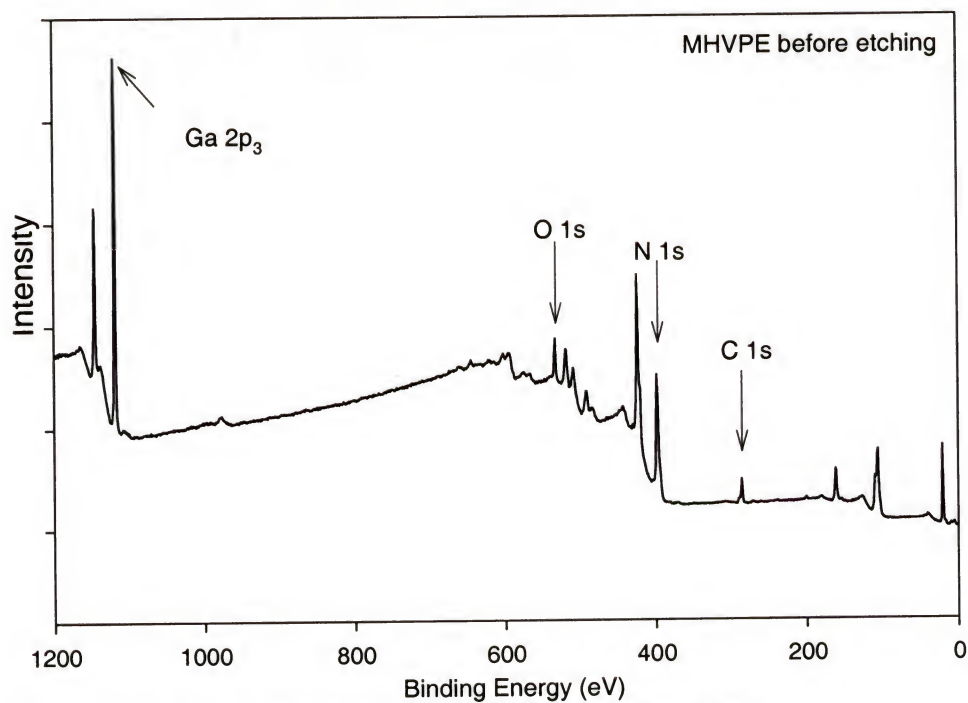
Figure 3-8. X-ray photoelectron spectrum of HVPE GaN
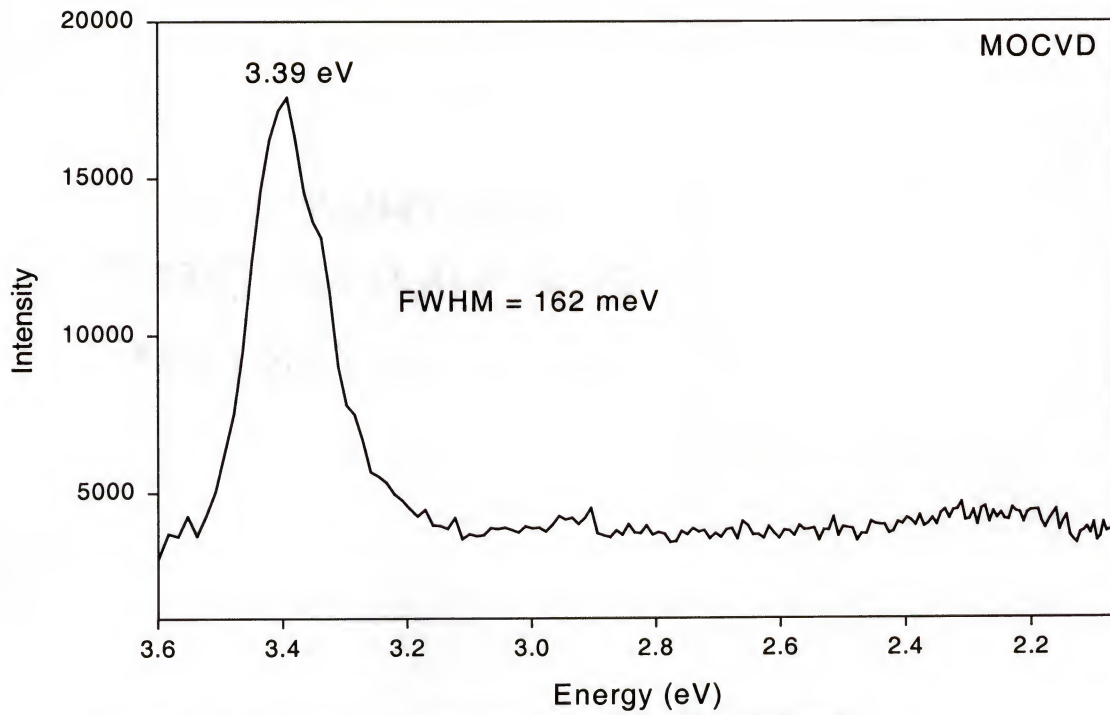
Figure 3-9. Photoluminescence of GaN grown by MOCVD
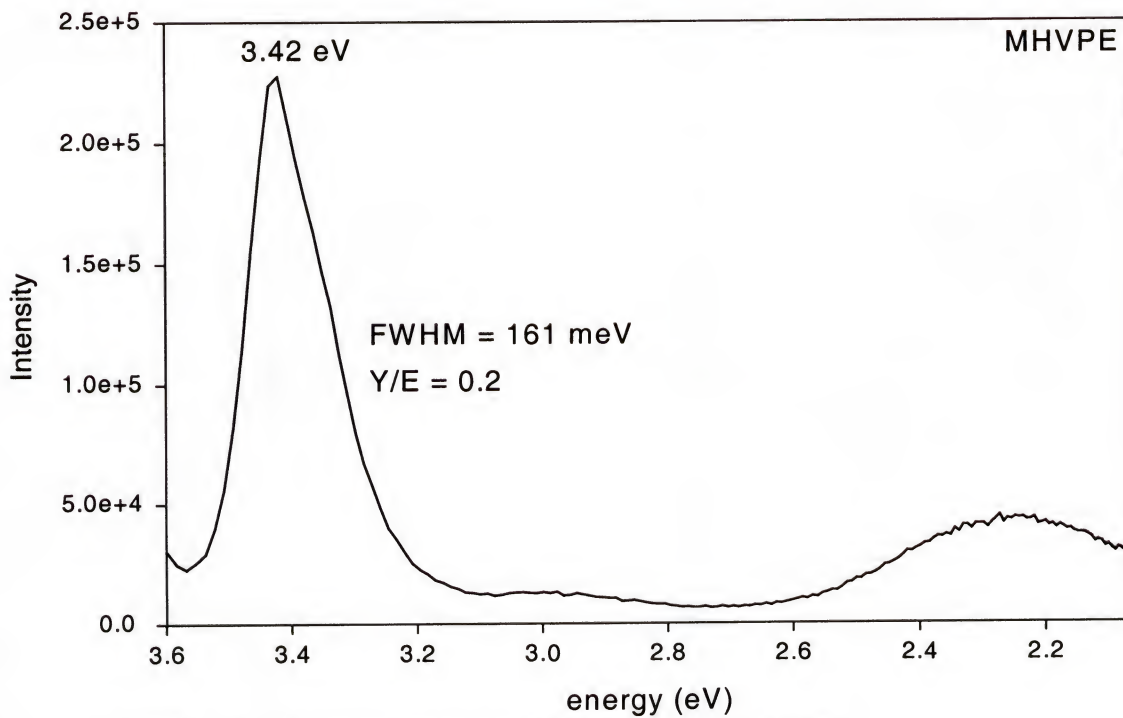
Figure 3-10. Photoluminescence of GaN grown by HVPE
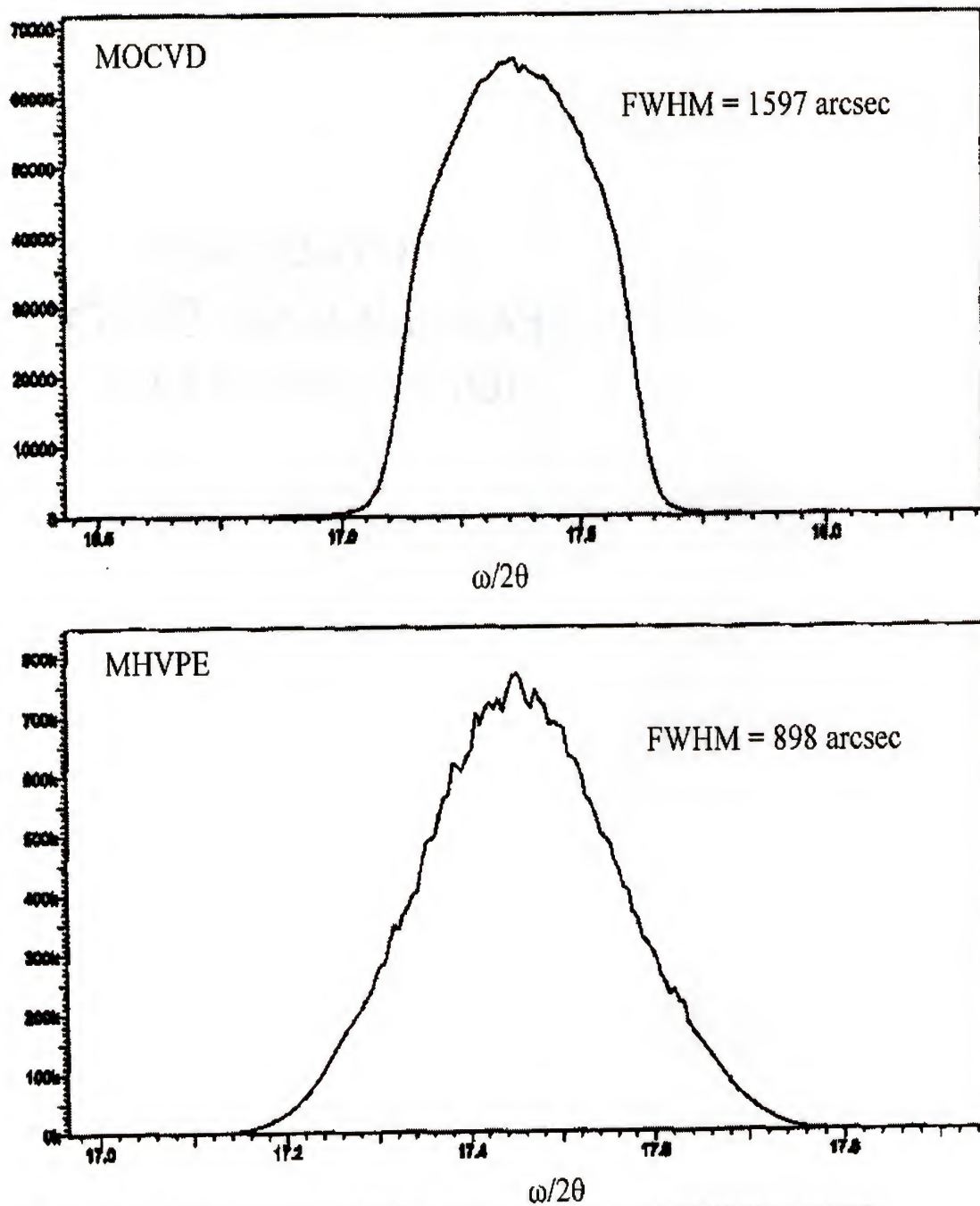
Figure 3-11. High resolution XRD of GaN grown by a) MOCVD b) HVPE

3.4 Deposition Byproducts

Similar to a traditional HVPE reactor, the main component of the wall deposition is ammonium chloride. This byproduct deposits on the inside walls of the reactor, exhaust lines, and scrubbing system. Figure 3-12 shows an XRD of

ammonium chloride (NH_4Cl) powder taken from the walls of the merged-hydride reactor. All peaks were assigned to ammonium chloride.

Figure 3-12 shows that appreciable amounts of gallium atoms are not lost to wall deposition by the absence of diffraction signals for gallium or compounds containing gallium
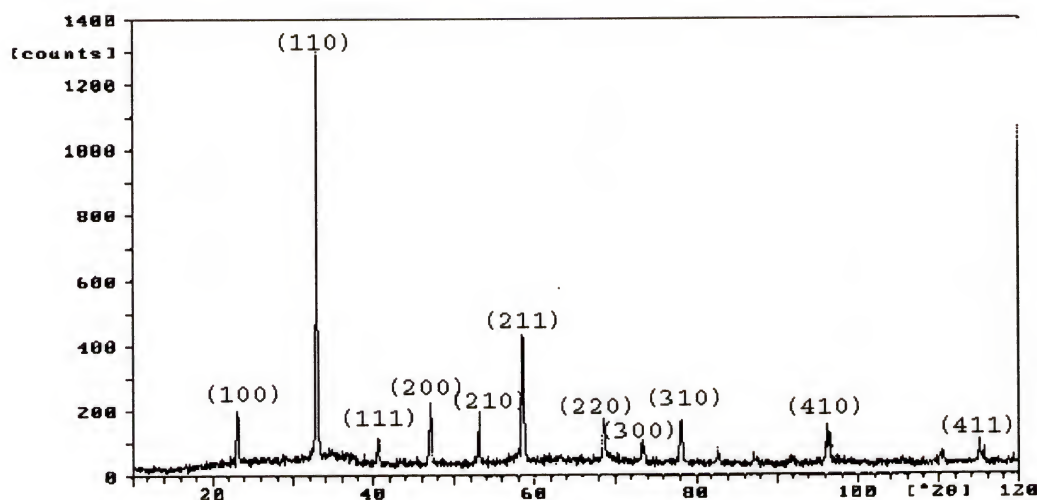
Figure 3-12. X-ray diffraction peaks of ammonium chloride deposition

3.5 Conclusions

The details of the optimization study of the two-inch reactor were given. A set of growth conditions was found that gave the optimal GaN film. The most favorable growth conditions for GaN films on sapphire substrates were a growth temperature of 950 °C, HCl/Ga ratio of 2/1 and a NH_3 flow rate of 500 sccm. The ease in scaling up to the two-inch reactor indicates that another scale-up would be possible. The maximum size the present furnace could house is a reactor for four-inch wafers. Even though LAO and LGO are not available in large sizes, the encouraging results of GaN on two-inch silicon substrates described in chapter four may necessitate a scale-up for growth on larger silicon substrates.

CHAPTER 4
GALLIUM NITRIDE GROWTH ON SILICON

4.1 Introduction

As in other semiconductor systems, epitaxial growth of GaN would ideally occur on GaN substrates cut from bulk GaN single crystals. Bulk crystal growth of GaN, however, requires extremely high pressure to maintain the nitrogen content in the crystal, rendering bulk growth extremely difficult. For this reason, the high volume production of large size, bulk GaN is improbable in the near future and the search for alternative substrates continues. Two of the main factors associated with substrate choice are cost and resulting GaN epilayer quality. Thus, the focus of this research effort is on Si substrates as they are available at low cost, high quality, large area, and large quantity, presenting many manufacturing advantages over other available substrates such as sapphire and SiC.

The disadvantages of Si as a substrate for GaN heteroepitaxy are significant. The a-plane +20.5% misfit has led people to conclude that growth of GaN directly on silicon was not likely to work well. In addition, the thermal expansion misfit between GaN (5.6×10^{-6} K^{-1}) and Si (6.2×10^{-6} K^{-1}) of 9.6% may lead to cracking upon cooling in films grown at high temperature.

Aside from the well-known potential of GaN light emitting devices, GaN FET's have shown very promising results for possible applications in high-speed, high-power devices such as wireless communications [137-139]. Silicon substrates offer some

intriguing advantages for these devices such as good thermal conductivity and low RF loss.

The integrated silicon circuit has been advancing markedly in the past decade. If GaN layers can be obtained on silicon substrates, it would be possible to obtain highly integrated circuit devices with optical signal transfer systems. In addition, optical communications devices with a highly concentrated memory would be easily fabricated.

A technique was developed to deposit GaN on Si (111) by a two-step low-temperature MOCVD step followed by a low-temperature HVPE step in the same reactor. It was found that an SiO_x compliant interface was needed to relieve stress at the substrate-film interface. It was shown experimentally and theoretically that low-temperature growth prevented the formation of SiN_x, which is detrimental to GaN epitaxy. All reports to date for low temperature VPE of GaN are of amorphous buffer layers [10]. This work is scientifically interesting as it represents the lowest reported temperature for deposition of GaN by vapor phase epitaxy. Practically, low temperature epitaxy allows deposition of GaN with low thermal stress. Furthermore, developing a low temperature deposition technology is important for increasing In incorporation into ternary $In_xGa_{1-x}N$ films.

4.2 Merged-Hydride Deposition of GaN on Si

4.2.1 Introduction

The initial stages of growth are crucial for obtaining device quality GaN layers. The initial growth step for GaN epitaxy on sapphire involves the growth of a thin (~50 nm) nucleation or buffer layer of AlN or GaN. Similar to GaN on sapphire epitaxy, the

most studied buffer layer for the growth of GaN on Si is AlN. Direct deposition of a thin

GaN or AlN buffer layer on Si, however, is accompanied by the formation of amorphous

SiN_x on the surface [76] when the surface is exposed to the nitrogen source, typically

NH_3. Sánchez-García *et al.* reported that the initial coverage of the Si surface with a few

monolayers of Al was necessary to prevent the formation of amorphous Si_3N_4 at the

interface [75]. Results of single crystal α-GaN grown on SiO_x formed on Si (111) are

presented below.

4.2.2 Experimental

In this work, two types of reactors were used to deposit GaN. The main reactor

used was a hot-wall merged-hydride reactor that can alternate between MOCVD and

HVPE. A capping GaN layer was grown in an alternate reactor that is a traditional cold-

wall MOVPE system; the different notation of MOVPE was used to denote a different

reactor. Growth conditions for the films were as follows: pressure: MOCVD @ 760

Torr, HVPE @ 760 Torr, MOVPE @ 76 Torr; V/III ratio: MOCVD 3000, HVPE 125,

MOVPE 3000; growth temperature: MOCVD 560 to 950 °C, HVPE 560 to 950 °C,

MOVPE 850 °C. Details of growth are described in chapter two.

Table 4-1. Summary of sample designation in GaN/Si growth study

Reactor	Heat Mode	Heat Source	Temperature	Gallium Source	Designation in Study
Nippon Sanso MOCVD	Cold Wall	RF	850 °C	TEGa	**MOVPE**
Custom Merged MO/Hydride VPE	Hot Wall	Resistive Heating	560 °C to 950 °C	TMGa	**MOCVD** **HVPE**

An extensive study of silicon wafer preparation was performed. It was

determined that optimal growth occurred when the substrate was cleaned in warm

trichloroethylene(TCE)/acetone/methanol and etched for one minute in HF (1%). This was followed by an in-situ hydrogen reduction for ten minutes at growth temperature. This study used two-inch Wacker n-type (phosphor) Si (111) wafers with a 2% miscut.

4.2.3 High Temperature Growth

Initial attempts at GaN growth at high temperature (900 $^{\circ}$C) on a Si substrate prepared as discussed above resulted in poly-crystalline GaN as evident by the XRD spectrum shown in figure 4-1. The deposition sequence was a high temperature layer of MOCVD GaN (900 $^{\circ}$C, 15 min) followed by a high temperature (900 $^{\circ}$C, 120 min) HVPE GaN layer. It is well known that HCl will react with Si to form volatile chlorides. Thus the intended purpose of the MOCVD layer is to protect the Si substrate from attack from the HCl atoms present in the HVPE chemistry.

Ammonia gas and TMG were sent simultaneously to the growth zone. Most likely an amorphous SiN_x layer formed at the Si/GaN interface. Single crystal growth is impeded by the growth of SiN_x islands on the surface. GaN condensing on Si covered with SiN_x does not experience an epitaxial constraint and thus grows in its hexagonal modification with some cubic grains. This is unavoidable unless the Si surface is protected against impinging nitrogen [81]. It was concluded that growth conditions were needed that avoid the formation of SiN_x at the Si surface during the initial stages of growth.

Using low temperature MOCVD at 560 $^{\circ}$C followed by high temperature HVPE at 900 $^{\circ}$C resulted in growth of poly-crystal GaN. This poly-crystal HVPE layer was caused by degradation of the MOCVD buffer layer during the long temperature ramp (3 hr) from low temperature growth to high temperature growth.
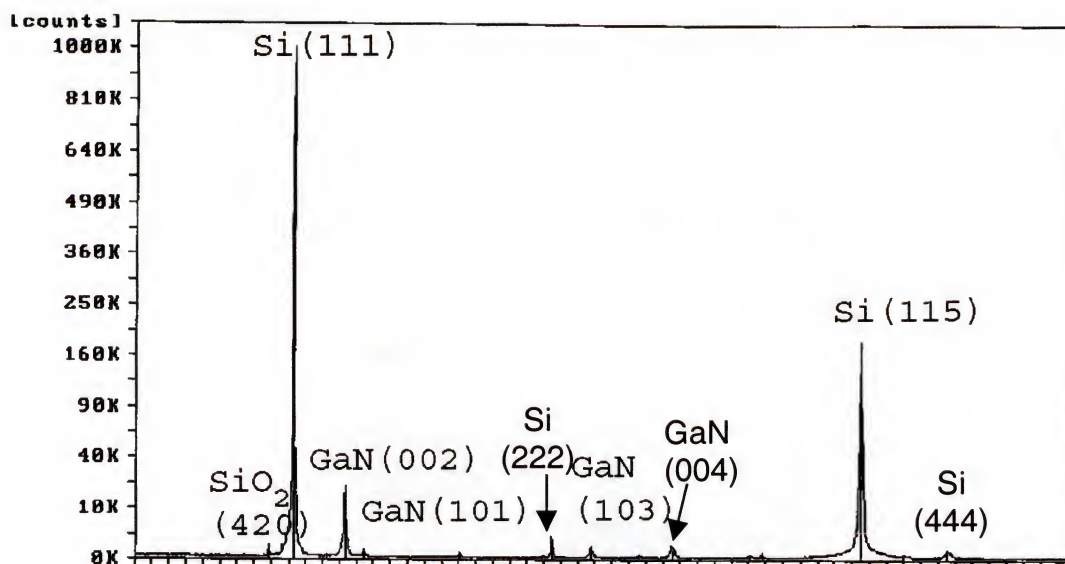
Figure 4-1. XRD spectrum of GaN deposited at high temperature on Si (111)

4.2.4 Silicon Surface Chemistry

It was also observed that growth performed at intermediate temperature (approximately 700 to 800 °C) was also of poor quality. Surprisingly, only the low temperature (560 °C) growth produced films of single crystal quality. A thermodynamic assessment of the Ga-N-O-Si system was performed using the ThermoCalc software package [65,66] to understand the chemistry at the Si/GaN interface. An equilibrium phase-diagram (figure 4-2) was generated that shows temperature versus mole fraction of Si to provide insight as to what interfacial compounds might form. To model the thermodynamics at the initial stages of growth, the mole fraction of silicon was varied as an independent axis as is seen in figure 4-9 to simulate changing surface coverage. It was estimated that at the silicon surface the system could be defined with $P_{total} = 1.0$ atm, $x_{Ga} = 0.1$, $x_O = 0.05$, and x_N was the independent variable. Chlorine was not present, as the initial growth step was MOCVD. The temperature range studied was 500 to 950 °C.

The phase diagram indicates that above 575 $^{\circ}$C, SiN$_x$ forms. Even small amounts of SiN$_x$ at the interface would cause poly-crystalline growth of the subsequent GaN as observed for medium and high temperature GaN growth.
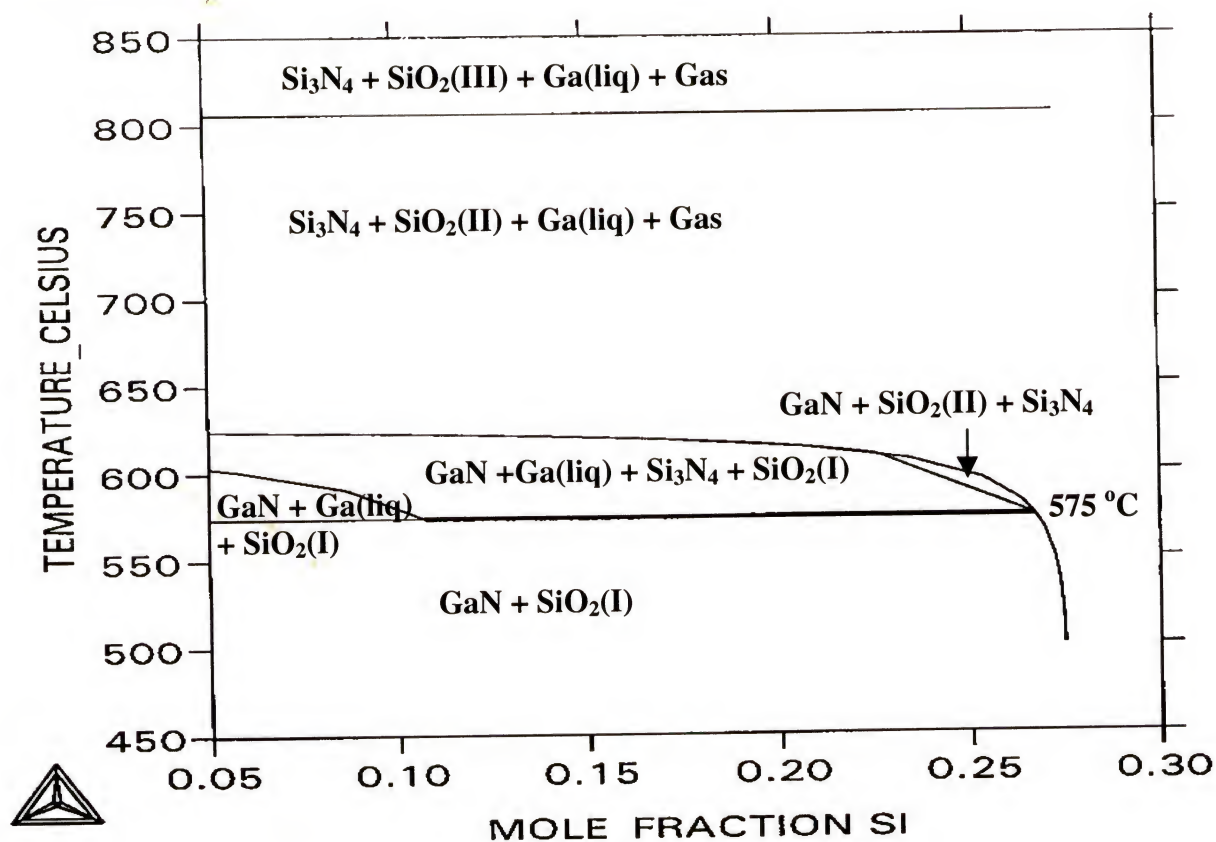
Figure 4-2. Equilibrium phase diagram of Ga-O-N-Si system

To understand the initial stages of GaN growth on Si, a thermal treatment study was undertaken. The effects of temperature, cleaning procedure, H$_2$ in-situ cleaning, and TMGa and NH$_3$ treatment on bare silicon were studied.

Figures 4-3 and 4-4 show ESCA spectra of the Si 2p$_3$ peak for bare silicon treated with and without NH$_3$ at high (900 $^{\circ}$C) and low (560 $^{\circ}$C) temperature. These samples were cleaned in warm trichloroethylene/ethanol/methanol, etched in 1% HF and in-situ

cleaned in H_2 at the anneal temperature. Analysis by ESCA was performed within 3 hr of the experimental run to minimize contamination from the ambient.

An advantage of ESCA is that it gives information on chemical states from variations in binding energies, or chemical shifts, of the photoelectron lines. The bulk Si-Si bonds have a binding energy at 100.1 eV. This peak shows a doublet splitting of the 2p subshell into $2p_{3/2}$ and $2p_{1/2}$ bands with an intensity ratio of 1:2. Emission of an electron with up or down spin from a p-type orbital creates a photoelectron with two possible energy levels. These two emission levels separated by 0.6 eV create an asymmetry in the overall Si peak.

Strained Si-Si bonds near the Si/SiO_x interface are distorted from their typical tetragonal bonding configuration. This compressive distortion results in a silicon bonding peak shifted to 102.2 eV. A strong peak observed at 104.1 eV was assigned to the Si-O bond. For samples treated in ammonia, a strong peak from the Si-N bond was observed at 103.3 eV.

By integrating the area of each peak, an estimation of the bonding configuration of the surface atoms is possible. Table 4-2 shows that nitrogen incorporates into the SiO_x film for samples annealed in NH_3. The nitrogen incorporation increases with increasing anneal temperature consistent with either increased NH_3 decomposition or N diffusion at elevated temperature.

The pre-treatment seen in figure 4-4b of warm TCE/ethanol/methanol clean, 1% HF etch, no nitridation and in-situ H_2 clean at 560 °C resulted in the highest quality GaN epitaxy. ESCA analysis indicates that the GaN was deposited on a thin SiO_x film. Only the first 5 nm of the surface are probed in ESCA due to the small escape length of the

photoelectrons. Thus, for all films an oxide or oxynitride thickness in the range of 2 nm to 3 nm can be estimated from the ratio of bulk Si bonding to silicon oxide bonding.

(a)
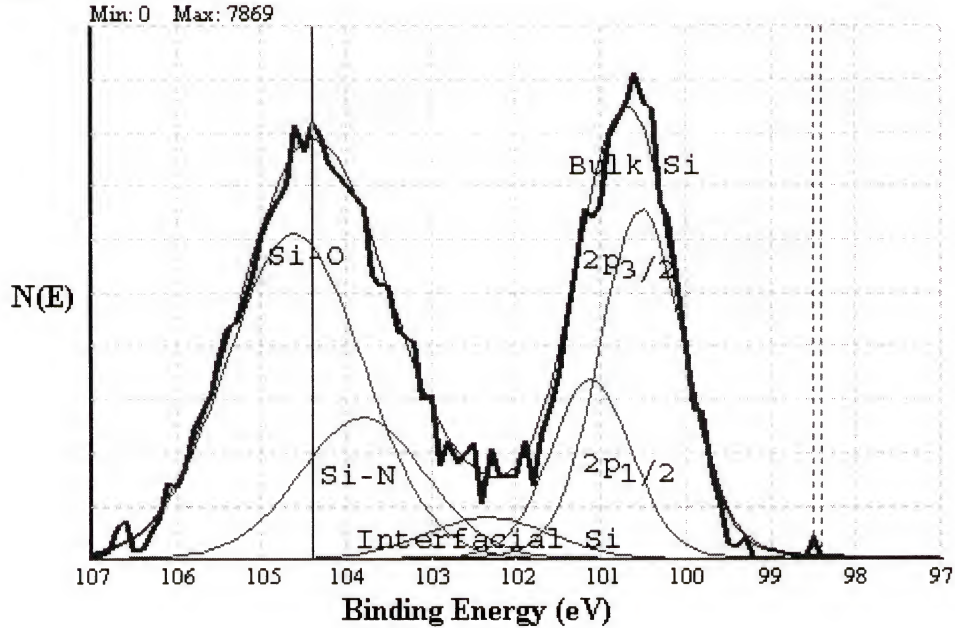
(b)

Figure 4-3.   ESCA spectra of Si 2p$_3$ peak for Si annealed at 900 $^{\circ}$C in 1.0 slm N$_2$ a) with 100% NH$_3$ at 1.0 slm b) without NH$_3$

(a)

(b)

Figure 4-4. ESCA spectra of Si $2p_3$ peak for Si annealed at 560 ^{o}C in 1.0 slm N_2 a) with 100% NH_3 at 1.0 slm b) without NH_3

Table 4-2. Comparison by ESCA of Si anneals

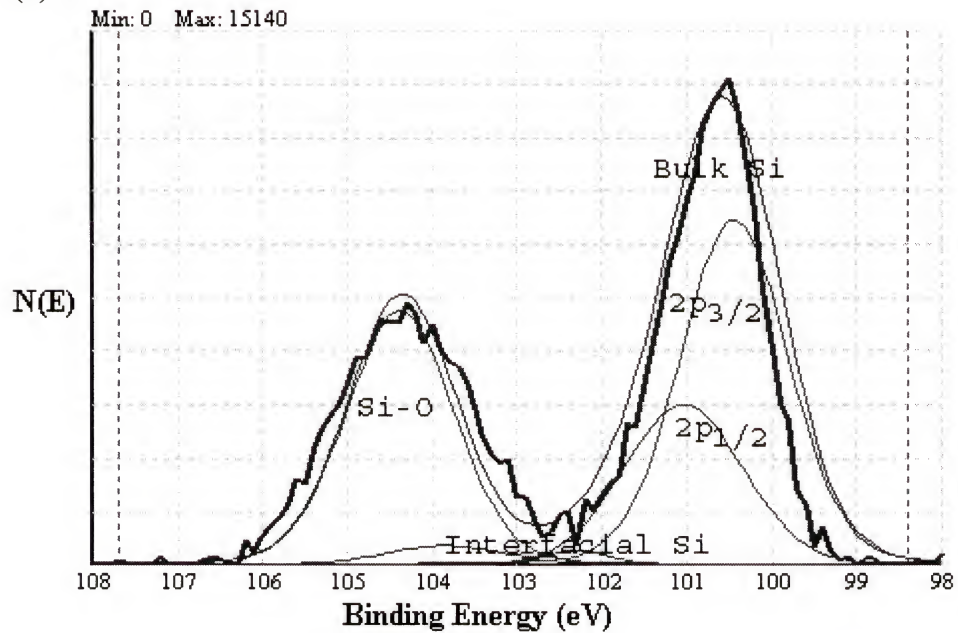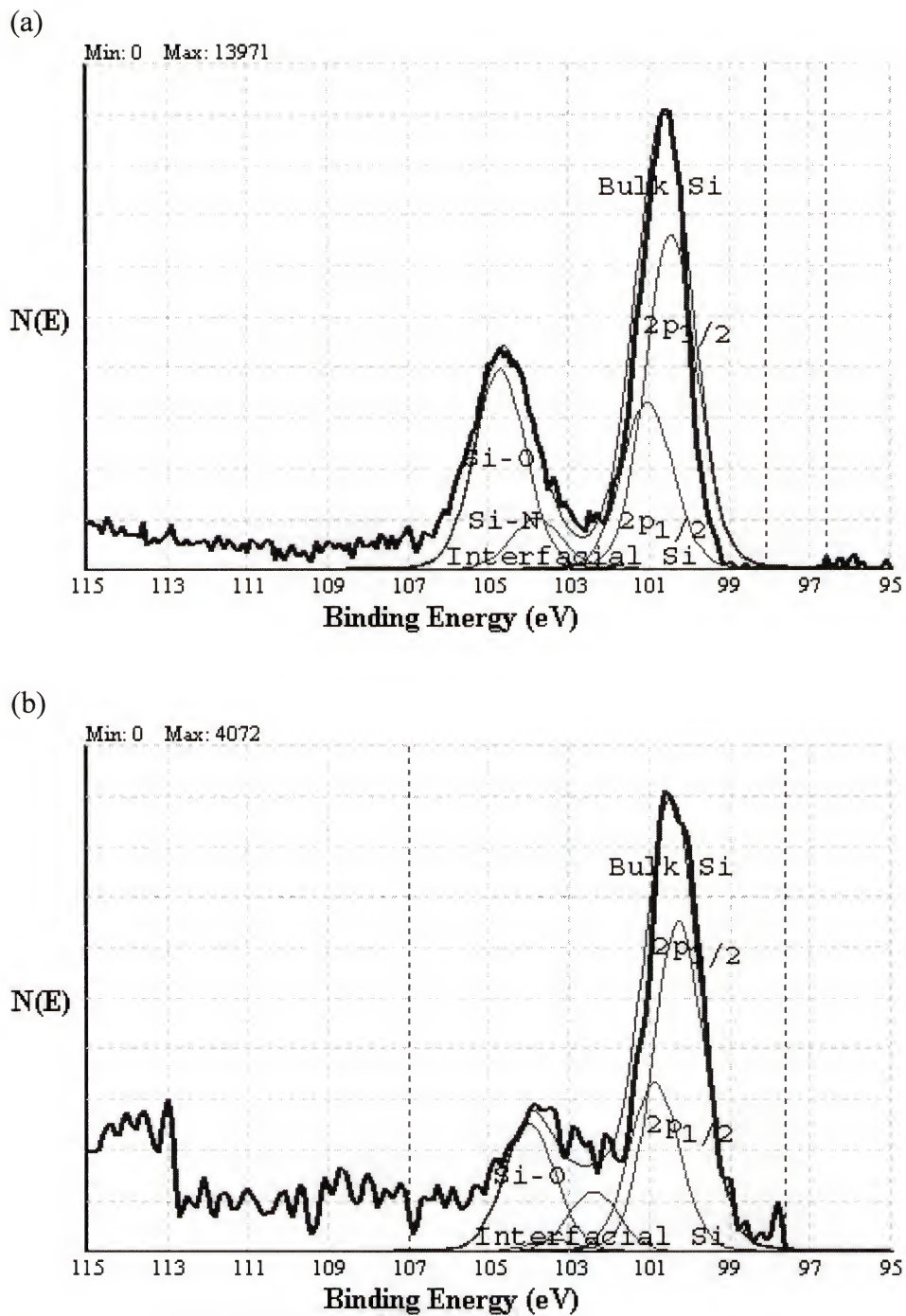| Temperature	NH$_3$	%Bulk Si Bonds	%Si-O Bonds	%Si-N Bonds
High (900 ^{o}C)	Yes	40.2	38.8	16.2
High (900 ^{o}C)	No	64.6	31.5	Negligible
Low (560 ^{o}C)	Yes	66.0	26.4	6.8
Low (560 ^{o}C)	No	71.5	18.3	Negligible

4.2.5 Low Temperature Growth

Alternatively, single crystal GaN was produced using a low temperature MOCVD layer (560 ^{o}C, 15 min) followed by a low temperature HVPE GaN layer (560 ^{o}C, 120 min). A cross-sectional SEM micrograph depicted in figure 4-2, shows a sharp interface between the MOCVD and HVPE layers. Clearly the HVPE growth rate was greatly reduced at low temperature. Most likely the reduced pyrolisis rate of TMG combined with an etching mechanism by the large number of free chlorine atoms reduced the growth rate. Another possibility is the formation of adducts that reduce the amount of Ga atoms available to form GaN at the growth surface.

The cross-sectional SEM micrograph in figure 4-2 indicates that the SiO$_x$ layer is approximately 10 nm in thickness. This thickness may be exaggerated by SEM contrast. Oxygen is always available in the merged-hydride reactor from the hot-wall quartz tube as well as other typical contamination sources. Growth on denuded wafers is planned in the near future to better understand the oxide formation mechanism. Several different cleaning/etch pre-treatments for the silicon substrates were investigated and the optimal cleaning procedure was determined to be warm (50 ^{o}C) TCE/acetone/methanol followed by a wet etch in 1% HF with a subsequent in-situ hydrogen clean. Bare silicon is extremely reactive with oxygen and thus SiO$_x$ would readily form. The phase diagram in

figure 4-2 indicates that Si-N formation is less likely at low temperature. Additionally, the gallium source is sent prior to the nitrogen source to seed the surface with gallium atoms and minimize SiN_x formation.
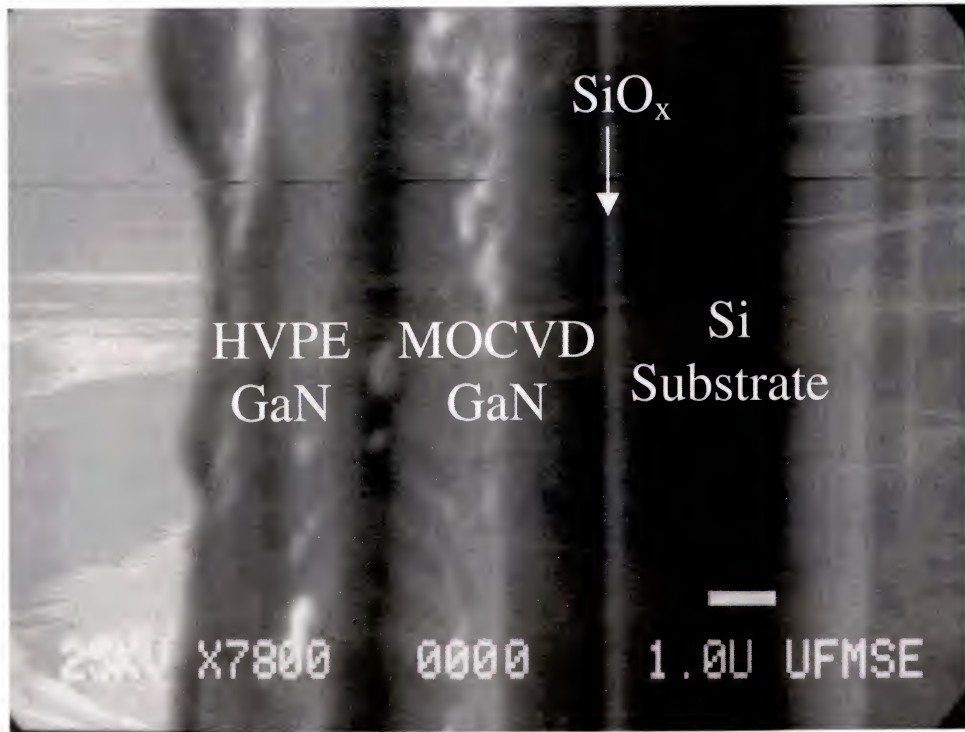
Figure 4-5. XSEM of low-temperature MOCVD/HVPE GaN

Growth parameters such as growth temperature, V/III ratio, III/Cl ratio, cleaning procedure and surface pre-treatment were optimized to provide the strongest crystalline signal by XRD. Figure 4-6 and table 4-3 illustrate that the strongest GaN signals were found when the SiO_x signal was reduced although it was never eliminated. It is possible that the SiO_x layer is beneficial as it acts as a compliant interface, reducing the stress between the GaN and the Si substrate.
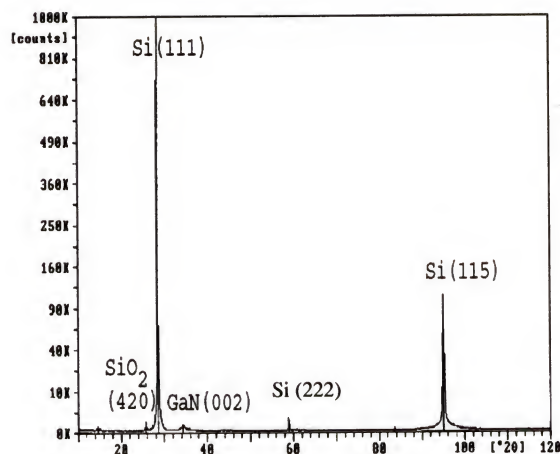
(a)   (b)
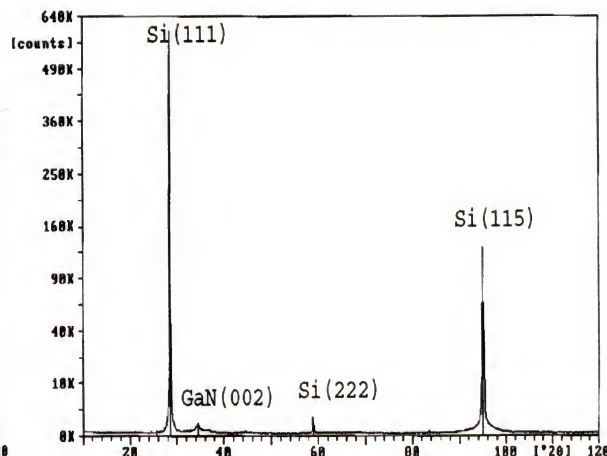
Figure 4-6.   XRD spectrum of low temperature (560 °C) HVPE/MOCVD GaN on Si (111) (a) with and (b) without NH$_3$ pre-treatment

Table 4-3. Comparison of XRD signal strength

Peak	XRD Signal Strength	
	NH$_3$ Pre-Treatment	No NH$_3$ Treatment
GaN (002)	219	3570
SiO$_2$	630	620

The strongest crystalline signal by XRD (figure 4-7) was found when wafers were: cleaned in warm TCE/Acetone/Methanol; etched in HF(1%); pre-treated in-situ with hydrogen (10 min) had no NH$_3$ pretreatment, and then films were grown in the sequence 30 min MOCVD (4% H$_2$ / basis N$_2$ carrier gas) growth followed by 2 hr HVPE (4% H$_2$ / basis N$_2$ carrier gas) growth. The V/III ratio for MOCVD was 3000 and HVPE was 125.

Figure 4-8 shows a surface Auger spectrum of the GaN surface. The absent chlorine peak indicates that within the limits of AES (~0.1%) there is no chlorine present

in the film. As expected, the as-grown sample surface contained significant oxygen (O_{KLL}, 504 eV) and carbon (C_{KLL}, 263 eV) contamination due to exposure to air.
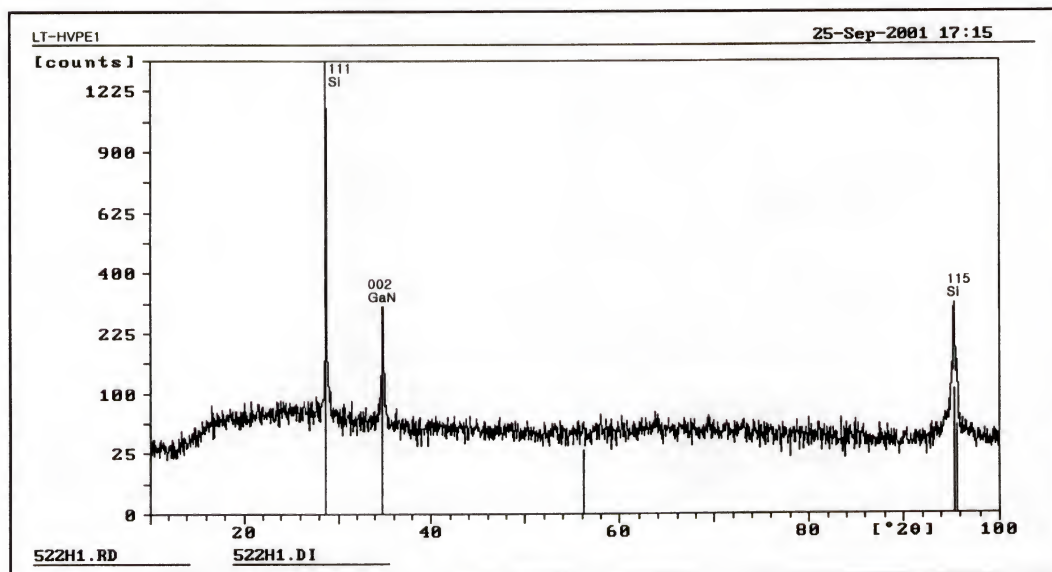
Figure 4-7. LRXRD spectrum GaN grown on (111) Si at 560 ^{o}C
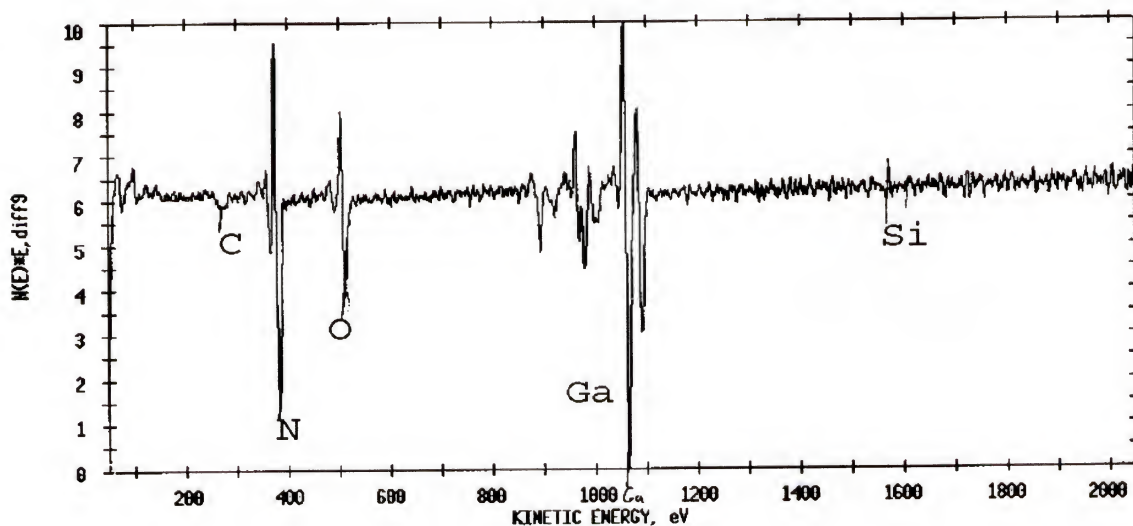
Figure 4-8. AES spectrum of the GaN surface with no pre-sputtering cleaning

The XPS spectrum in figure 4-9 provides confirmation that in the near surface region of the GaN that there is no chlorine detected within the limits of XPS (~0.2 %).

This oxygen peak seen in figure 4-9 is attributed to physisorption that occurred when the sample was removed from the reactor and exposed to the atmosphere. The concentration of the physisorbed oxygen layer is exaggerated in figure 4-9 because XPS only measures roughly the first 5 nm of the surface.

Figure 4-9. GaN surface XPS spectrum confirms no chlorine in film

Figure 4-10. AFM of GaN grown on (111) Si (RMS roughness = 1.497 nm)

All growths described had uniform coverage on 2" Si (111) substrates. Additionally, the GaN surface was specular and smooth as judged by visual inspection and supported by examination by AFM (figure 4-10).

An XTEM image is shown in figure 4-11a. This micrograph shows that dislocations form at the substrate/film interface located at the bottom of the picture and thread into the film. More importantly, the sharp selected area diffraction pattern in figure 4-11b provides confirmation that the GaN film is single-crystal.

(a)   (b)

0.15 µm
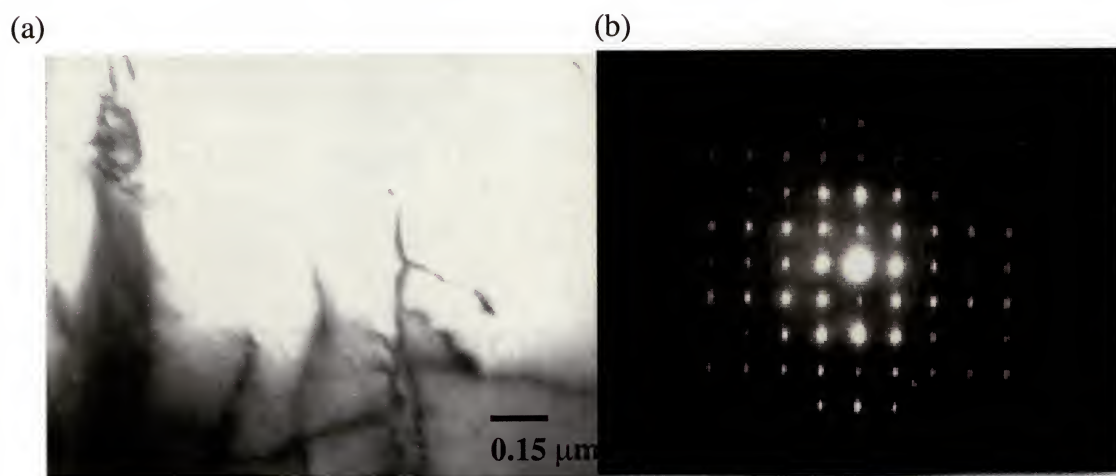
Figure 4-11. TEM <11-20> micrographs (a) threading dislocation in XTEM of GaN/Si
(b) SAD indicates that GaN is single crystal

4.2.5 High Temperature MOVPE on MOCVD/HVPE Films

Low temperature MOCVD/HVPE GaN/Si 2" wafers grown in the merged-hydride reactor were transferred to the commercial cold-wall MOVPE system. The growths were carried out at 850 ^{o}C for 30 min to 3 hr. All films were single-crystal although films thicker than 1 µm showed cracking from thermal stress upon cooling. All

films were specular by visual inspection and figure 4-12 shows that strong (0002) and (0004) GaN peaks are present indicating excellent crystal quality.
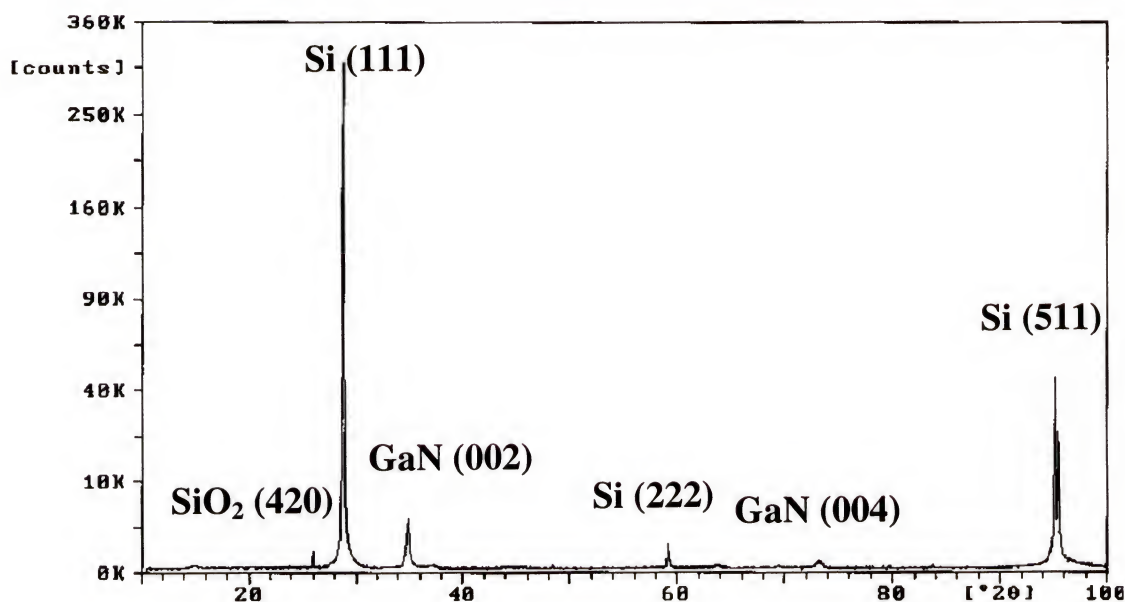
Figure 4-12. XRD of 850 °C MOVPE GaN on 560 °C MOCVD/HVPE GaN/Si film

4.2.6 High Temperature MOVPE Buffer Layers

GaN layers were grown on Si (111) substrates in the cold-wall MOVPE reactor at 850 °C and transferred to the merged-hydride reactor for HVPE growth at 560 °C. This reversed sequence was used to gain more insight into the chemistry and mechanisms of growth on silicon. In this sequence, the low-temperature MOCVD step was not needed to protect the Si substrate from attack from HCl. The SiO_x signal was eliminated when the MOVPE growth sequence was nitridation, low-temperature (560 °C) GaN buffer-layer, followed by a high-temperature (850 °C) MOVPE layer.

The structural quality of this film is appears excellent as judged by the LRXRD in figure 4-13 that shows a strong (0002) GaN single-crystal peak. Furthermore, figure 4-13

indicates that by using the commercial cold-wall reactor that the SiO_x signal could be eliminated. The removal of oxygen from the system may be explained by the rapid temperature ramp times by RF heating, reduced reactions with the cold quartz walls, or the decreased oxygen impurity levels in a low-pressure system. Preliminary PL results showed that films that eliminated the oxide layer exhibited a yellow luminescence signal. This may indicate that the oxide layer prevents the formation of a certain defect that is responsible for the undesirable yellow emission. Details of this early work were not available as of this writing.
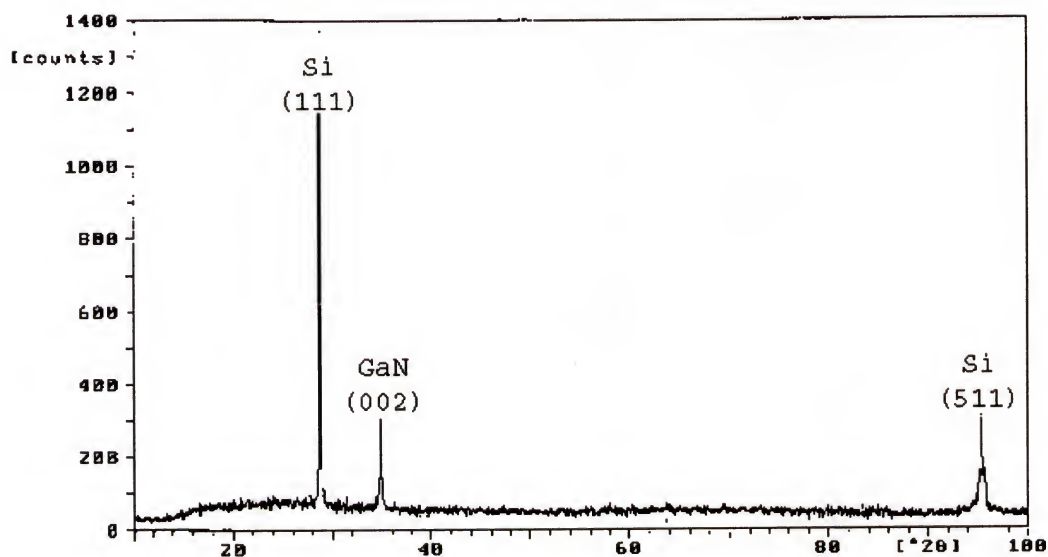
Figure 4-13. XRD of LT-HVPE on HT-MOVPE on Si (111)

4.3 High Temperature MOVPE on AlN/Si

Aluminum nitride buffer layers are traditionally used for GaN deposition on Si or sapphire substrates. Using a proprietary process, TDI Inc. (Gaithersburg, MD) deposited (0002) AlN on (111) Si and transferred the sample to the University of Florida. This sample used as a pseudo-substrate in the cold-wall MOVPE reactor for GaN deposition at

850 °C. Details of growth were described at the beginning of the chapter. The films were specular and by LRXRD (figure 4-14) had sharp (0002) and (0004) GaN diffraction peaks indicating the sample was of high crystal quality.
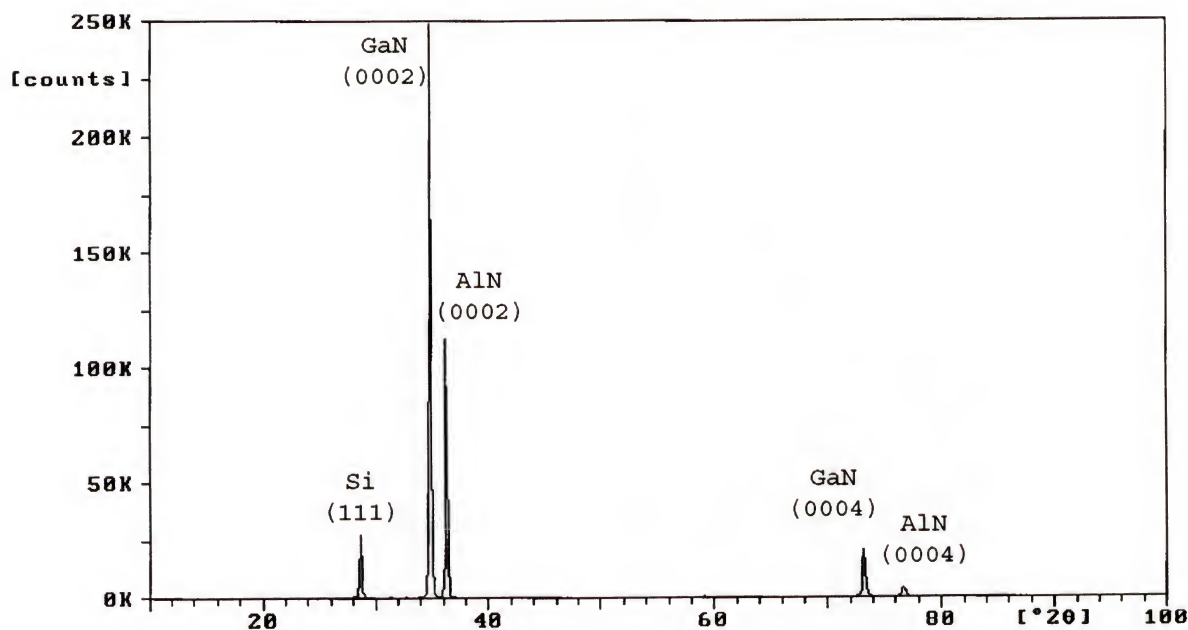
Figure 4-14. LRXRD of single crystal MOVPE GaN grown at 850 °C on AlN/Si (111)

4.4 Conclusions

It was shown that epitaxial GaN could be fabricated by a low-temperature MOCVD/HVPE deposition sequence in a hot-wall merged-hydride reactor. Measurements revealed that a thin compliant SiO_x layer was an effective intermediate layer for the GaN film grown epitaxially on Si. The GaN films had good adhesion and no films from optimized growths were observed to peel off the substrates. This represents the lowest deposition temperature reported for single crystal GaN by vapor phase epitaxy.

These encouraging results open a number of possible research pathways. Results of transfer to the cold-wall MOVPE reactor for high-temperature growth are excellent.

As the concept has been proven repeatedly, the next stage of research should be the fabrication of devices. A HEMT type structure could easily be fabricated by depositing an undoped, very thin GaN layer followed by a low-doped n-type, thin AlGaN layer on LT-GaN/Si. Performance of the HT-MOVPE/LT-HVPE/LT-MOCVD-GaN/Si structure would indicate if this is a practical technology.

In the merged-hydride system the investigation of AlN and AlGaN low-temperature epitaxy should be explored. Finally, further encouraging results of III-nitride epitaxy on two-inch silicon substrates may necessitate a reactor scale-up for growth on larger silicon substrates.

CHAPTER 5
THERMAL STABILITY OF GALLIUM NITRIDE

5.1   Introduction

Thermal decomposition of solids is of practical interest because of its fundamental presence in the fabrication, application and degradation of solid-state materials. Although factors such as heat input, chemical reaction, and gas phase mass transport exist at each stage of thermal decomposition, typically the evaporation step is the controlling mechanism. Volatilization is composed of three primary steps: (1) the transfer of thermal energy into the solid, (2) surface processes leading to formation of volatile molecules, (3) transport of vapor away from the surface.

The recent development of GaN based blue light emitting diodes (LEDs) and lasers [32,33,140] and high-power/high-temperature electronics [138,139] has produced an intense interest in the column III-nitrides. The thermal and chemical stabilities of GaN and related materials are important to growth and device processing, and is not well understood. As examples, the mechanisms of growth and the role of post-growth annealing in defect reduction are related to thermal stability as well as differences in implant activation pathways (Si, Mg) and the interfacial reactions between GaN and metal contacts. A detailed study of the stability of GaN in various ambients is important to the understanding of these issues as well as the future development of complex devices.

On heating, GaN can undergo the following possible decomposition routes depending on the annealing conditions (figure 5-2): etching (dissociative and direct sublimation) or decomposition accompanied by nitrogen-saturated liquid gallium droplet formation [141-149]. A series of decomposition experiments were performed that revealed the decomposition or etching of GaN depending on the nature of the ambient gas, annealing temperature, and growth technique.

5.1.1 GaN Sample History

For comparison GaN HVPE samples using the merged-hydride system and MOVPE samples using the Nippon Sanso commercial system were prepared. No low-temperature buffer layers were used, however, a 5 min pre-growth nitridation was performed on the c-plane sapphire at growth temperature. A comparison of the samples used in this sample is provided in table 5-1. The two-inch diameter HVPE sample was diced into a number of approximately 1x1 cm samples that were used in the thermal stability study. The MOVPE samples were diced prior to growth but the samples were loaded simultaneously so the GaN film could be deposited in the same growth run to reduce error in the study.

Table 5-1. Summary of sample designation in thermal stability study [142]

Reactor	Growth Pressure (Torr)	Heat Mode	V/III	Growth Temp. (^{o}C)	Gallium Source	Film Thickness (μm)	Designation in Study
Nippon Sanso MOCVD	760	Cold wall-RF	3000	850	TEGa	1	**MOVPE**
Custom Merged Hydride VPE	76	Hot wall-resistive heating	125	950	TMGa	10	**HVPE**

MOVPE is the standard method for producing GaN samples. HVPE is a common alternative method for producing thicker GaN samples. By altering the reaction chemistry HVPE films have higher growth rates but can sacrifice structural quality. The AFM (tapping mode) pictures in figure 5-1 show that the MOVPE films are smoother when compared to the HVPE films.

5.1.2 Thermal Behavior

As illustrated in figure 5-2, decomposition of GaN is predicted to be thermodynamically favorable. The Gibbs free energy values, ΔG^o, were calculated for a reaction at 900 ^{o}C. Kinetic effects can be important, however, as highly activated barriers can exist. A detailed thermodynamic analysis was first performed for the Ga-N system.
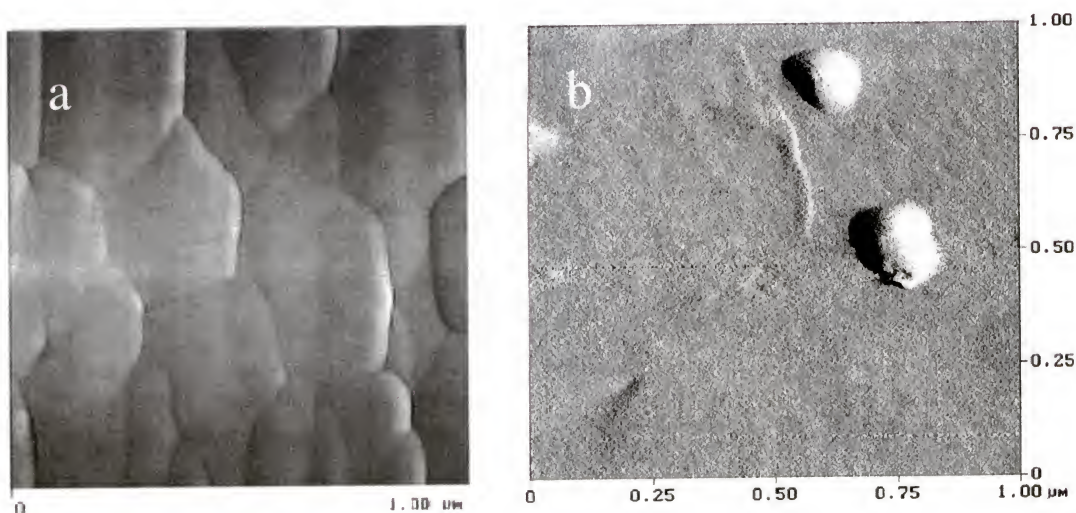
Figure 5-1. AFM micrographs of as-received GaN grown by a) MOVPE b) HVPE

Equilibrium between a solid and ambient gas occurs when the number of molecules of each species evaporating per unit time is equal to the number condensing,

thus the net rate is zero. A thermodynamic assessment of the Ga-N system suggests that the following reaction is the most thermodynamically favorable for GaN decomposition at atmospheric pressure [143]

$$GaN = Ga^l + \frac{1}{2} N_2^v \qquad (5.1)$$

The equilibrium partial pressures of GaN and Ga are relatively small under these conditions.

| GaN |
| Elevated Temperature |

| Sublimation |

| Decomposition |

$$GaN = Ga(g) + \frac{1}{2} N_2(g)$$
$$\Delta^o G(800C) = +55 \text{ kJ/mol}$$

$$GaN = Ga(l) + \frac{1}{2} N_2(g)$$
$$\Delta^o G(800 \ ^o C) = -94 \text{kJ/mol}$$
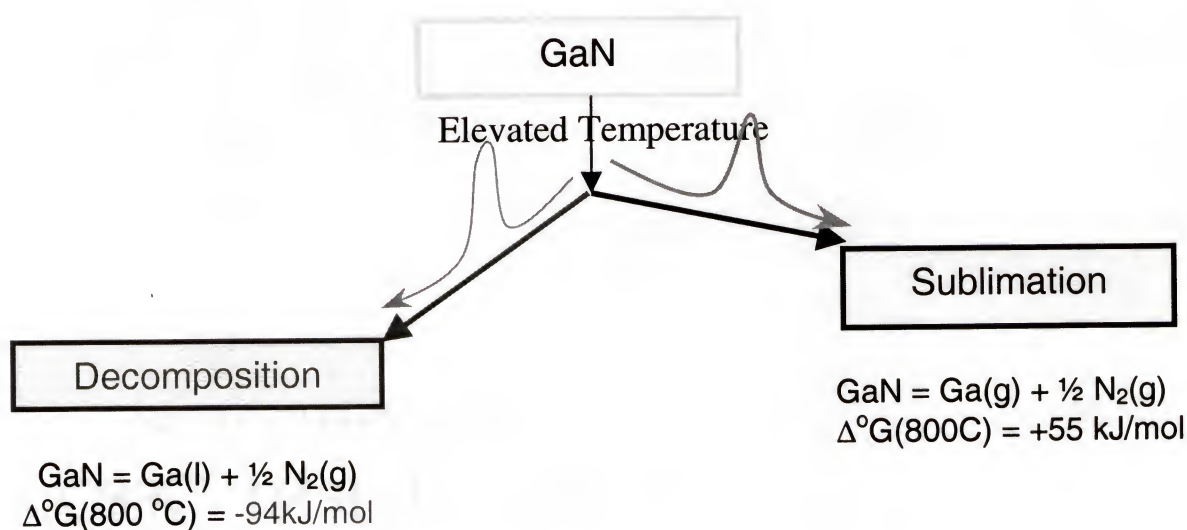
Figure 5-2. GaN when exposed to elevated temperature can follow a decomposition or sublimation mechanism. [143]

Sublimation occurs when a two-component solid mixture evaporates without change in composition. It is found that if the vapor lost upon sublimation has the same composition as the solid then the molecules of the species are leaving the surface with equal efficiency. This sublimation can occur for example by the simple dissociative reaction

$$GaN^s = Ga^v + \frac{1}{2} N_2^v \qquad (5.2)$$

Naturally it is assumed that the GaN used is stoichiometric [144]. This congruent sublimation occurs when

$$x(solid) = x(vapor) \qquad\qquad (5.3)$$

where x is an overall composition of the phase.

It has been suggested that the high thermal stability of GaN in vacuum, inert gases and reactive gases is due to its wurtzite structure that exhibits strong covalent bonds between each nitrogen atom and its four nearest neighbors, as well as the long distances between nitrogen atoms in the lattice [141].

5.2 Details of Thermal Annealing Study

This section reports on a study of GaN decomposition in HCl, H_2, NH_3, and N_2 (the most common processing ambients). A summary of the experimental conditions is given in table 5-2 [142]. The samples used in this study were loaded as grown, that is, the samples received no additional cleaning. The furnace was pre-heated to the particular anneal temperature. The load-lock system allowed samples to be loaded into the hot furnace. The load-lock was pumped and purged five times to prevent contaminating the system with oxygen. The sample was loaded with the magnetic arm and after allowing approximately 5 min for the temperature in the furnace to stabilize, the anneal gas was sent to the system for 30 min. The system was flushed with nitrogen for 5 min after the experiment was completed to remove any hazardous gases. The sample was then unloaded and the new temperature was set.

The differences between MOVPE and HVPE films in these ambients were compared. Additionally, it was investigated how MOVPE and HVPE films compare to theoretical calculations. All films were characterized by use of AFM and SEM for

surface structure, and AES, SEM with EDS for chemical composition. Samples were typically sprayed with methanol to remove particles prior to analysis.

Table 5-2. Annealing conditions of MOVPE and HVPE GaN samples

Samples	MOVPE and HVPE GaN
Conditions	HCl 760 Torr H_2; 760 Torr NH_3; 760 Torr N_2; 760 Torr and 76 Torr; with and without InGa doplet
Flow-rates	50 sccm HCl (10% HCl/basis N_2) + 3.2 slm N_2 3.2 slm 100% H_2 500 sccm 100% NH_3 + 3.2 slm N_2 3.2 slm N_2
Time	30 min
Temperature	variable but in range of 500 to 1400 ^{o}C

5.2.1 HCl Anneal of MOVPE GaN

A comparison of MOVPE GaN for different anneal temperatures (30 min) was performed under HCl gas. As is evident from the series of SEM micrographs shown in figure 5-3, the surface of the GaN was still intact at 800 ^{o}C. At 900 ^{o}C, these films began to show a sublimation mechanism. EDS analysis revealed that at higher temperatures Ga and N leave the surface simultaneously as a gas, indicative of a congruent sublimation mechanism.

This is seen in figure 5-3a-c where the white area is GaN, the gray is the original GaN, and the black is the sapphire substrate. At 900 ^{o}C nearly 1/4 of the film area was sublimated leaving only the sapphire substrate (black areas). By 965 ^{o}C 3/4 of the film area was sublimated. The SEM micrographs and the estimations of sample vaporization are representative of the whole sample. Since no Ga droplets are present this is not a decomposition mechanism. The surface of the MOVPE films has excellent structural quality and specular surfaces that possess high kinetic barriers that prevent the GaN from

reaching equilibrium during annealing. Thus HCl anneals of MOVPE GaN follow a sublimation route.
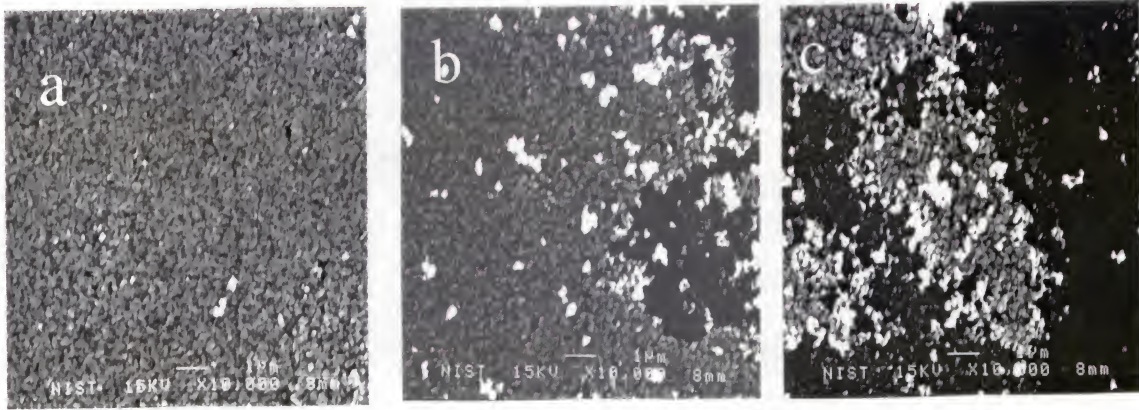
Figure 5-3.   SEM micrographs of MOVPE GaN annealed in HCl (a) 800 ^{o}C (b) 900 ^{o}C (c) 965 ^{o}C
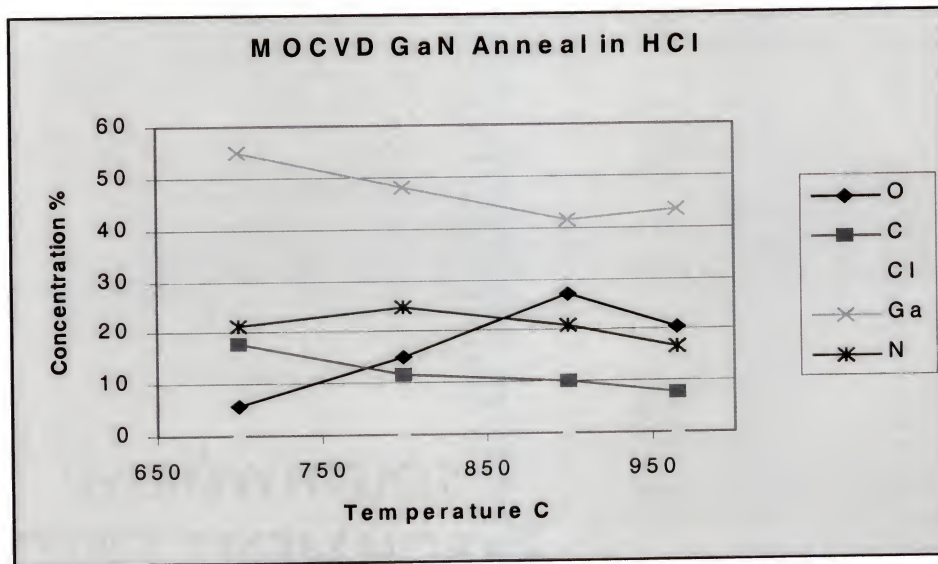
Figure 5-4.   AES measurement of the surface concentration of O, C, Cl, Ga, and N atoms for MOVPE GaN annealed in for 30 min in HCl

Figure 5-4 shows AES of MOVPE GaN annealed in HCl exhibit slight sublimation (N and Ga loss) beginning at 800 ^{0}C. This agrees with the previous SEM/EDS results. Thus HCl anneals of MOVPE GaN follow a sublimation route that can be expressed as the following simplified reaction:

$$GaN\,^s + HCl^v = GaCl^v + 1/2\,H_2{}^v + 1/2N_2{}^v \tag{5.4}$$

This decomposition mechanism was supported performing equilibrium closed box-type calculations for the GaN and HCl mixtures using thermodynamic data for solid GaN [142] and for all possible gas species in the Ga-N-H-Cl system [65,66,143].

5.2.2 HCl Anneal of HVPE GaN

Figure 5-5a shows Ga droplets on top of GaN hexagonal pyramids. Nitrogen is desorbs from the surface, leaving N-saturated gallium liquid droplets on the surface that solidify upon cooling. In figure 5-5b, hexagonal pyramids similar to those in figure 5-5a are observable. Thus at high temperature, decomposition occurs for HVPE films under HCl gas. In figure 5-6, AES shows decomposition (nitrogen decrease) of the GaN at higher temperatures.
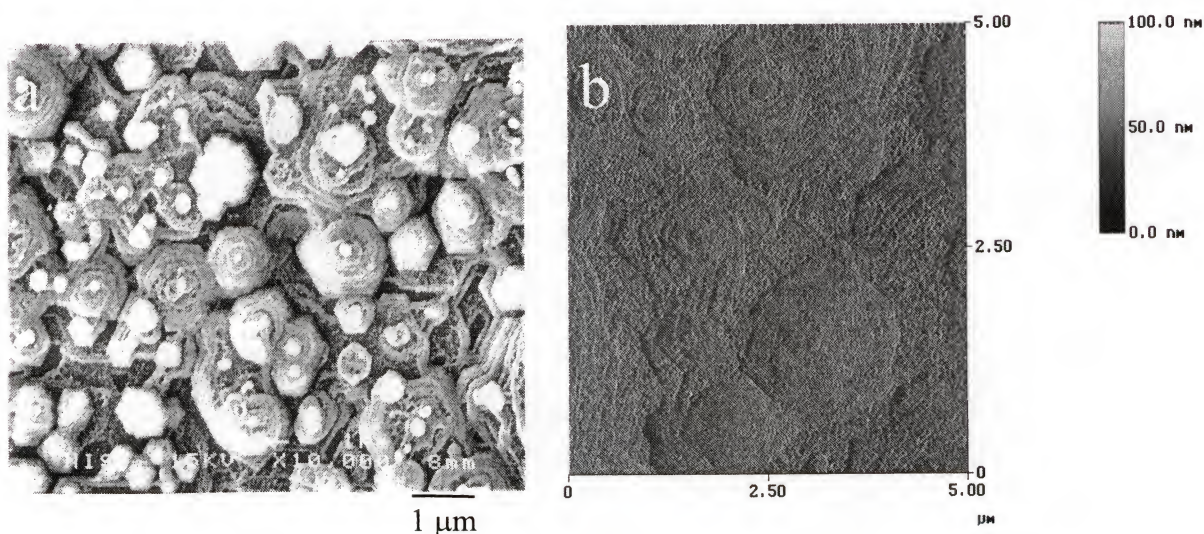
Figure 5-5. HVPE GaN annealed in HCl at 965 °C a) SEM b) AFM

A plot of the AFM RMS roughness as a function of anneal temperature shows the difference between MOVPE and HVPE films (figure 5-7a). MOVPE films begin to roughen above 900 °C as the sublimation mechanism takes over. Figure 5-7a also shows

that the HVPE films begin to roughen at 800 °C. Comparatively the AFM picture in

figure 5-7b below shows the MOVPE surface is still intact at 900 °C in an HCl gas

stream.
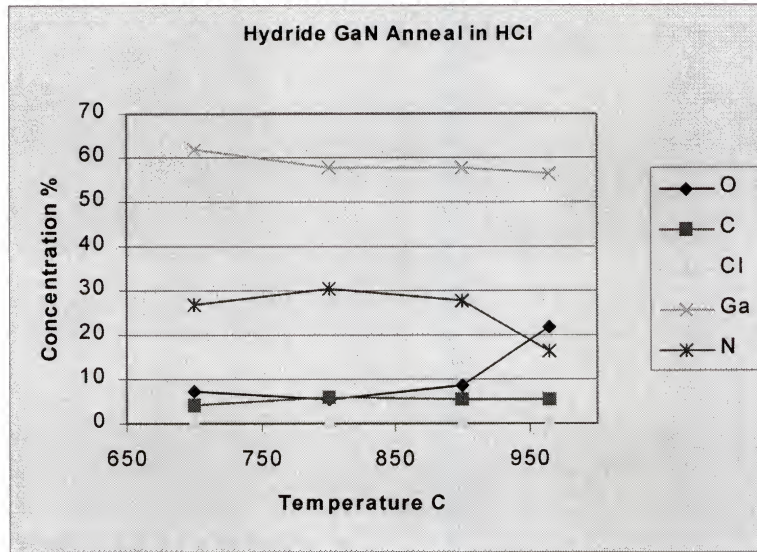
Figure 5-6.   AES measurement of the surface concentration of O, C, Cl, Ga, and N atoms
for HVPE GaN annealed in for 30 min in HCl
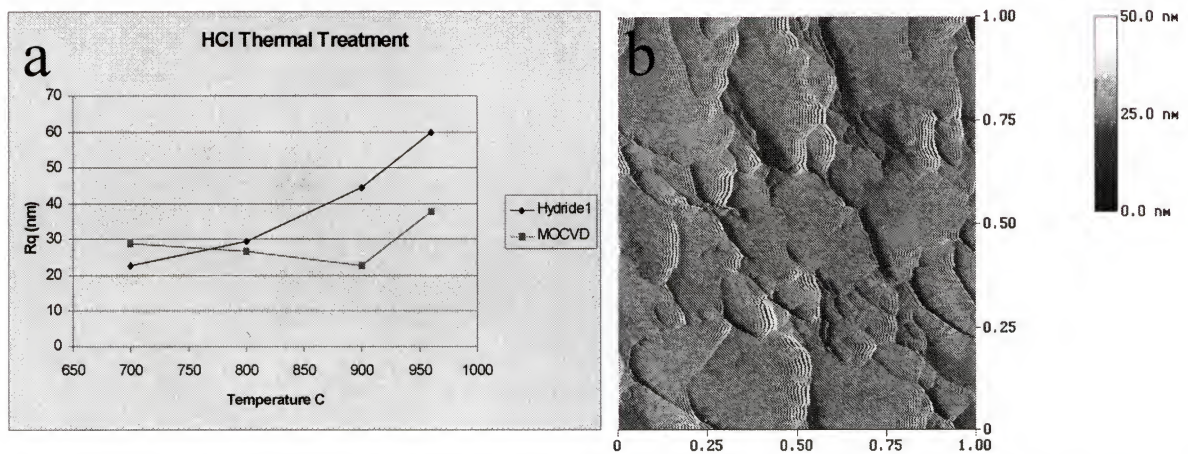
Figure 5-7.   GaN annealed in HCl a) RMS roughness as a function of anneal temperature
for MOVPE and HVPE GaN as detected by AFM b) AFM micrograph of
MOVPE sample annealed at 900 °C

The reaction of HVPE GaN film with the HCl gas can be expressed by two independent reactions:

$$GaN^s + HCl^v = GaCl^v + 1/2 \ H_2{}^v + 1/2N_2{}^v \qquad (5.5a)$$

$$GaN^s = Ga^l + N_2{}^v \qquad (5.5b)$$
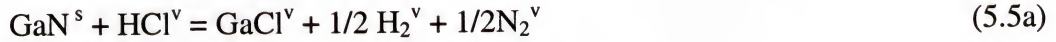
5.2.3   H$_2$ Anneal of MOVPE GaN

For MOVPE GaN films annealed in H$_2$ to 700 ^oC, no change in film composition or morphology is observed. AES (figure 5-8) shows that at 900 ^oC, Ga and N have completely left the surface as a gas, resulting in a GaN surface that is entirely sublimated.
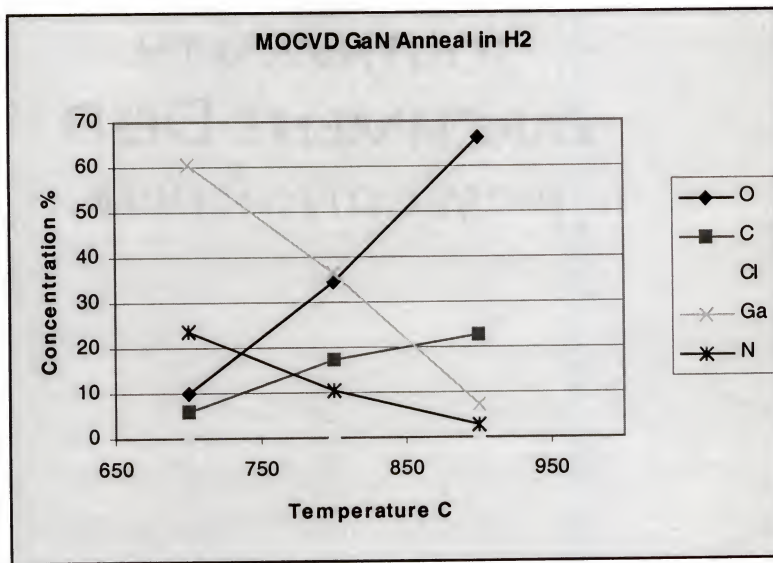
Figure 5-8.   AES measurement of the surface concentration of O, C, Cl, Ga, and N atoms for MOVPE GaN annealed in for 30 min in H$_2$

SEM of MOVPE GaN annealed in H$_2$ at 800 ^oC (figure 5-9a) shows partial sublimation of GaN (white areas = GaN) with no Ga droplets observable by EDS. SEM of 900 ^oC in H$_2$ anneal (figure 5-9b) agrees with the AES analysis as GaN is nearly completely sublimed and only the substrate (black area) remaining.
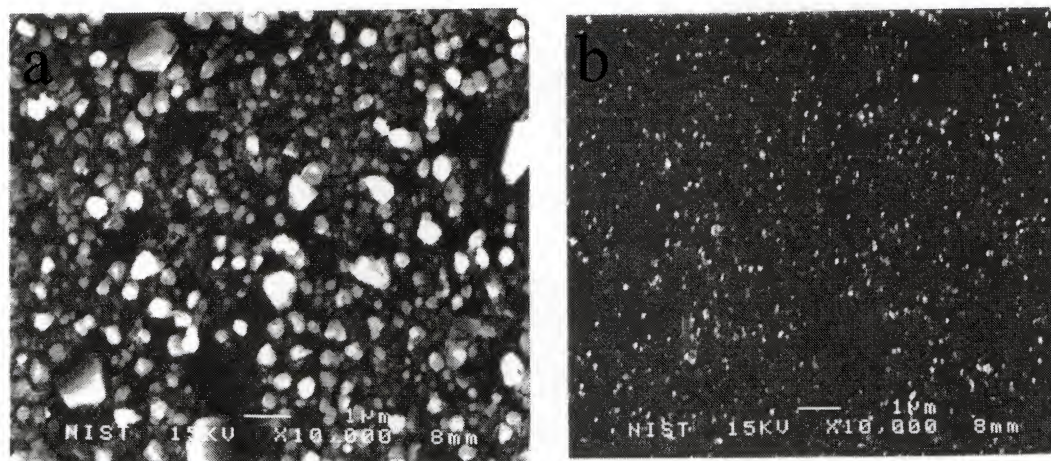
Figure 5-9. SEM micrograph of MOVPE GaN annealed in H_2 at a) 800 ^{o}C b) 900 ^{o}C
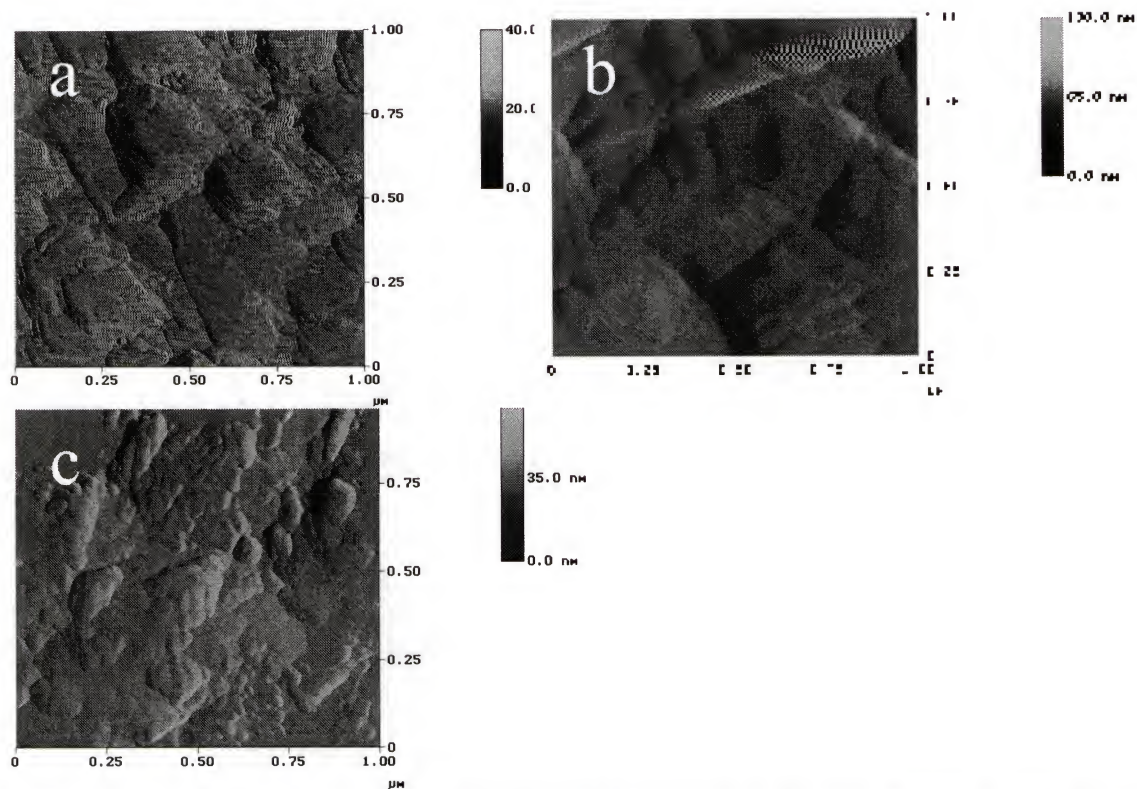
Figure 5-10. AFM micrograph of MOVPE GaN annealed in H_2 at a) 700 ^{0}C b) 800 ^{0}C c) 900 ^{0}C

Figure 5-10 shows that the surface morphology deteriorates as the GaN

sublimation rate increases with anneal temperature. By 900 ^{o}C only the substrate

remains.   The sublimation reaction for the MOVPE film can be summarized by three

independent reactions:

$$GaN^s = Ga^v + \frac{1}{2} N_2^v \tag{5-5a}$$

$$GaN^s + H_2^v = \frac{1}{2} GaH^v + \frac{1}{2} N_2^v + \frac{1}{2} H_2 \tag{5-5b}$$

$$3H_2^v + \frac{1}{2} N_2^v = 2 NH_3 \tag{5-5c}$$
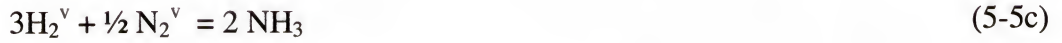
5.2.4 H$_2$ Anneal of HVPE GaN

Figure 5-11b shows that decomposition of HVPE GaN annealed in H$_2$ starts at

800 ^{0}C, evident by the small size Ga droplets (white areas) forming at defects in the film.

HVPE films typically have higher defect densities than MOVPE films.   SEM contrast

allows the island growth and dislocation defects to be discernible.   These defects are

formed during three-dimensional island growth.   Weak bonds at these defects lower the

kinetic barriers at the surface.   Thus annealing of HVPE films appears closer to

thermodynamic equilibrium (decomposition).
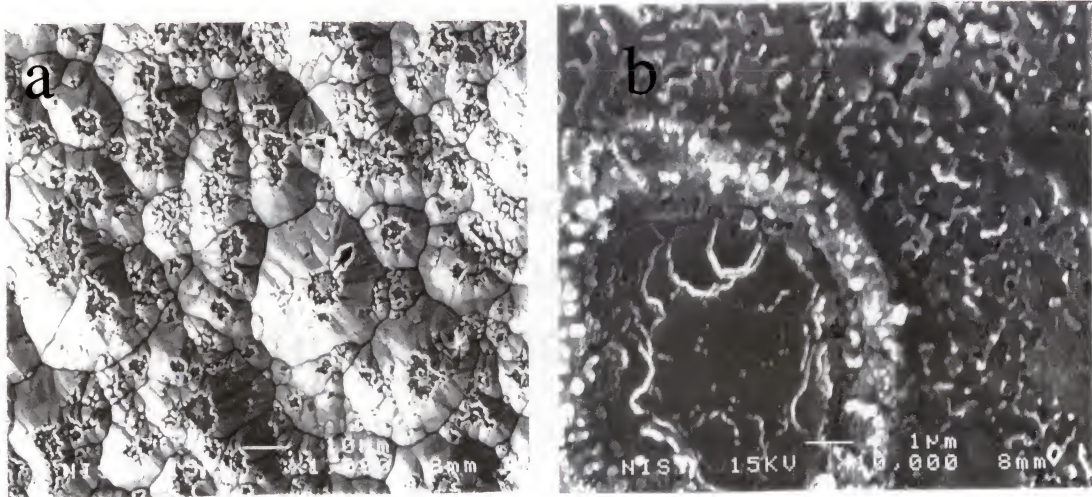
Figure 5-11. SEM micrograph of HVPE GaN annealed in H$_2$ at a) 700 ^{0}C b) 800 ^{0}C

As evident in the SEM micrograph displayed in figure 5-12b, HVPE GaN decomposition is accompanied by formation of large Ga droplets (~100 μm) on the surface. This is also evident in the AES spectrum shown in figure 5-12a, which shows nitrogen loss while the Ga concentration remains constant.
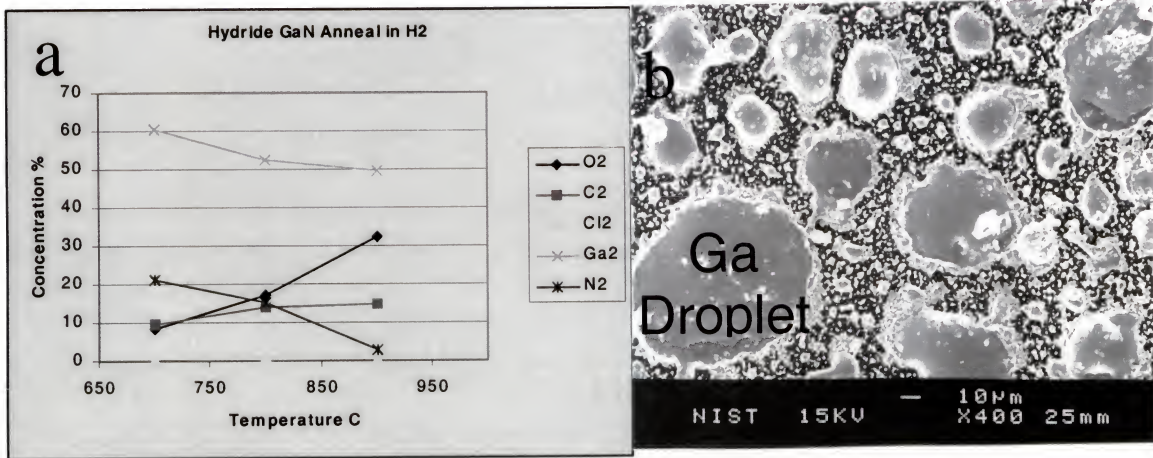
Figure 5-12. HVPE GaN annealed in H_2 a) AES measurement of the surface concentration of O, C, Cl, Ga, and N atoms b) SEM micrograph of sample annealed at 900 ^{o}C

From figure 5-13a-c it is seen that the HVPE films roughen as they decompose. In figure 5-13d, the onset of sublimation for MOVPE films (above 800 ^{o}C) is approximately 100 degrees later than decomposition for HVPE films (above 700 ^{o}C). The decomposition reaction of GaN in hydrogen can be expressed as these three independent reactions:

$$GaN^s = Ga^l + \frac{1}{2} N_2^v \qquad\qquad (5\text{-}6a)$$

$$GaN^s + H_2^v = \frac{1}{2} GaH^v + \frac{1}{2} N_2^v + \frac{1}{2} H_2 \qquad\qquad (5\text{-}6b)$$

$$3H_2^v + \frac{1}{2} N_2^v = 2 NH_3 \qquad\qquad (5\text{-}6c)$$
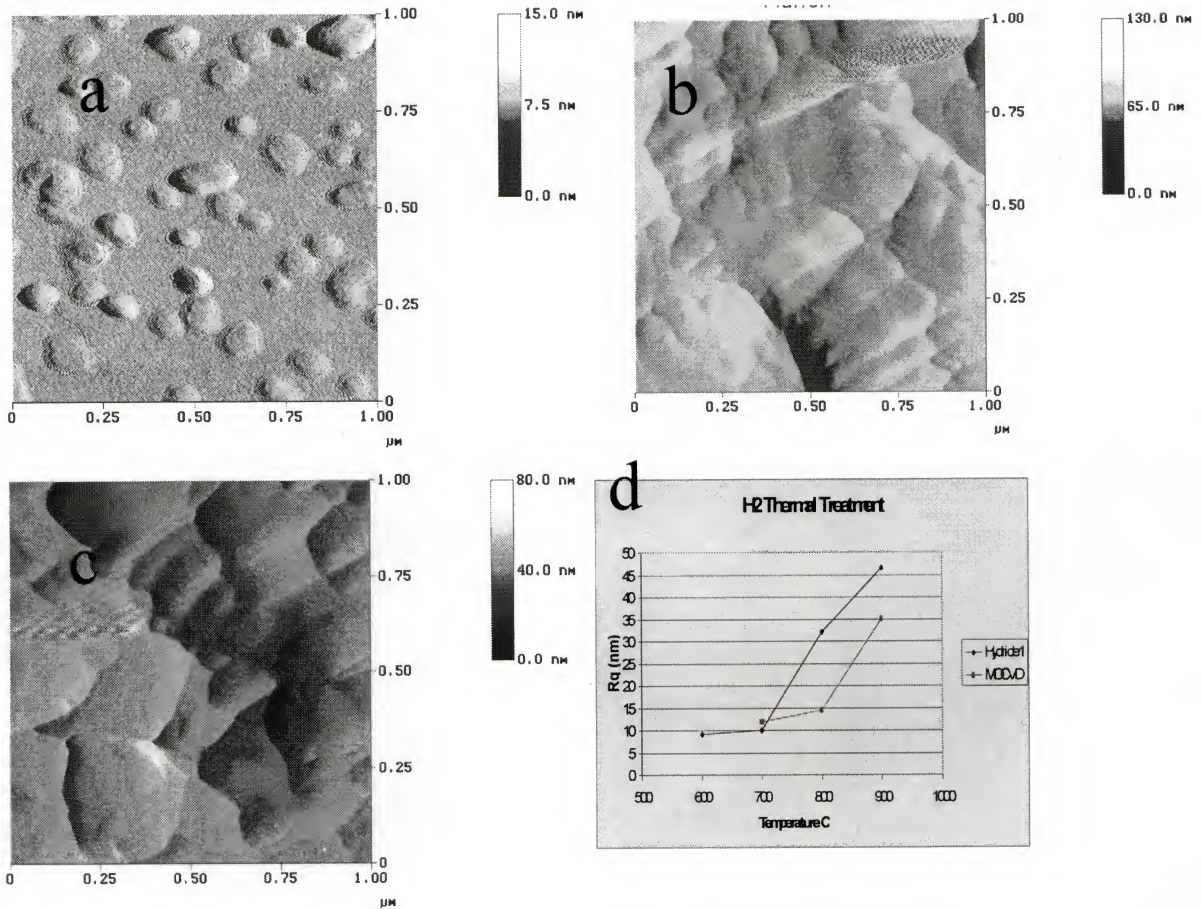
Figure 5-13. AFM of HVPE GaN annealed in H_2 a) 700 ^{0}C b) 800 ^{0}C c) 900 ^{0}C d) AFM RMS roughness as a function of anneal temperature for MOVPE and HVPE GaN

5.2.5 NH$_3$ Anneal of MOVPE GaN

Examination of films annealed in an NH3 ambient by SEM and AES show no decomposition of the MOVPE GaN film and only minimal sublimation. There is no significant change in roughness with anneal temperature for either MOVPE or HVPE films (figure 5-15a).

109
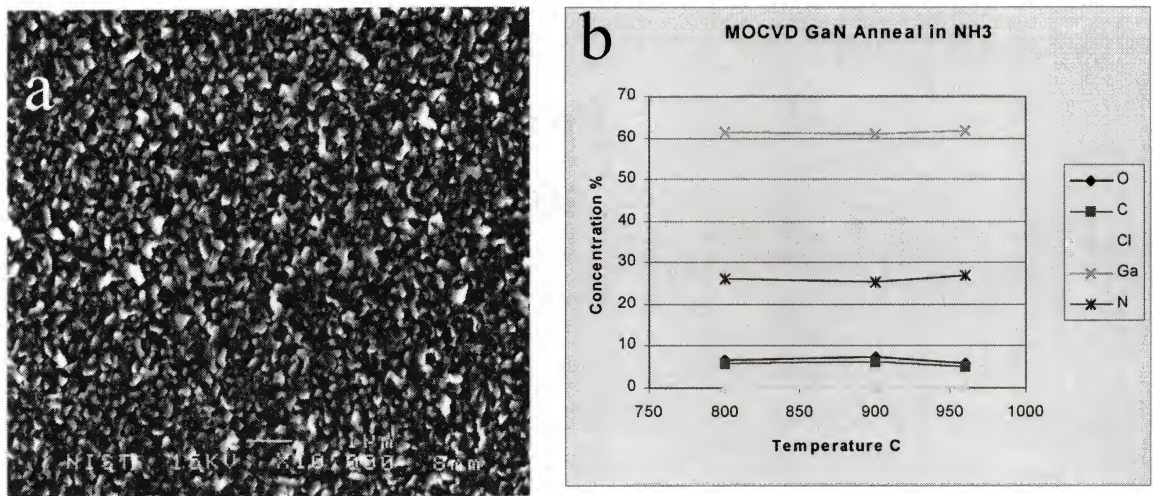
Figure 5-14. MOVPE GaN annealed in NH_3 a) SEM of sample annealed at 965 ^{0}C b) AES measurement of the surface concentration of O, C, Cl, Ga, and N atoms
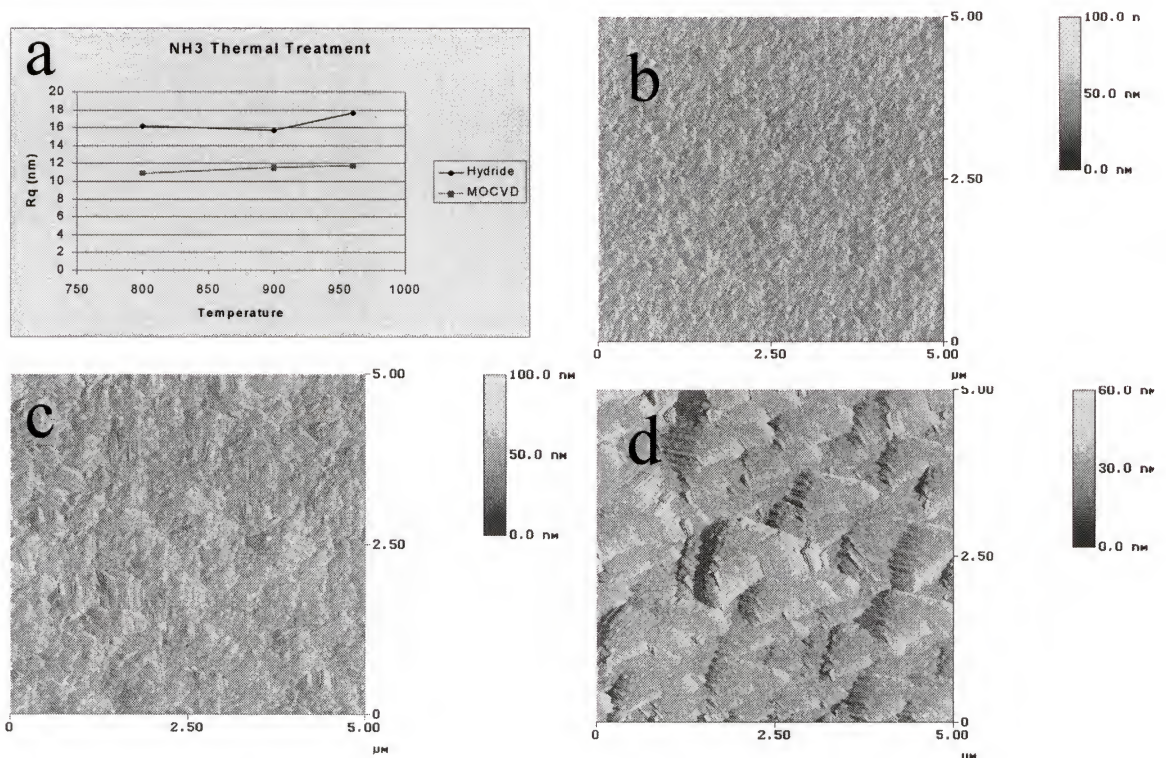
Figure 5-15. AFM of GaN annealed in NH_3 a) RMS roughness as a function of temperature for MOVPE and HVPE; micrographs of MOVPE film annealed at b) 800 ^{o}C c) 900 ^{o}C d) 965 ^{o}C

5.2.6 NH₃ Anneal of HVPE GaN

From the AFM pictures in figure 5-16 for HVPE GaN annealed in NH_3 a slight surface smoothing caused by a mild etching mechanism is observed. It is postulated that H decomposes from NH_3 to attack the energetically unstable island structures on the surface of the GaN.

In a competing process, active nitrogen species from ammonia gas would shift the decomposition reaction: $GaN^s = Ga^l + \frac{1}{2} N_2^v$ to the left, thus inhibiting gallium nitride from decomposing. Therefore, at the above conditions the reaction of both MOVPE and HVPE GaN with ammonia is insignificant and is hindered by the kinetic stability of NH_3 species. No composition change by AES analysis of MOVPE films is observed. Overall, both MOVPE and HVPE films are relatively stable in NH_3 ambient in the temperature range 500 to 965 °C (figure 5-15a).
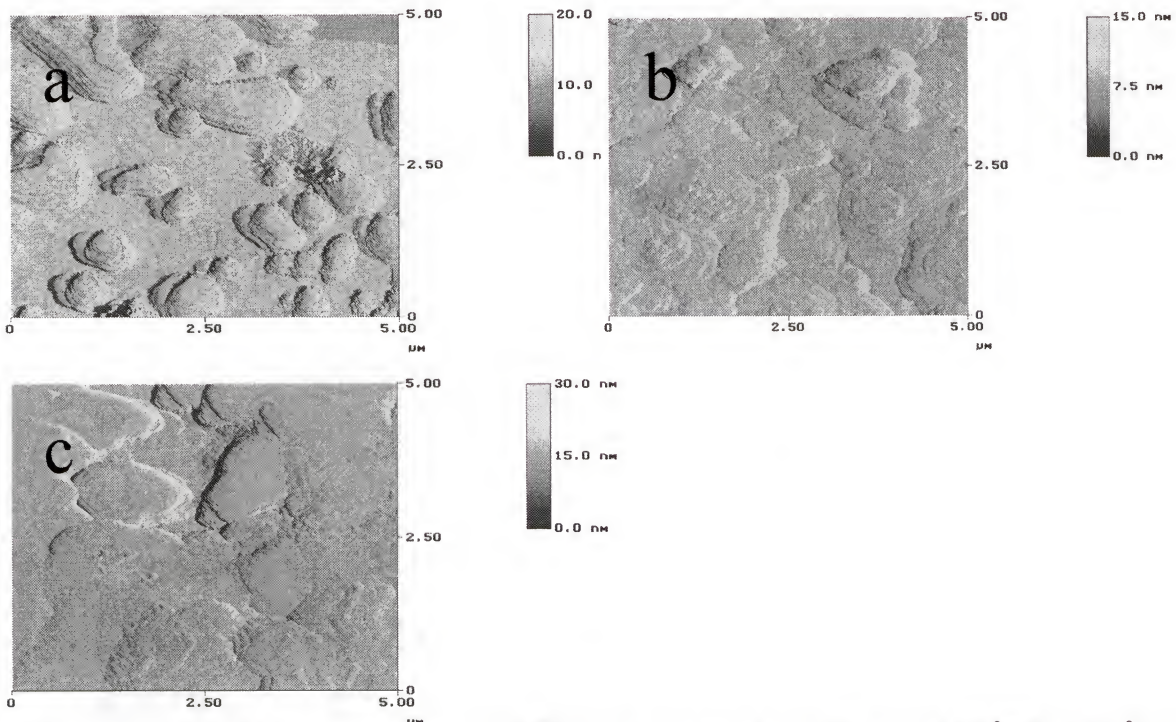
Figure 5-16. AFM micrographs of HVPE GaN annealed in NH_3 at a) 800 °C b) 900 °C c) 960 °C

5.2.7 N₂ Anneal of MOVPE and HVPE GaN

MOVPE GaN films are very stable during a N_2 anneal as the AFM picture (figure 5-17) shows. It was necessary to apply an extremely high anneal temperature to observe any surface degradation for both MOVPE and HVPE GaN. HVPE films did not decompose until 1200 °C and MOVPE films were completely stable in the range studied (up to 1400 °C). Even at high temperature, minimal dependence on anneal pressure (760 to 76 Torr) was seen in the evaporation rate.
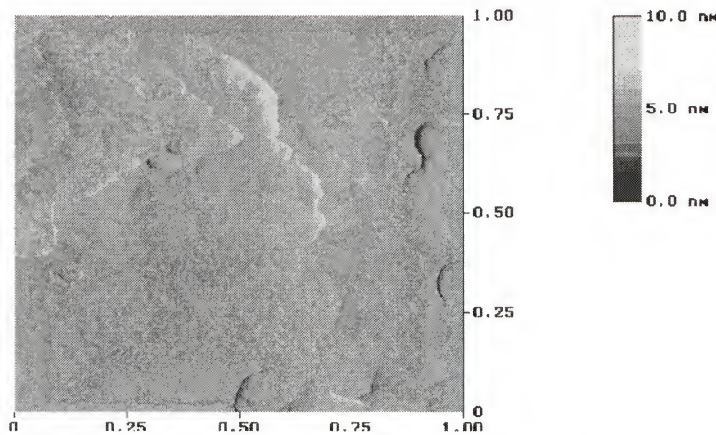
Figure 5-17. AFM micrograph of MOVPE GaN annealed in N_2 at 950 °C, 76 Torr

5.2.8 Catalytic Effect

GaN was shown to be very stable in nitrogen gas [141]. By using a catalyst such as a droplet of the $In_{.15}Ga_{.85}$ alloy ($T_{eutectic}$ = 86 °C), however, the decomposition temperature in N_2 was lowered to 850 °C for HVPE films and 1000 °C for MOVPE films. As seen in figure 5-18b, a $In_{.15}Ga_{.85}$ droplet on the surface decreases the decomposition temperature by 350 C° for MOVPE.

The catalytic effect observed for Ga and $In_{.15}Ga_{.85}$ droplets during the decomposition of GaN was also verified by weight loss. The evaporation is enhanced

through a catalytic effect by simultaneous condensation of the low-volatility product at the reactant/product interface [145-147]. At the surface, some of the condensation energy is transferred to the reactant thus increasing its decomposition rate [148]. For the decomposition of GaN, the enthalpy of reaction is reduced from 629.3 to 488.0 kJ/mol [149]. At the GaN^s/Ga^l interface, the decomposition of GaN should occur with the simultaneous condensation of Ga vapor lowering the initial temperature of GaN decomposition [149].

5.3 Summary of Thermal Stability

This work represents a study of GaN annealed in HCl, H_2, NH_3 and N_2. The GaN thermal behavior was evaluated by comparison of MOVPE and HVPE samples. A summary of the results is presented in table 5-3. In general, the MOVPE films were found to obey a dissociative sublimation mechanism while the HVPE films followed a decomposition pathway with liquid gallium droplet formation.

The MOVPE films appear to have a higher kinetic barrier towards decomposition. This difference cannot be accounted for by contaminants as a SIMS profile showed negligible chlorine and oxygen impurity concentrations in both films. The different growth mechanism, and resulting crystal quality and structure account for the observed difference.

5.4 Polarity

A review of the influence of polarity on GaN growth and processing is provided in chapter 1. Following this, the previous analysis of the thermal stability of GaN is extended to include how polarity affects the surface chemistry of GaN during growth and annealing of MOVPE and HVPE films.

Table 5-3. GaN thermal behavior comparison of MOVPE and HVPE samples

Annealing Gas	Growth Technique	Mechanism	Evaporation Temperature (^{o}C)	Comment
HCl	MOVPE	Sublimation	800	Slight Etching Above 800 ^{o}C
	HVPE	Decomposition	800	Etching Above 900 ^{o}C
H$_2$	MOVPE	Sublimation	800	Completely Sublimed by 900 ^{o}C
	HVPE	Decomposition	800	~100 μm Droplets at 900 ^{o}C
NH$_3$	MOVPE	Sublimation	Small Effect at 965	Roughens Above 800 ^{o}C
	HVPE	Decomposition	Small Effect at 965	Smooths Above 800 ^{o}C
N$_2$	MOVPE	Negligible	Completely Stable to 1400	From 40 to 760 Torr
	HVPE	Decomposition	1200	Negligible Pressure Influence

Influence of Polarity on Results. What follows is a discussion of the results that clarifies the role of polarity on GaN growth and surface properties. As discussed prior (chapter 1), Weyher *et al.* revealed that when exposed to aqueous solutions of KOH and NaOH, the rough MOVPE films with N-face hexagonal crystallites etched more rapidly than did the smooth Ga-faced films [110,111]. Using a similar methodology it was found that a wet etch of KOH rapidly etched the rough HVPE GaN surface (fig 5-19a), and in fact etched the surface into hexagonal facets. A similar result was seen with HCl gas anneals (figure 5-5). In some cases, however, the rough GaN seemed to planarize upon annealing (a result of H dissociating from NH$_3$ gas and attacking the energetic hillocks).

Our smooth films (MOVPE) etched slower (figure 5-19b) and did not preferentially etch any of the faces of GaN. Using prior notation our rough HVPE films were clearly N-face, while our MOVPE films were Ga-face. For our MOVPE GaN films

on sapphire, low-temperature AlN buffer layers were not needed to produce Ga-face GaN. Instead a pre-nitridation step was used to convert the sapphire surface to the correct orientation. Prior to MOVPE growth, the in-situ pre-nitridation step involves flowing H_2 and NH_3 gas that at growth temperature provides a reducing atmosphere that strips the native oxide from the surface and strips surface oxygen from the bulk substrate. Now nitrogen from the NH_3 is able to bond with aluminum at the surface of the substrate. The nitrogen proceeds to diffuse into the substrate surface forming a pseudo AlN buffer-layer. The polarity of the surface is realigned to provide favorable nucleation sites for Ga-face GaN growth. Comparatively, HVPE adds chlorine gas to the reaction chemistry. Although a pre-nitridation step was used for HVPE, the chlorine molecule destabilized the structure and thus the polarity of the surface. Without properly oriented nucleation sites available at the surface, HVPE by its nature proceeds in a three-dimensional, N-face growth regime.
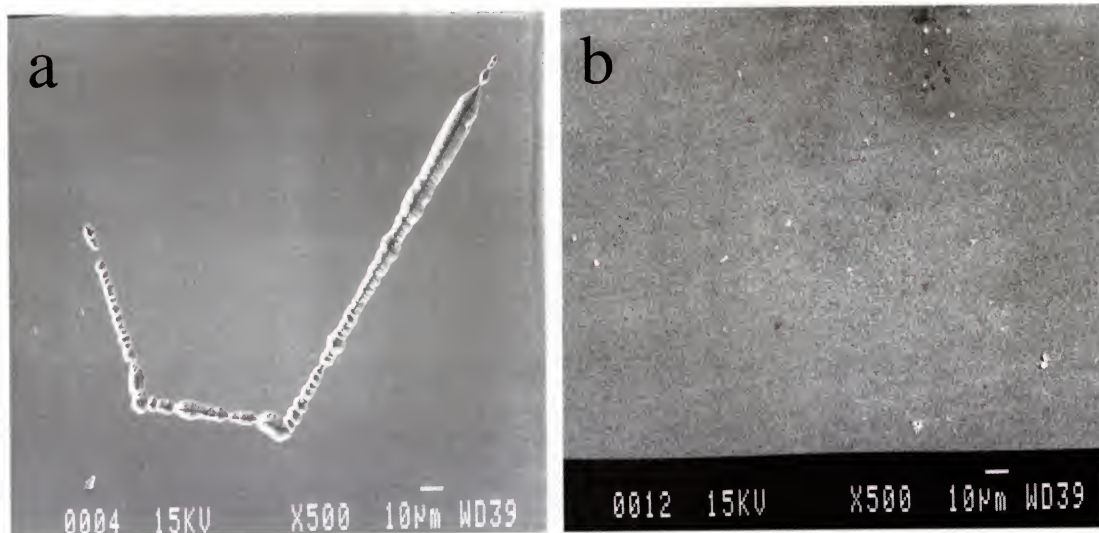
Figure 5-19 SEM micrographs of GaN wet etched in KOH a) HVPE b) MOVPE

In understanding why the HVPE films were rougher, several related phenomena are easily tied together. HVPE GaN films have a high growth rate and N-face polarity. Thus we determined that crystal structure depends not only on growth technique but also on initial substrate surface polarity. The N-face films are known to have pyramidal growth versus Ga-face films that have a slower layer-by-layer growth mechanism. The N-face films are structurally less stable with energetic pyramidal faces that would be highly susceptible to etching. As observed in this study the N-face films etch quickly and etch into hexagonal pyramids. This also relates to reports that the less stable N-face GaN surface oxidizes rapidly due to the energetic nature of its surface [109].

Raman measurements. Raman analysis was performed to provide confirmation of the polarity of the MOVPE and HVPE films assigned in this study.

In hexagonal GaN, excitation close to resonance with scattering by LO phonos by the Frohlich-mechanism can give rise to the higher order LO phonon [150]. This scattering can be seen as $A_1(LO)$ or $E_1(LO)$ excitation. The LO phonon scattering is proportional to the square of the polaron coupling constant. Thus the LO phonon is related to the polarity of the anion-cation bond. This scattering is more pronounced in GaN than traditional III-V semiconductors due to the strength of the Ga-N bond [150]. The direction of this polarity can be determined by linking peak shifts to the phonon dispersion relationship for the planar bond-charge model [151]. When imposing a condition of static equilibrium, it was reported for III-V semiconductors that a cation(Ga)-polarity induces a LO shift to a higher optical frequency [151]. The $A_1(LO)$ phonon refers to a symmetric stretching of the longitudinal optical phonon.
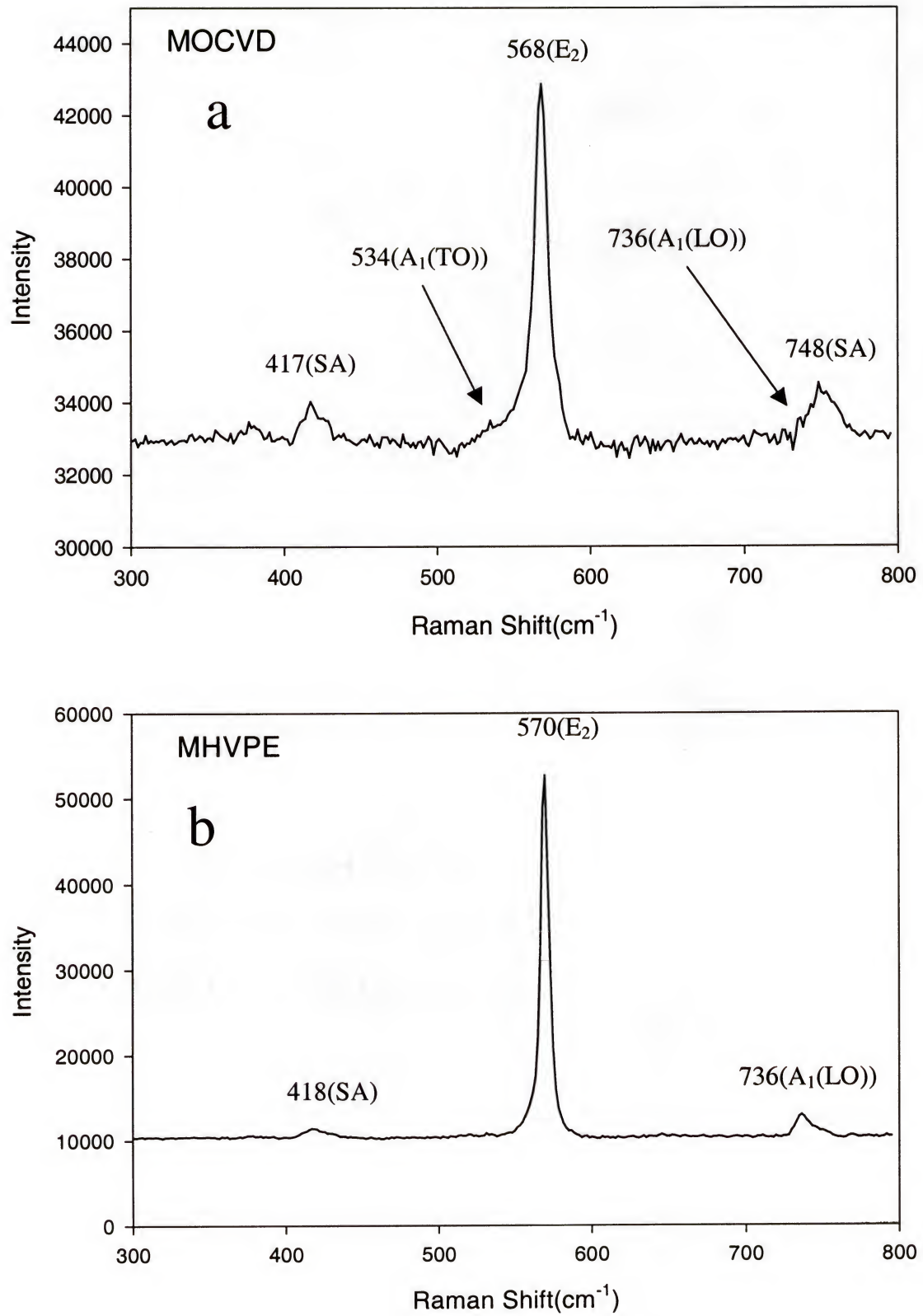
Figure 5-20. Raman spectra of GaN a) MOVPE b) HVPE

As observed in figure 5-20a, it appears that the $A_1(LO)$ phonon for MOVPE films either does not exist or has shifted to a higher frequency and is obscured by the SA phonon. When compared to the HVPE Raman spectrum (figure 5-20b) this would indicate that the MOVPE film is Ga-face while the HVPE film is N-face.

5.5 Conclusions

Using our annealing study we were able to inspect the GaN surface by AFM, AES, SEM, and EDS. This correlated with our thermodynamic analysis to indicate which mechanism the GaN films would follow when exposed to elevated temperatures. Specifically this work elegantly explains the structure and composition of the GaN surface, as well as how the surface science and kinetic barriers of GaN relate to GaN polarity.

To gain more information from this annealing study, simple electrical tests such as Hall and I-V curve measurement could be made on the samples to gain information on mobility and breakdown voltage, respectively. Although it is expected that they would follow the basic trend of a rapid destruction of the semiconductor structure and properties above a certain temperature dependent on the anneal ambient and growth technique. It would be of scientific and practical interest to anneal $AlGaN/Al_2O_3$ and GaN/Si samples to see if these films have the same temperature stability points and vaporization mechanisms as the films studied in this chapter.

Additional confirmation of the polarity determination is under way with TEM (University of Central Florida) and X-ray standing wave (Cornell High Energy Synchrotron Source) but results were not available as of this writing.

CHAPTER 6
THEORETICAL VAPORIZATION OF GALLIUM NITRIDE

6.1 Introduction

Along the [0001] direction, gallium nitride crystals have alternating layers of gallium and nitrogen atoms. The (0001) and the (000-1) faces are composed of primarily one type of atom and have been shown to have different surface structure, etching, oxygen adsorption behaviors, and crystal growth rates [96]. The [0001] face is designated as the Ga-face and the [000-1] face will be referred to as the N-face. Based on previous results it was shown that MOCVD GaN grew along the [0001] direction and sublimed congruently when exposed to elevated temperature. Conversely the HVPE films grew along the [000-1] direction and followed a decomposition mechanism that included liquid gallium droplet formation.

6.2 Sublimation of MOCVD GaN

Hertz Langmuir Equation. The maximum rate of vaporization can be estimated from the standard Gibbs energy of formation for the compound [152]. It was found that MOCVD GaN dissociates readily at high temperature according to the reaction

$$2GaN^s = 2Ga^v + N_2^v \tag{6.1}$$

GaN sublimes congruently, that is the chemical composition of the GaN solid phase does not change over time. At equilibrium the Gibbs energy change of reaction 6.1 is zero

$$\Delta G = 0 = \Delta G^o + RT \ln K \tag{6.2}$$

where K is the equilibrium constant and accounts for the species that are not at their standard state condition. For the reaction 6.1 the equilibrium constant is given by

$$K = a_{Ga}^2 a_{N2} / a_{GaN}^2 \tag{6.3}$$

where the activity $= a_i = f_i/f_i^o$. Taking the standard state of GaN as the pure compound at the T and P of interest, then $a_{GaN} = 1$. Further assuming the gas is an ideal gas mixture, the $a_i = P_i$. With this assumption the, equilibrium constant reduces to

$$K_{GaN} = (p_{Ga})^2(p_N) \tag{6.4}$$

where (p_{Ga}) and (p_N) is the thermodynamic partial pressure of Ga and N_2, respectively.

At equilibrium then equation 6.2 becomes

$$\Delta G^o = -RT \ln K = -RT \ln[(p_{eq}^{Ga})^2 (p_{eq}^N)] \tag{6.5}$$

Assuming congruent sublimation at steady state, the flux, J_{Ga}, leaving the GaN film must equal

$$J_{GaN} = J_{Ga} = 2J_N \tag{6.6}$$

The maximum rate of vaporization is given by the Hertz-Langmuir equation

$$J_{GaN} = (p_{eq}^{GaN}) / [2\pi MRT]^{1/2} \tag{6.7}$$

where $[2\pi MRT]^{1/2}$ is the transitional velocity [152].

Substituting and rearranging yields

$$J_{GaN}(max) = [(2/M_{Ga}M_{N2})^{1/2}\exp(-\Delta G^o/RT)]^{2/3} [2\pi RT]^{-1/2} \tag{6.8}$$

Substituting $M_{Ga} = 69.72$ g/mol, $M_{N2} = 28.0$ g/mol, T = 800 ^{o}C = 1073 K, R = 8.314 J/mol-K, and $\Delta G^o = 55$ KJ/mol [152] allows the maximum rate of evaporation of GaN into a vacuum at 800 ^{o}C to be determined as

$$J_{GaN} = 1.08 \times 10^{-6} \text{ kg/m}^2\text{s} = 1.08 \times 10^{-7} \text{ g/cm}^2\text{s} \tag{6.9}$$

For a 1-μm film on 1x1cm sample the total weight of GaN is 6.1 x 10^{-4} g. With the relation, $\Delta m = JAt$, figure 6-1 below presents the film weight loss for the experimentally estimated rate and the maximum theoretical evaporation predicted by the Hertz-Langmuir equation versus temperature. No sublimation was observed in the experimental samples at 700 ^{o}C, however, the Hertz Langmuir equation predicts vaporization at 700 ^{o}C.
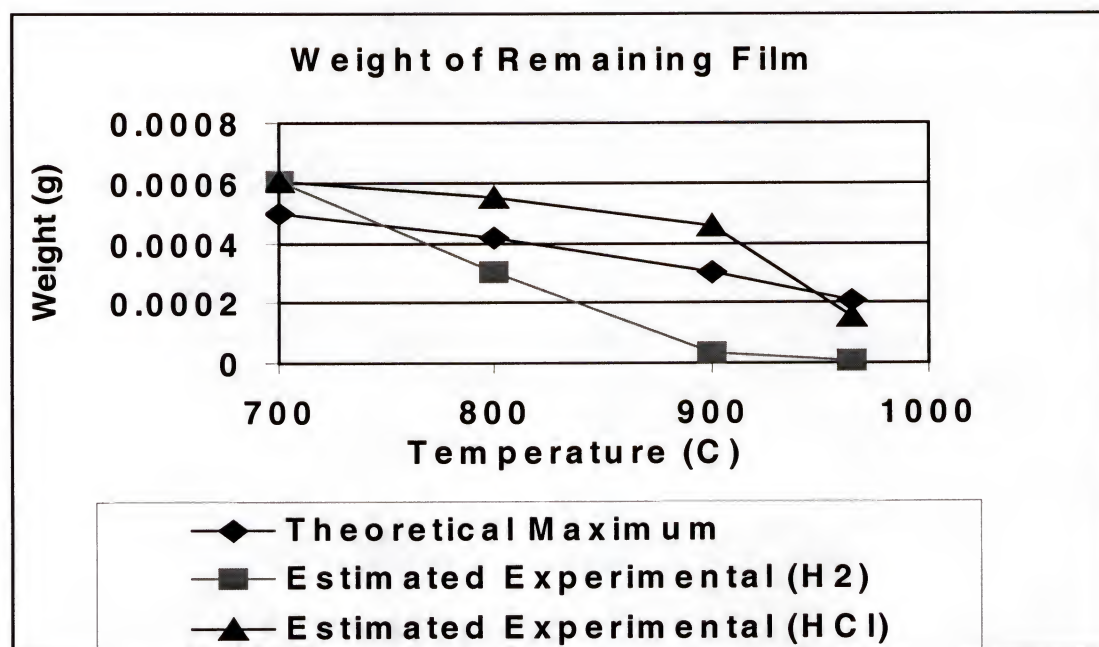
Figure 6-1. Experimental and theoretical weight loss from MOCVD GaN film

6.3 Decomposition of HVPE GaN

6.3.1 Chemistry of Decomposition

The investigation of HVPE gallium nitride vaporization indicates the primary mechanism is decomposition to Ga^l and N_2^v. Since gallium liquid droplets were readily discernible after vaporization, it was concluded that gallium nitride vaporizes incongruently to give liquid gallium and nitrogen vapor molecules. Incongruent

vaporization occurs when the composition of the vapor is different than the crystal composition.

$$GaN^s \rightarrow Ga^l + N_2^v \tag{6.10}$$

Two alternate routes are available to calculate the decomposition rate of GaN. The first described in sections 6.3.2 to 6.3.5 estimates the amount of gallium on the surface and then assumes a stoichiometric amount of nitrogen has left the surface as N_2. The second route described in section 6.3.7 calculates the rate nitrogen escapes the surface by diffusing through liquid gallium and then assumes an equal amount of gallium is added to the liquid phase. Section 6.3.6 confirms the rate of gallium liquid evaporation is negligible.

Defects on the surface of the sample seem to serve as nucleation sites for vaporization. Untreated (without liquid Ga) samples showed an autocatalytic effect, that is the rate process increases with time. As the gallium droplets grow on the surface the rates of vaporization increases [153]. A similar catalytic decomposition mechanism was seen when the sample was placed in the reactor chamber with excess liquid gallium placed on top of the evaporating surface.

Examining the structure of GaN indicates the reasons for the low vaporization coefficient and catalytic activity by liquid gallium or indium. GaN is a hexagonal close-packed arrangement of gallium atoms with nitrogen atoms in the tetrahedral positions. This rigid wurtzite lattice has covalent bonds between each nitrogen atom and its four nearest gallium neighbors. Strong covalent bonds must be broken and nitrogen atoms must diffuse over the crystal surface in order for vaporization to occur directly from the solid [153]. An alternate pathway with lower activation energy may be provided when a

surface liquid is used to dissolve the GaN, acting as a catalyst. The liquid disrupts the rigid crystal structure during the solution process. The nitrogen atoms are then free to migrate into the liquid to form N_2 molecules that can diffuse through the liquid and escape to the liquid-gas interface where vaporization occurs [154]. This nitrogen vaporization rate may decrease over time due to depletion of the sample or increase in the thickness of the surface layer of gallium.

A complex series of reaction steps are involved in vaporization of solids [154]. Bond breaking, bulk diffusion, charge transfer, rearrangement, transport of atoms along the surface, or association or dissociation of the vaporizing surface atoms. Any of the mechanisms can be the controlling step for the kinetics of vaporization of a compound semiconductor.

For other III-V semiconductors the presence of liquid metals was shown to increase the vaporization rate without changing the activation energy [154]. The catalytic effect may be attributed to one of the following: the liquid metal provides electrons at the surface that facilitate charge transfer during vaporization; the liquid metal dissolves the vaporizing species and provides an alternate pathway for evaporation; the liquid metal changes the defect concentration at the surface. Since we observed that droplets form at defects on bare samples, perhaps the later mechanism shows the relation for catalytic vaporization. When charge transfer is the limiting mechanism as for the case of CdS, the activation energy is on the order of the bandgap energy [155].

Conceivably liquid metals on the GaN crystal lattice change the defect concentration at the surface, thus influencing the evaporation rate. The gallium atoms

precipitate out in the form of a liquid at the surface due to their low vapor pressure while the nitrogen atoms associate and subsequently diffuse through the liquid metal.

Vaporization catalysis occurs when the liquid layer that forms actually enhances the vaporization rate [156]. This enhancement is with respect to the initial sublimation rate for the crystal, which has not built up a liquid surface layer. Once the liquid layer forms or is placed on the surface intentionally the steady-state vaporization coefficient is much closer to unity than the initial value. Schoonmaker [157] found that the decomposition of pure GaN in nitrogen ambient was too small to measure, however when liquid gallium or indium was placed on the surface the rate was equivalent to a Langmuir vapor pressure of $N_2(g)$ of 10^{-6} atm at 800 ^{o}C [152]. The Langmuir vapor pressure, P_L, is an apparent vapor pressure where

$$P_L = \alpha_v{}^o P_E \tag{6.11}$$

and P_E is this equilibrium vapor pressure and α_v is the vaporization coefficient.

Indium and gallium liquid metals appear to dissolve GaN, acting as an effective catalyst. It is likely that other liquid metals could follow the same catalytic mechanism. The requirement is that the phase diagram has a simple eutectic with limited solubility of GaN in the liquid metal. GaN has a limited solubility in liquid indium resulting in the liquid metal acting as a catalyst. Grzegory *et al.* [158] calculated the liquidus line for Ga-GaN system using an ideal solution approximation and a melting temperature of 2790 K. They found that for an ideal solution, the solubility can be expressed as:

$$n = n_0 \exp(\Delta H_{sol}/kT) \tag{6.12}$$

where H_{sol} is the heat of dissolution of $GaN^s = Ga^l + N^l$. For GaN, $H_{sol} = 187.02$ kcal/mole = 0.49 eV/bond and expresses the bonding energy in the crystal in relation to its solution.

The present work was initiated to investigate both the thermodynamic and kinetic aspects of the vaporization of GaN.

6.3.2 Surface Thermodynamics

A detailed discussion on the surface tension of liquid droplets is presented to aid in the description of liquid gallium droplet formation in these experiments. For any interface (e.g., v-l, l-l, v-s, etc.), the Gibbs energy of formation of that interface is positive for stable existence between two phases. Were it zero or negative then any fluctuation would expand the surface continuously and lead to eventual complete dispersion of one material into the other.

The surface tension, γ, is a definite property of the interface between two phases [159]. If two phases are in contact with each other and one is moved over the surface by dA, then the work required to do this is γdA. This is reversible work at constant temperature and pressure, and thus gives an increase in the free energy of the system.

$$dG = \gamma dA \tag{6.13}$$

This process is reversible, therefore the heat correlated with it gives the surface entropy

$$dq = TdS = TS^s dA \tag{6.14}$$

Here S^s is the surface entropy per area of the surface. As $(\partial G/\partial T)_P = -S^s$, then

$$d\gamma/dT = -S^s \tag{6.15}$$

The total surface enthalpy per area, H^s, is

$$H^s = G^s + TS^s \tag{6.16}$$

Typically total surface enthalpy is equal to the total surface energy E^s

$$E^s = G^s + TS^s \qquad (6.17)$$

or a form derived by Guggenheim [160] is

$$E^s = \gamma - T d\gamma/dT \qquad (6.18)$$

The surface tension of most substances decreases with increasing temperature in a nearly linear fashion.

6.3.3 Thermodynamic Properties of Curved Surfaces

Liquids assume a curved surface in equilibrium to minimize the surface area and thus decrease the excess surface Gibbs energy [161]. The radius of curvature depends on the surface tension, and a pressure difference is established, on the two sides of the interface. In equilibrium, the radius of curvature, r, of a droplet is related to the internal and external pressures, P_{in} and P_{ex}, respectively, and with the surface tension by

$$P_{in} - P_{ex} = 2\gamma/r \qquad (6.19)$$

Therefore, for a flat surface as r -> ∞, the pressure difference normal to the interface disappears. Conversely, the smaller the droplet size is (or the larger the surface tension) then the larger the pressure difference.

From thermodynamics, the effect of a change in mechanical pressure at constant temperature on the molar free energy of a substance is

$$\Delta G = \int V dP \qquad (6.20)$$

or if the molar volume V is considered to be constant for a condensed phase for small changes in pressure. For constant γ, $\Delta P = \gamma(1/R_1 + 1/R_2)$ which indicates the change in pressure for a change in radius, then

$$\Delta G = \gamma V(1/R_1 + 1/R_2) \qquad (6.21)$$

Assuming the vapor to be a ideal gas, then $G = G^o + RT \ln P$. For a spherical particle, the vapor pressure of a droplet is expressed by the Kelvin equation,

$$\ln(P/P_o) = 2\gamma V_m/RTr \qquad (6.22)$$

V_m is the molar volume of the drop and P_o is the vapor pressure over a flat surface where $1/r$ equals zero. Hence small particles have higher vapor pressure than larger ones. Similarly for solubility that is proportional to vapor pressure for ideal solutions, small droplets have greater solubility than larger particles.

Generally, solids and liquids that have large surface tensions also have strong adhesion bonds. Values for hydrogen and nitrogen gas are known to be [159]

$\gamma_v (H_2) = 2.01$ dyne/cm

$\gamma_v (N_2) = 9.41$ dyne/cm

The surface tension of pure solid GaN can be estimated from theory [161], as the surface tension of a solid can be estimated from the bond strength at 0 K of surface atoms. Calculating one-half the energy to rupture all the bonds passing through one cm^2 of the surface.

$$E_s = \frac{1}{2} E_{cohesion} \qquad (6.22)$$

The basal plane bond length of hexagonal GaN is $a = 0.318$ nm, giving 1.86×10^{15} bonds/cm^2 with a density of 6.1 g/cc. A bond strength of 8.7 eV/atom results in a surface tension, γ_s(GaN), of 127 dyne/cm [161]. This model neglects reconstruction of the surface bonds.

Bikerman reported a surface tension for liquid gallium in the presence of its own vapor, γ_l (Ga, 30 ^{o}C), of 706 dyne/cm [162]. As discussed, van der Waals interactions cause the surface tension, γ, to decrease with increasing temperature. One relation

presented by Bikerman [162] states $\gamma = E_s (1- T/T_c)^n$ where n is approximately unity for most substances. T_c is the critical temperature (T_c (Ga) = 7125 K). If the variation in density and thus the molar volume is small then $\gamma = E^s$, particularly for low to moderate temperatures. Extrapolating for liquid gallium, E_s = total surface energy = $\gamma_0 = \gamma(0\ K) = 736$ dyne/cm. An appreciable decrease is seen in surface tension. At 965 ^{o}C the surface tension of liquid gallium decreases to 608 dyne/cm.

Table 6-1. Surface tension of liquid gallium

Temperature (^{o}C)	γ_l (Ga)
800	625.2
900	614.8
965	608.1

Interfacial tension between two phases. Any two-phase interaction (γ_{ab}) can be estimated from the individual surface tensions (γ_a, γ_b). This approximation allows an estimation of surface tension by combining the van der Waals force contribution from two separate pure substances. For constant T and P, a small change in surface free energy is given by [159]

$$dG = (\Delta G/\Delta A_a)dA_a +\ (\Delta G/\Delta A_{ab})dA_{ab} + (\Delta G/\Delta A_b)dA_b \tag{6.23}$$

where

$$(\Delta G/\Delta A_a) = \gamma_a,\ \ (\Delta G/\Delta A_b) = \gamma_b \tag{6.24}$$

$$(\Delta G/\Delta A_{ab}) = \gamma_{ab} \tag{6.25}$$
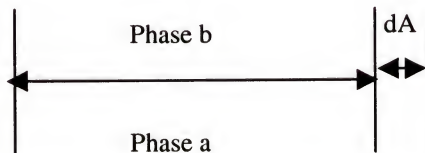
Figure 6-2. Interfacial tension between two phases, a and b, at constant T, P

A simplified form uses the geometric mean law to give [162]

$$\gamma_{ab} = \gamma_a + \gamma_b - 2\beta (\gamma_a \gamma_b)^{1/2} \tag{6.26}$$

β is related to molar volumes, empirically it ranges from 0.5 to 1.5 and for most substances it can be approximated to unity. Thus

$$\gamma_{ab} = \gamma_a + \gamma_b - 2(\gamma_a \gamma_b)^{1/2} \tag{6.27}$$

Table 6-2. Surface tension interaction between GaN^s, Ga^l and H_2^v

Temperature (^oC)	γ_l (Ga) (dyne/cm)	γ_{sl} (GaN^s-Ga^l) (dyne/cm)	γ_{lv} (Ga^l-Ga^v) (dyne/cm)	γ_{sv} (GaN^s-Ga^v) (dyne/cm)
800	625.1	470.3	591.7	113.0
900	614.8	462.3	581.6	113.0
965	608.1	457.2	575.1	113.0

6.3.4 Contact Angle

Force balance on the surface tensions for a slight movement in the s-l-v boundary while the γ_{ij} values remain constant gives

$$\Delta G_s = \Delta A(\gamma_{sl} - \gamma_{sv}) + \Delta A \gamma_{lv} \cos(\theta - \Delta\theta) \tag{6.28}$$
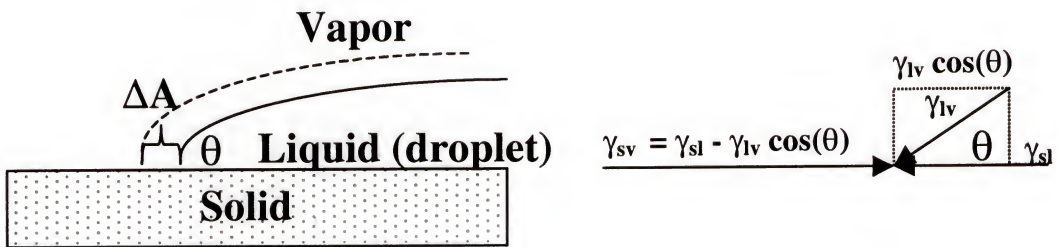
Figure 6-3. Force balance at solid-liquid-gas interface

where γ_{sv} is the interfacial tension at the solid–gas interface, γ_{sl} is the interfacial tension at the solid-liquid interface, γ_{lv} is the interfacial tension at the liquid–gas interface. Surface tension exerts a pressure tangentially along a surface (figure 6-3). The surface Gibbs

energy balance is between the surface forces acting in opposite directions at the point where the three phases of solid, liquid and gas meet [161]. Equilibrium occurs when the limit $\Delta G_s/\Delta A = 0$ as $\Delta A \to 0$ reduces the previous equation to

$$(\gamma_{sl} - \gamma_{sv}) + \gamma_{lv}\cos(\theta) = 0 \quad \text{or} \quad \gamma_{lv}\cos(\theta) = \gamma_{sv} - \gamma_{sl} \tag{6.29}$$

Now knowing the surface tensions, one can compute the contact angle. As the contact angle θ advances towards zero, complete wetting of the surface occurs [159]. If the contact angle is large (θ approaching 90°), the liquid does not freely wet the solid surface. Rearranging equation 6.29 gives

$$\gamma_{sv} = \gamma_{sl} + \gamma_{lv} \cos(\theta) \tag{6.30}$$

θ is the contact angle at the solid-liquid–gas interface with its value listed in table 6-3.

Table 6-3. Contact angle at solid-liquid-gas interface

Temperature ($^{\circ}$C)	θ
800	21.33
900	18.65
965	16.62

6.3.5 Radius of Curvature

A geometric manipulation is needed to calculate the radius of curvature. This model assumes that the force of gravitry is insignificant compared to surface tension forces. For any line that contacts the surface at one point, this line will be perpendicular with another line emanating from the center of the same circle (figure 6-4). θ is the angle the droplet makes with the surface. Φ is the internal angle and is related to θ by

$$\Phi = 90 - \theta \tag{6.31}$$
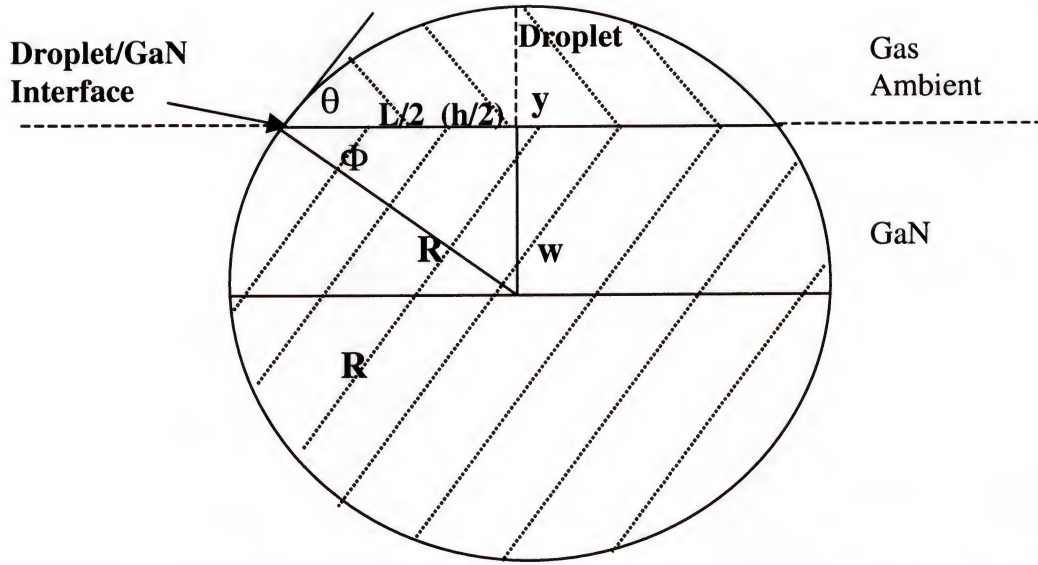
Figure 6-4. Geometric representation of a droplet with visualized radius of curvature.

The length of the droplet was measured experimentally (equation 6.31 and table 6-3) and Φ was calculated, allowing the radius of curvature, R, to be calculated by

$$\cos \Phi = (L/2) / R \tag{6.32}$$

And w is given by

$$\tan \Phi = w / (L/2) \tag{6.33}$$

Integration is necessary to calculate the volume of the droplet. To find an arbitrary y and h,

$$R^2 = h^2 + y^2 \text{ or } h = (R^2 - y^2)^{1/2} \tag{6.34}$$

The volume of the droplet is calculated from w to R,

$$V = \int_w^R \pi h^2 dy = \pi \int_w^R (R^2 - y^2)dy \tag{6.35}$$

$$V = \pi[R^2 y - y^3/3] \big|_w^R \tag{6.36}$$

$$V = \pi [[(2/3)R^3] - [R^2 w - (1/3)w^3]]] \tag{6.37}$$

Table 6-4. Geometric properties of droplets

Temperature (°C)	L(exp) (μm)	Φ	R (μm)	w (μm)	Volume (cc)	Average thickness (μm)
800	0.10	68.67	0.14	0.09	7.23E-16	0.02
900	0.50	71.35	0.78	0.60	7.45E-14	0.09
965	10.00	73.38	17.45	14.30	5.13E-10	1.64

The average GaN film thickness (table 6-4) is the volume divided by the area. By using the volume of the liquid droplets along with a standard distribution of droplets, the total amount of liquid gallium formed can be calculated. Once the total mass of liquid gallium droplets is known, the total amount of solid GaN needed to produce this product is known. A 10 μm, 1cm x 1cm GaN film has a total mass of 6.1×10^{-3} g. It was observed experimentally at 965 °C that the entire film was decomposed. This compares to the calculated (table 6-5) decomposed GaN mass of 1.3×10^{-4} g at 965 °C. The cluster distribution factor is the average distance to the next droplet divided by the radius of the droplet.

Table 6-5. GaN decomposition rate

T (°C)	Droplet length [μm]	Cluster distribution factor	# of clusters/ cm^2	Ga Droplet mass(g)	Total GaN decomposed [g/cm^2]	Decomposition rate [g/cm^{2}s]
800	0.1	5	4.0E+08	1.7E-06	1.8E-06	9.8E-10
900	0.5	5	1.6E+07	7.0E-06	7.3E-06	4.0E-09
965	10.0	5	4.0E+04	1.2E-04	1.3E-04	7.0E-08

Table 6-5 provides an estimation of the total amount of GaN decomposed, the key goal of this derivation.

6.3.6 Heat of Evaporation and Droplet Size

This section provides an aside to estimate the amount of Ga lost from the droplet by evaporation ($Ga^l \rightarrow Ga^v$). It will be shown that this loss rate is negligibly small. It is necessary to see the influence of droplet size on the evaporation rate of liquid gallium. A

derivation of the evaporation from, a droplet at constant temperature, T, and radius, r, will illustrate the influence of droplet radius on the heat of evaporation [163]. As the liquid evaporates it is replaced by a second phase it is in contact with (solid or liquid). Under these restraints the system is constantly replenished with heat corresponding to equilibrium evaporation dQ = TdS.

The system is divariant, that is the variables T and r determine the equilibrium states during equilibrium evaporation while the molar entropy, S, will be constant. As dn moles pass from the vapor to the liquid phase, entropy S''n'' of the second phase will decrease by S''dn while that of the first phase increases by S'dn. The entropy of the surface remains constant since the area and state of surface are unchanged dS = (S' − S'')dn [164].

The change in the molar latent heat of evaporation is defined as Δh_e = T(S' − S''). As a function of T and pressure, P,

$$\delta\Delta h_e = T[\partial P'(\partial S'/\partial P') - \partial P''(\partial S''/\partial P''))] \qquad (6.38)$$

Using the Gibbs-Duhem equation,

$$(\partial S/\partial P)_T = (\partial V/\partial T)_P \qquad (6.39)$$

where V = molar volume. Substitution gives

$$\delta\Delta h_e = -T[(v''/(v'-v''))(\partial V'/\partial T)) - (v'/(v'-v''))(\partial V''/\partial T)]\delta(2\sigma/r) \qquad (6.40)$$

where σ = interfacial tension, which is a function of γ [164]. Assuming an ideal gas where V' = RT/P with $(\partial V'/\partial T)_{P'}$=R/P', gives

$$\delta\Delta h_e = -[v'' - T(\partial V''/\partial T)_{P''}]\delta(2\sigma/r) \qquad (6.41)$$

Thus $\delta\Delta h_e$ increases as r decreases. Integrating yields the absolute change in heat of evaporation from a free surface to a curved droplet with a radius, r,

$$\Delta h_e(r) - \Delta h_e(O) = -(2\sigma/r)[v'' - T(\partial V''/\partial T)_{P''}] = -(2\sigma/r)v'' \tag{6.42}$$

where $(\partial V''/\partial T)$ is assumed to be negligible for a condensed phase.

Table 6-6. Absolute change in the heat of evaporation for droplet size

Radius (μm)	Relative $\delta\Delta h_e$
∞	1
10	0.999994
1	0.99994
0.1	0.9994
0.01	0.994
0.001	0.94

Thus table 6-6 shows for a 1 nm droplet, a 6% decrease in the heat of evaporation is predicted. This change needs to be incorporated when the rates of droplet evaporation or reaction rates are evaluated. Table 6-7 below displays the enthalpy correction for gallium droplets observed on the HVPE films.

Table 6-7. Heat of evaporation correction for droplets observed on HVPE films

T ($^\circ$C)	R (μm)	Enthalpy correction
800	1.372632983	5.8×10^{-5}
900	7.803277449	1.9×10^{-5}
965	174.4814291	0

The mass of liquid gallium present on the decomposed films has already been calculated. It is necessary to calculate the mass loss of gallium from evaporation. An enthalpy of evaporation for $Ga^l \rightarrow Ga^v$ is 256KJ/mol [165]. Deriving an equation for theoretical maximum evaporation similar to the derivation presented for GaN (section 6.2), the max flux is

$$J_{Ga}(max) = [(2/M_{Ga})\exp(-\Delta G_v/RT)]/[2\pi RT]^{1/2} \tag{6.43}$$

Equation 6-43 shows that the vaporization rates from liquid gallium are negligible compared to the amount of GaN decomposed. Therefore, mass loss of liquid gallium by evaporation need not be considered important.

6.3.7 Steady State Diffusion

In this final section, the rate of nitrogen diffusion through the gallium droplets will be calculated. The average thickness of the gallium droplets were calculated earlier and tabulated in table 6-4. If this final side derivation is correct, then the rate of nitrogen diffusion should equal the rate of GaN vaporization calculated earlier (table 6-5).

The rate of evaporation is controlled by a steady-state diffusion through the surface film. From Fick's law, the mass flux, J [$gcm^{-2}s^{-1}$] is given by [159]

$$J = - D(dc/dx) = - D\Delta c/\Delta x \qquad (6.44)$$

where c expresses the concentration of the nitrogen [gcm^{-3}], dx denotes the thickness of the surface region.

It was assumed that the activation energy is low for the nitrogen atoms to break from the crystal structure and enter the liquid film. Also nitrogen at the surface of the liquid gallium droplet freely evaporate into the ambient. Thus diffusion through the gallium liquid film is the limiting step for nitrogen vaporization.

Diffusion coefficients for nitrogen in liquid metals have not been reported in the literature [166]. Several theories exist to approximate diffusion in liquids, however, liquids are distinguished by a combination of strong intermolecular forces combined with irregular chaotic arrangement of atoms [166]. The Stokes-Einstein equation is based on the assumption that the particles are hard spheres with a molar volume, V_a, that move at a uniform velocity in a continuum under the action of a constant force

$$D_{ab} = [K'T]/[uV_a]^{1/3} \tag{6.45}$$

where u is the viscosity and K' is a constant of proportionality. The Wilke and Chang [162] model gives a semi-empirical estimation for the diffusion coefficient,

$$D_{ab} = 1.17 \times 10^{-13} (a_b M_b)^{1/2} T/[V_a^{0.6} u] \tag{6.46}$$

where a_b is the association factor ($a_b = 1$ for simple liquids) and $M_b = 69.7$ g/mol.

At 800 °C,

$$D_{ab} = 1.17 \times 10^{-13} (69.7 \text{ g/mol})^{1/2} (1073 \text{ K})/[156 \text{cc/mol}^{0.6} 1.5 \text{cP}] \tag{6.47}$$

$$D_{ab} = 3.38 \times 10^{-11} \text{ cm}^2/\text{s} \tag{6.48}$$

The external concentration of nitrogen was calculated from data that Schoonmaker *et al.* [153] reported on the ambient nitrogen pressures of the GaN^s/Ga^l system. The internal concentration was calculated assuming the solid-liquid interface was saturated according to the liquid gallium solubility equation of Grzegory *et al.* [158] described earlier in this chapter (equation 6.12) using a similar phase diagram to figure 1-6. It is assumed that nitrogen atoms are rapidly freed from the GaN lattice and allowed to enter the liquid to saturation at the GaN/Ga^l interface. From Fick's law we have at 800 °C,

$$J_{N2} = D_{N2Ga} (c_{in} - c_{ex}) / l_{droplet} \tag{6.49}$$

$$J_{N2} = (3.38 \times 10^{-11} \text{ cm}^2/\text{sec})(6.6 \times 10^{-10} - 1.1 \times 10^{-11} \text{ mol/cc}) / (2.3 \times 10^{-6} \text{ cm}) \tag{6.50}$$

$$J_{N2} = 6.8 \times 10^{-10} \text{ g/cm}^2\text{-s} \tag{6.51}$$

Table 6-8. Diffusivity constants and mass fluxes for nitrogen in liquid gallium

Temperature (°C)	D_{N2Ga} [cm²/s]	Average thickness [cm]	n_{in} [mol/cc]	n_{ex} [mol/cc]	J [g/cm²s]	Total GaN decomposed [g]
800	3.4E-11	2.3E-06	6.6E-07	1.1E-11	6.8E-10	7.2E-06
900	3.7E-11	9.5E-06	4.0E-06	2.2E-11	1.1E-09	1.1E-05
965	3.9E-11	1.6E-04	1.1E-05	2.8E-11	1.8E-10	1.9E-06

The total amount of GaN decomposed can be calculated from the total amount of nitrogen that diffuses out of the film. The total amount of GaN estimated to decompose

in this section (table 6-8) is lower than the semi-quantitative rates measured earlier in section 6.3.6 (table 6-5). Likely the diffusion coefficient for nitrogen gas in liquid gallium (D_{N2Ga}) that was estimated from theory was too low.

6.4 Conclusions

This chapter provides a theoretical description of the sublimation of MOCVD GaN and the decomposition of HVPE GaN. The results of this derivation show good agreement with experimental data from chapter five for MOCVD sublimation (figure 6-1) and HVPE decomposition (table 6-5).

Because many assumptions and approximations were made in all the calculations, some inherent error is present. For detailed estimations of rate parameters, torsion-effusion experiments, which precisely measures vapor pressure of solid- and liquid-phase sample, should be performed in the future to refine the models presented in this chapter.

Chapter 7

Conclusions and Recommendations for Future Work

7.1 LiGaO$_2$ and LiAlO$_2$ Substrates for GaN Epitaxy

The demonstration of free-standing GaN wafers of relatively large area (1 cm^2) and low dislocation density (10^7cm^{-2}) grown by a manufacturable process is significant. Future research should be pursued to produce GaN thick enough (>100 μm) for subsequent device processing. LAO due to its superior chemical stability appears to have more potential in the merged H-MOVPE system.

Several research issues need to be addressed. The most important issue is substrate scale-up, as growth to date has used only 1-cm^2 pieces. A 2-dimensional simulation of the reactor should be developed to assist in understanding the scale-up issues. Also, doping during growth with both n and more importantly p-type dopants may affect the process (e.g., LiGaO$_2$/GaN interfacial energy, residual stress). Of course, this should be proceeded by a study to reduce the background carrier concentration.

For certain device applications there is an advantage to having a larger bandgap (e.g., Al$_x$Ga$_{1-x}$N) or larger lattice constant (e.g., In$_x$Ga$_{1-x}$N) substrate. The stability differences between the chlorides of Ga and Al or In should be examined by the thermodynamic computation. Both AlGaN and InGaN growth should be investigated experimentally on LAO and LGO substrates. An In$_{0.02}$Ga$_{0.98}$N compound could be alloyed to exactly lattice-match LGO and Al$_{0.71}$Ga$_{0.29}$N compound could be exactly lattice-match LAO.

7.2 Si Substrates for GaN Epitaxy

It was shown that epitaxial GaN could be fabricated by a low-temperature MOCVD/HVPE deposition sequence in a hot-wall merged hydride reactor. Measurements revealed that a thin compliant SiO_x layer was an effective intermediate layer for growing GaN film epitaxially on Si. The GaN films had good adhesion and no films from optimized growths were observed to peel off the substrates. This represents the lowest deposition temperature known by this author to be reported for single crystal GaN by vapor phase epitaxy.

These encouraging results open a number of possible research opportunities. Results of LT-HVPE films transferred to the cold-wall MOVPE reactor for high-temperature growth are excellent. As the concept has been proven repeatedly, the next stage of research should be the fabrication of devices. A HEMT type structure could be fabricated in the sequence of 20 nm AlN or GaN buffer layer, 1 μm unintentionally doped (UID) GaN, 3 nm UID $Al_{0.2}Ga_{0.8}N$, 10 nm $Al_{0.2}Ga_{0.8}N$:Si, (~1x10^{18}cm^{-3}), 10 nm UID $Al_{0.2}Ga_{0.8}N$, 3 nm UID GaN. HEMT structures are relatively simple to grow yet they are practical devices. Performance of this HT-MOVPE/LT-HVPE/LT-MOCVD-GaN/Si structure would indicate if this sequence is a viable technique for producing other device structures.

In the merged-hydride system the investigation of AlN and AlGaN low-temperature epitaxy should be explored. Furthermore, due to the high vapor pressure of indium, InN and InGaN require deposition temperature lower than typically used for GaN. As low temperature growth of GaN has been proven, alloying GaN with indium may improve film quality. Finally, further encouraging results of III-nitride epitaxy on

two-inch silicon substrates may necessitate a reactor scale-up for growth on larger silicon substrates. To improve film uniformity in commercial HVPE, reactors often have a diameter much larger than the diameter of the substrate used for growth. This technique could be used to further improve film thickness uniformity of the GaN films on Si.

7.3 Thermal Stability of GaN

A challenge remaining for the further advancement of GaN processing technology is the prevention of degradation during device processing or operation, caused in part by dissociative sublimation and/or thermal decomposition of nitrides. This work reported the experimental investigation of the thermal stability of gallium nitride supported by a thermodynamic assessment of its thermal behavior. Evaluation of thermally treated GaN showed the dependence on pressure, ambient gas and annealing temperature. Specifically this work explained the structure and composition of the GaN surface, as well as how the surface science and kinetic barriers of GaN relate to GaN polarity.

This study should be continued to investigate the thermal stability of AlGaN/Al$_2$O$_3$ and GaN/Si samples to see if these films have the same temperature stability and vaporization mechanisms as the films studied here.

7.4 Polarity of GaN

The ability to grow thick HVPE GaN on sapphire followed by a backside etch to remove the substrate, resulting in large, free standing GaN has been demonstrated. Although it is difficult to minimize the damage to the backside of the GaN, it would be of interest to show that the backside of freestanding epitaxial films follows the mechanism of bulk grown samples in which the opposite surface of GaN shows opposite polarity.

It has been shown by Kryliouk *et al.* [134], and verified by Hellman *et al.* [70], that rough GaN grown on $LiGaO_2$ (O–face) is N-face, while smooth GaN grown on $LiGaO_2$ (cation–face) is Ga-face. The growth on $LiGaO_2$ does not require etching to separate the GaN film, thus preventing damage to the surface formed at the former substrate/GaN interface. Clearly this would represent an excellent opportunity to investigate how the two surfaces of the GaN film compare in terms of their polarities. The only limitation may be the size and quality of available $LiGaO_2$ substrates that may prevent grows sizable free-standing GaN that can easily be used for the characterizing the total polarity, and possibly the spontaneous and piezoelectric polarization. Ideally, free-standing GaN from $LiGaO_2$ should have minimal strain, resulting in a piezoelectric polarization close to zero.

Appendix A
Merged-Hydride Deposition System

Figures A-1, A-2, A-3 show the merged-hydride GaN deposition system. The main components are the chemical storage cabinets, gas handling lines, quartz reactor chamber, and furnace.

The typical carrier gas is nitrogen drawn from a ball of liquid nitrogen, or 100% hydrogen or 4% hydrogen (basis nitrogen) from cylinders stored external to the building. Cooling baths are located under the tabletop to allow up to three separate temperature-controlled bubblers to be connected into the system. Cylinders of HCl and NH_3 are stored adjacent to the system in a vented cabinet. The cabinets contain a hazardous gas detection system and a spare nitrogen cylinder that is used to flush the hazardous gas lines.

All of the gases pass through a set of quick-switching pneumatic valves. The valves allow the gas flow to develop in a separate vent line before being quickly switched to the main reactor. The quick-switching pneumatic valves also allow complex structures such as quantum wells to be grown. Additionally in the event of toxic chemical detection or power outage these valves are designed to switch off or "fail off" to cut off flow to the reactor. After the gas exits the reactor, it is sent through a dry scrubber before passing to the building exhaust/scrubber system.

As described elsewhere in this dissertation, the main reactor was recently scaled up to accept two-inch wafers. A load-lock is attached adjacent to the main chamber. The load-lock can be isolated from the system and pumped-and-purged through separate vacuum and nitrogen lines. A six-foot magnetic loading arm combined with the load-lock allows sample introduction without exposure to atmosphere.

The furnace contains six independent heating zones. The first two zones typically control the temperature of the inlet region and thus control the rate of reaction for GaCl formation. The middle two zones are located in the growth zone and define a temperature plateau region. The final two regions maintain a temperature level that ensures any unreacted chemicals are cracked before passing to the scrubber/exhaust.
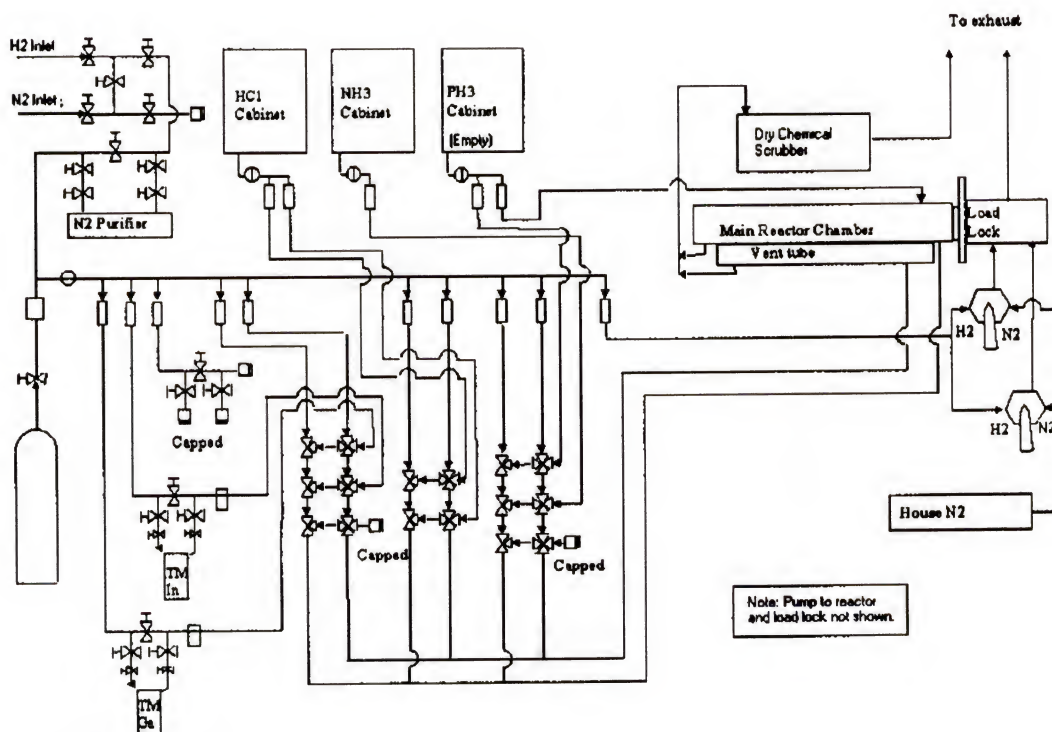

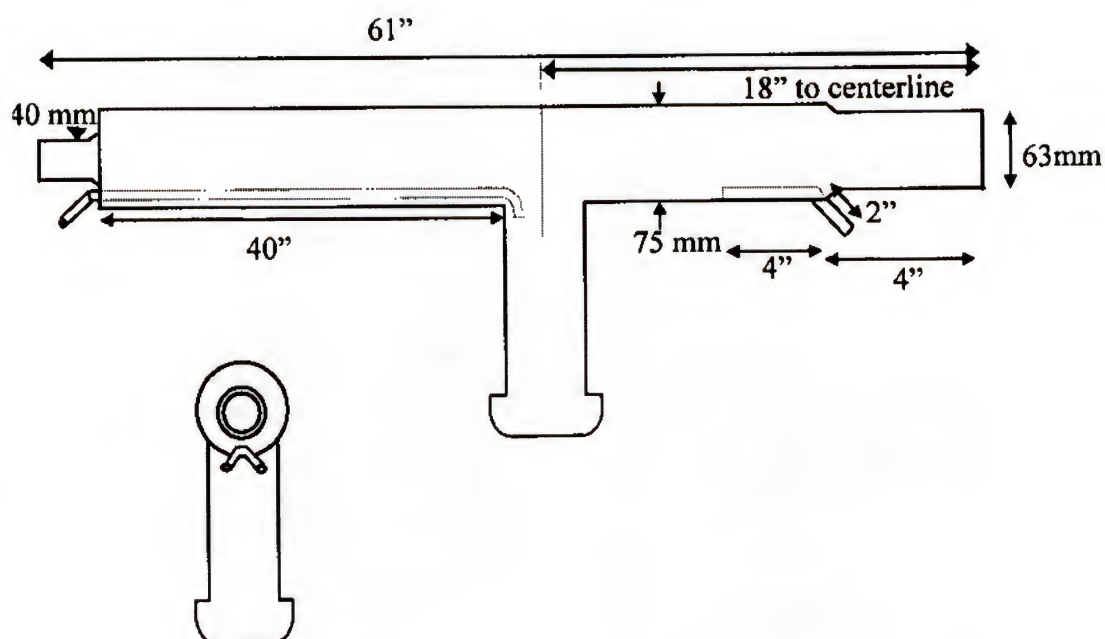Figure 2-1. Schematic of merged-hydride GaN deposition system [136]

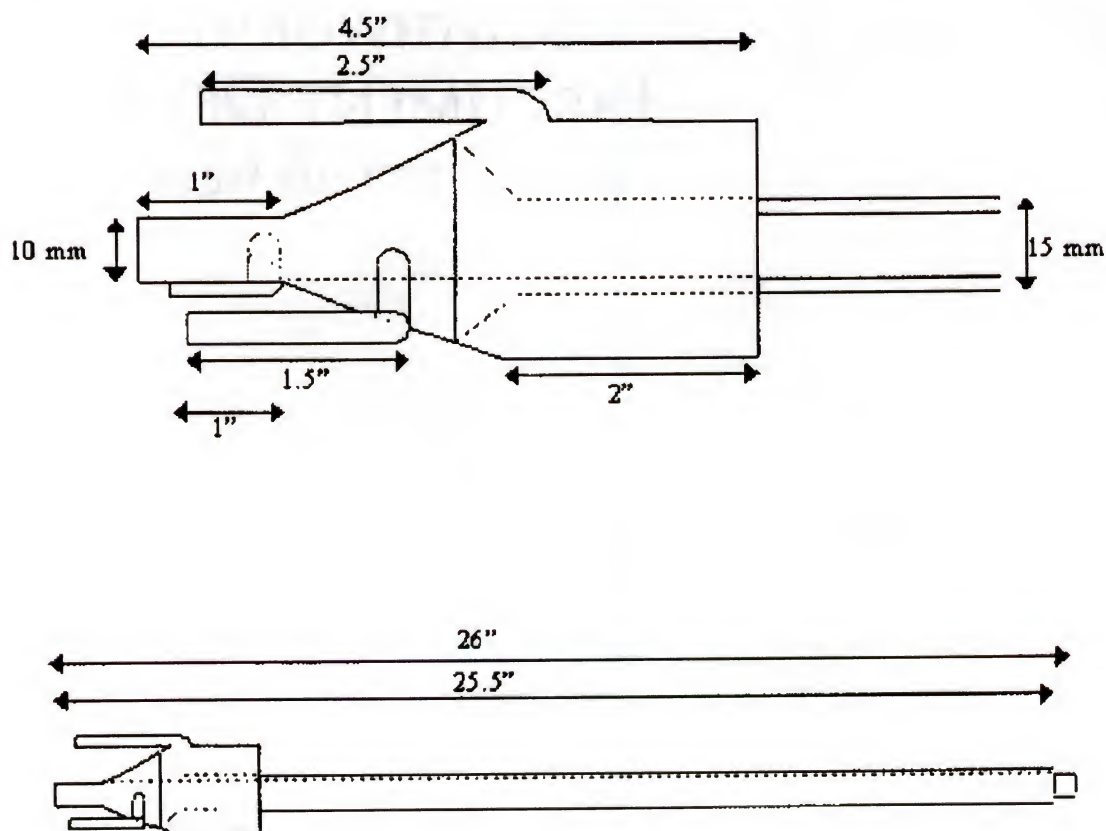Figure A-2. Merged-hydride main quartz reactor [136]

Figure A-3. Expanded view of reactor inlet [136]

Appendix B
High Temperature Electric Furnace

For the study of thermal stability of GaN it became necessary to construct an electric furnace. The author aided Visiting Professor Vladimir Demin (Moscow State University) in the design and construction of the furnace. Using this furnace we were able to attain a temperature of 1400 °C, much higher than attainable in the MOCVD and HVPE reactors (1000 °C). Additionally, the furnace with the attached vacuum was able to operate from 40 to 760 Torr. The overall design is pictured in figure B-1. Winding a wire around an 8" tube made the initial step. The core tube was quartz glass that has an acceptable extended-exposure temperature limit in air of 1300°C. If higher temperature is required, alternatives for the inner core are unglazed porcelain (1400°C), clay (1700°C), or Alundum tube (1900°C). The winding must be done carefully to ensure that kinks don't develop because these are points of stress that are likely to break when a voltage is applied across the wire. We initially attempted to use Nichrome wire that later failed at temperature above 870 °C. Using Chromel wire proved satisfactory in the temperature range we studied (up to 1400°C). At the ends of the tube additional wire was left to provide for connection. It was necessary to twist five wires together, giving the exposed wire higher resistance and thus lower temperature. Ideally the tube should be covered in asbestos to avoid shorting out the winding. For health reasons we searched for

alternatives. The best substance found was an alumina adhesive, a white paste substance that could be coated on.

The core was then inserted into a double shell cylinder (figure B-2). Near the core, the furnace was packed with high temperature, alumina wool insulation. The remaining packing was lower temperature and lower cost glass insulation. The thin air gap between the shells provided the final layer of insulation. This three-layer construction provided a low cost insulating barrier with a low thermal conductivity.
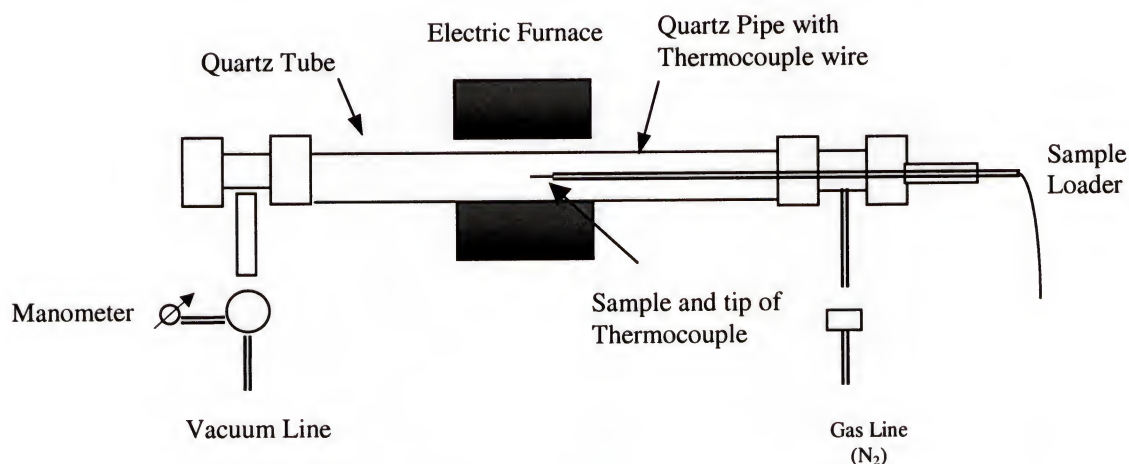
Figure B-1. Schematic of high temperature furnace

The exposed wires that formed the leads from the core were covered with sodium silicate (solid) insulation and feed out of the cylinder. These wires were connected to external wires which lead to a temperature controller or variac. Since the furnace was normally operated under vacuum conditions, heat transfer down the pipe by convection is negligible. Light rays travelling through the quartz pipe, however, are able to transfer heat from inside the furnace to the external pipe. This is undesirable because at the

quartz glass to metal connection is a viton gasket. With the furnace operating at 950 °C, the temperature at the viton gasket can reach 200°C, which would destroy the viton. The construction, shown in figures B-2 and B-3, reduced the temperature at the quartz glass to metal connection to 50 °C.
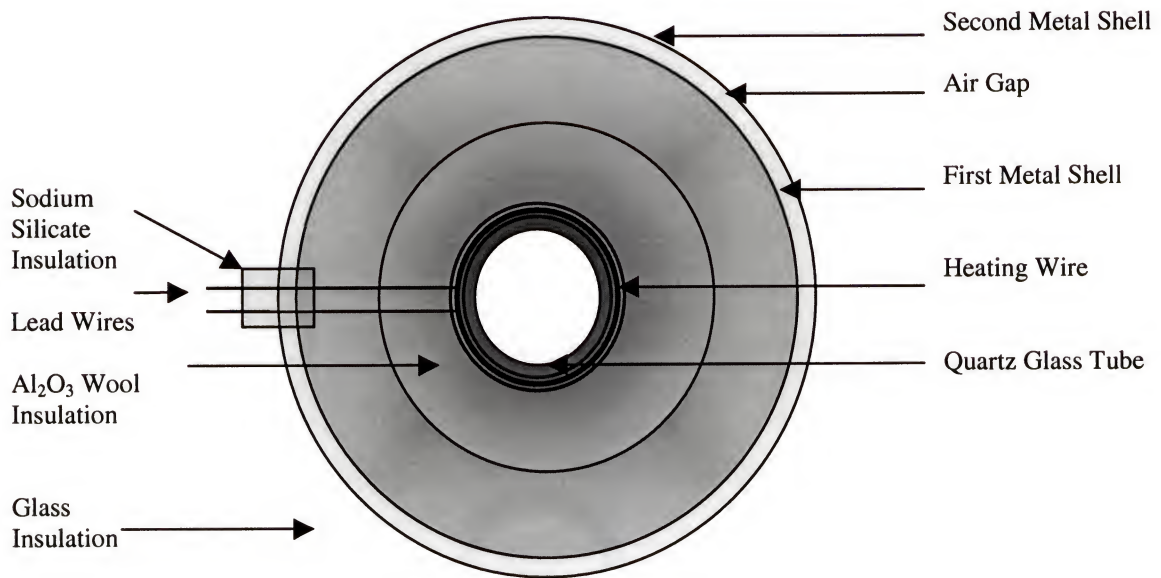

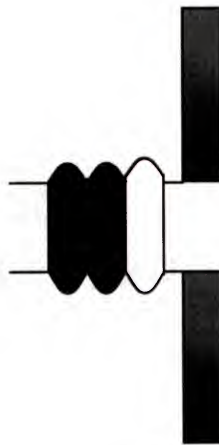Figure B-2. Cross-sectional view of high temperature furnace

Figure B-3. Blow-up of pipe at edge of furnace

Using quartz work, three humps were formed into the pipe near the furnace (figure B-3). The first hump was roughened on a diamond saw. Compared to the smooth surface of the quartz that normally internally reflects the light rays, the rough surface acts as a surface for the light rays to escape (figure B-4).

Light (Heat) Rays
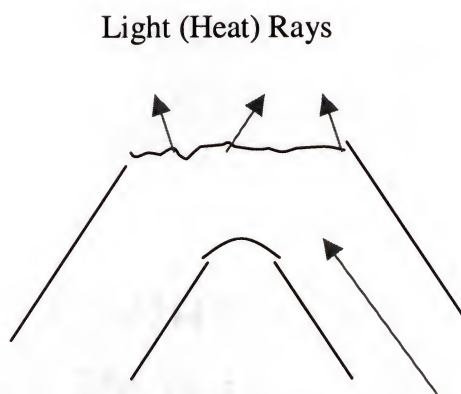
Figure B-4. Blow-up of figure B-3; bending and roughening of quartz pipe prevents heat transfer via light rays

The next two humps were also roughened and were coated under flame with $FeCl_3$ that reacted according to

$$FeCl_3^s + O_2^g \rightarrow FeO^s + \text{byproducts} \tag{B-1}$$

$$FeO^s + SiO_2^s \text{ (quartz glass)} \rightarrow (FeSiO_3)_x^s \text{ (black glass)} \tag{B-2}$$
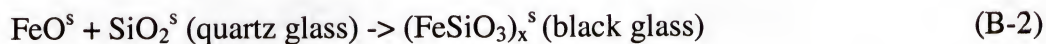
The $FeSiO_3$ coating acts to absorb additional light particularly IR radiation.

The quartz inside the furnace is subjected to temperatures in the range 900 °C to 1000 °C. In this range quartz glass can decompose into β-quartz and more favorably into α-quartz,

$$SiO_2^{\text{quartz-glass}}(900 \text{ °C}) \rightarrow \alpha\text{-quartz}^{\text{transparent}}(1000 \text{ °C}) \rightarrow \beta\text{-quartz}^{\text{white}} \tag{B-3}$$

This mechanism is undesirable because α-quartz has a low resistivity at high temperatures to oxygen diffusion from the atmosphere (figure B-5). During high temperature work a white film was noticed to form on the outside of the quartz tube.
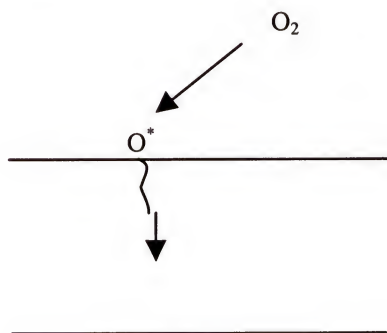
Figure B-5. α-quartz is highly permeable to oxygen diffusion

This can be explained by the reaction.

$$SiO_2^s \ (700 \ °C) + NaCl^s -> \beta\text{-quartz}^s \tag{B-4}$$

This reaction is advantageous because β-quartz that forms on the surface of the quartz glass is resistive to oxygen diffusion at high temperatures. The source of NaCl is from the operator who typically handles the quartz without gloves.

Work in a quartz glass furnace is limited to less than 1300 °C due to this reaction

$$SiO_2^s + \text{ambient air} \ (1300 \ °C) -> \gamma\text{-quartz}^s \tag{B-5}$$

The γ-quartz forms crystals that penetrate into the surface of the amorphous quartz glass. The quartz glass and the γ-quartz have a large difference in coefficient of thermal expansion. This leads to cracking in the quartz glass surface upon cooling.

APPENDIX C
CHARACTERIZATION TECHNIQUES

Scanning Electron Microscopy (SEM). (JEOL 35CF) In SEM, an electron beam is focused into a fine probe and raster scanned over a small rectangular area of the sample. This interaction with the sample creates various signals including secondary electrons, backscattered electrons, Auger electrons, characteristic x-rays, photoelectrons and internal currents. To image the surface, the secondary electrons are detected in either a scintillator photo multiplier tube or a partially depleted n-type silicon diode coated with a gold film. The signal produced by the detectors is relayed to a cathode ray tube in synchronization with the electron beam raster pattern. The image generated is similar to what is seen in an optical microscope, however, an SEM has a large depth of focus and a lateral resolution of 1 nm to 50 nm [167].

Energy-Dispersive X-Ray Spectroscopy (EDS). Typically EDS spectrometers are attached to an electron column instrument such as an SEM system. In EDS, elemental analysis is measured by examining the characteristic x-rays emitted when an electron beam strikes a sample. Each element present in the sample produces a characteristic x-ray with a unique energy. The characteristic x-rays enter a solid-state detector, usually lithium-drifted silicon. The x-rays that enter the detector are converted into signals that are processed into an energy histogram. Each peak in the spectrum corresponds to a particular element and the size of the peak is proportional to the concentration of the

element. EDS provides quantitative elemental analysis within 5% and lateral resolution of approximately 0.5 μm [167].

Transmission Electron Microscopy (TEM). (JEOL 200CX, JEOL 4000FX) In TEM, a finely focused, monoenergetic electron beam encounters a thin (< 200 nm) solid sample. This high-energy beam (100 KeV to 1 MeV) propagates through the sample then impacts a florescent screen where an image is observable. In crystalline material, the planes of atoms can diffract the electron beam such that a diffraction pattern is imaged on the screen. Seen as a series of dots and/or rings, this diffraction pattern gives information on the crystalline quality of the sample and the phases present. This image is referred to as selected area diffraction (SAD).

Alternatively changing the focus of the electron beam can produce a picture of the sample [167]. Atomic contract and non-homogenous crystallinity cause contrast in the picture. In high-resolution (HRTEM) systems, lateral resolution of up to 0.2 nm can be achieved, allowing atomic imaging.

Atomic Force Microscopy (AFM). (Digital Instruments Nanoscope III) Atomic force microscopy provides a representation of the topography and surface characteristics of a material down to the atomic level. A sharp tip located within a few angstrom of the surface scans the sample. Interatomic forces between the surface atoms of the sample and the tip cause a deflection of the cantilever tip. The magnitude of this deflection of the cantilever provides a measure of the sample height. A topographical map is produced by raster scanning the tip across the sample surface [167].

Auger Electron Spectroscopy (AES). (Perkin-Elmer 660) Auger Electron Spectroscopy uses a focused electron beam to stimulate excitation of Auger electrons near

the surface of a solid sample. The electron beam ejects inner shell electrons. An ejected electron is replaced with an electron from a higher shell. This rearrangement leaves the atom in an energetic state that is relieved by the emission of an Auger electron or a characteristic x-ray. The energy of the Auger electron (or characteristic x-ray) is determined by the energy separation of the orbital, which is unique to each element. Only the top 3-4 atomic layers are analyzed due to the small escape length (small energy) of an Auger electron. When combined with an ion sputter gun to gradually remove the surface, AES can provide a depth profile of elemental concentration. The lateral resolution of AES is approximately 50 nm. Since hydrogen and helium have one orbital, they cannot produce Auger electrons and therefore are not detected in AES [167].

X-Ray Photoelectron Spectroscopy (XPS) / Electron Spectroscopy for Chemical Analysis (ESCA). (Perkin Elmer Phi 5100, VG Scientifics, Ltd. ESCALAB 250 XPS Spectrometer) X-Ray photoelectron spectroscopy uses a monoenergetic soft x-ray beam to stimulate the excitation of photoelectrons from the surface of the sample. The x-ray source is an Al- or Mg-coated anode struck by high voltage electrons to produce Al kα and Mg kα radiation lines. The kinetic energy of the photoelectron is the difference between the energy of the x-ray probe and the binding energy of the electron. The peaks in photoelectron energy spectrum reveal the elements present and the relative elemental concentration is known by the intensity of the peaks. Electron binding energies are dependent on the chemical state of the atom, i.e., atomic bonding. ESCA is an extension of XPS in which the shape and position of the peaks are analyzed to determine how the excited atom is bonded. In XPS the x-ray beam is large (~ 1 cm^2) thus limiting

lateral resolution. Only the top 3-4 atomic layers are analyzed due to the small escape length (small energy) of a photoelectron [167].

The system was operating under these measurement conditions: X-ray source: 15 kV, 150 W; Wavelength: λ=1.542 Å (Cu Kα1); Detector: CCD; Resolution: 0.45 eV; Ar+ sputtered thickness (after etching): 40~50 Å.

X-ray Diffractometer (XRD). (Philips APD 3720, Philips MPD 1880, X'Pert PRO-MNR) In XRD a collimated beam of x-rays (λ = 1.542 Å) is diffracted by the crystalline phases in the specimen according to Bragg's law ($n\lambda = 2d \sin \theta$, where d = distance between the atomic planes). An intensity spectrum of the diffracted x-rays as a function of θ is generated. This diffraction pattern identifies the phases present in the sample and measures structural properties including strain, grain size, phase composition, orientation, and defect structure. A high-resolution system (HRXRD) provides more detailed information on the structural properties of epitaxial layers and highly oriented thin films [167].

The system was operating under these measurement conditions: X-ray generator: 3 kW; LiF-Cu Anode; 4-bounce crystals (Ge(220), Ge(440), Ge(220)-Asy.); Analyzer Crystal (3 bounce Ge(220)); Eulerian cradle; Graded multi-layer mirror.

Raman Spectroscopy. (Renishaw System-2000) In Raman spectroscopy a monochromatic line from a gas laser produces inelastic light scattering that results from the vibrational excitation of molecular and crystalline materials. Raman reveals information on structure and strain of molecules and crystals by observing the position and shifts of the vibrational frequencies of chemical bonds [167].

The system was operating under these measurement conditions: Laser output power: 20 mW; Excitation wavelength: 514.532 nm; Focused beam size: 2 μm; Detector: CCD; Accumulation time: 10 sec; Objective lens: 50 X; Increment size: 1 cm^{-1}.

Photoluminescence (PL) (SPEX 750M) In PL, laser light induces excitation and subsequent relaxation of electronic states in the sample to measure physical and chemical properties. The spectral distribution and time dependence of the emission is measured by the combination of an optical spectrometer and a photodetector [167].

The system was operating under these measurement conditions: single monochromator; Excitation source: He-Cd laser 325 nm; Power: 50 mW; Power Density: 3 W/cm^2; Detector: multi-alkali photomultiplier tubu(PMT); Incremeant: 15 Å.

Secondary Ion Mass Spectometry (SIMS). In SIMS, a solid sample under vacuum is sputtered with a narrow beam of ions called primary ions. These ions are of sufficient energy to eject surface atoms and clusters from the sample surface. The ejected atoms, known as secondary ions are separated in a mass spectrometer according to their mass-charge ratio. Qualitative information on secondary ion concentration is provided by the mass spectrum. Trace impurity analysis down to 10^{12} to 10^{16} atoms/cc is possible with SIMS [167].

Hall Effect. The most common technique to measure the carrier concentration is by Hall effect analysis. Typically an electric field is applied across the x-axis and a magnetic field is applied across the z-axis. For p-type material, the Lorentz force qv_x X B_z exerts a -y force on the holes. The -y directed current causes holes to accumulate at the bottom of the sample, which causes an electric field, E_y. This electric field exactly balances the Lorentz force. This Hall field is measured externally while the applied

magnetic field is varied. The Hall mobility is a function of the conductivity and Hall coefficient. Provided one type of carrier dominates, the carrier concentration can be calculated [119].

REFERENCES

1. S. C. Jain, M. Willander, J. Narayan, R. Van Overstraeten, J. of Appl. Phys. **87**, 965 (1998)

2. J. I. Pankove, GaN and Related Materials, edited by S. J. Pearton, Gordon and Breach, New York, 1 (1997)

3. B. Monemar, The Second International Conference on Nitride Semiconductors, Institute of Physics, Bristol, England (1997)

4. S. C. Binari, H. C. Dietrich, GaN and Related Materials, edited by S. J. Pearton, Gordon and Breach, New York, 509 (1997)

5. H. Morkoç, B. Sverdlov, G.-B. Gao, Proc. IEEE **81**, 493 (1993)

6. L. Pfeiffer, K. W. West, H. L. Stormer, K. W. Baldwin, Appl. Phys. Lett. **55**, 1888 (1989)

7. B. Gelmont, K. Kim, M. Shur, J. Appl. Phys. **74**, 1818 (1993)

8. A.S. Grove, Physics and Technology of Semiconductor Devices, Wiley, New York (1967)

9. S.P. DenBaars, S. Keller, Semiconductors and Semimetals: Vol. **50**, Gallium Nitride I, Academic Press, New York (1998)

10. O. Ambacher, J. of Phys. D **31**, 2653 (1998)

11. J. Sun, J. Redwing, T. Kuech, Phys. Stat. Sol. (a) **176**, 693 (1999)

12. E. Aujol, J. Napierala, A. Trassoudaine, E. Gil-Lafon, R. Cadoret, J. Crystal Growth **222**, 538 (2001)

13. V.S. Ban, J. Electrochem. Soc. **119**, 761 (1972)

14. R. Cadoret, J. Crystal Growth **205**, 123 (1999)

15. W. C. Johnson, J. B. Parsons, M. C. Crew, J. Phys. Chem. **36**, 256 (1932)

16. E. Ejder, J. Crystal Growth **22**, 44 (1974)

17. R. Juza, H. Hahn, Z. Anorg, Allg. Chem. **234**, 282 (1938)

18. H. Grimmeiss, Z. Koelmans, Nature **14a**, 264 (1959)

19. H.P. Maruska, J.J. Tietjen, Appl. Phys. Lett. **15**, 327 (1969)

20. H. M. Manasevit, F.M Erdmann, W.I. Simpson, J. Electrochem. Soc. **118**, 1273 (1975)

21. H. Gotoh, T. Suga, H. Suzuki, M. Kimata, Jpn. J. Appl. Phys. **20**, L545 (1981)

22. S. Yoshida, S. Misawa, S. Gonda, Appl. Phys. Lett. **42**, 427 (1983)

23. H. Amano, I. Akasaki, T. Kozawa, K. Hiramatsu, N. Sawak, K. Ikeda, Y. Ishi, J. Lumin. **40/41**, 121 (1988)

24. H. Amano, N. Sawaki, I. Akasaki, Y. Toyoda, Appl. Phys. Lett. **48**, 353 (1986)

25. I. Akasaki, H. Amano, T. Kozawa, K. Hiramatsu, N. Sawaki, K. Ikeda, Y. Ishii, J. Lumin. **40/41**, 129 (1988)

26. H. Amano, M. Kito, K. Hiramatsu, I. Akasaki, Jpn. J. Appl. Phys. **28**, L2112 (1989)

27. I. Akasaki, H. Amano, Tech. Dig. Int. Electron. Devices Meet. **96**, 231 (1996)

28. I. Akasaki, H. Amano, I. Suemune, Inst. Phys. Conf. Ser. **142**, 7 (1996)

29. I. Akasaki, H. Amano, GaN and Related Materials I, edited by J. I. Pankove T. D. Moustakas, Academic Press, New York, 459 (1998)

30. H. Amano, T. Asahi, I. Akasaki, Jpn. J. Appl. Phys. **29**, L205 (1990)

31. S. Nakamura, Appl. Phys. Lett. **64**, 1687 (1994)

32. S. Nakamura, G. Fasol, The Blue Laser Diode, Springer, Heidelberg (1996)

33. S. Nakamura, Thin Solid Films **343**, 345 (1999)

34. G. Kamler, J. Zachara, S. Podsiad, L. Adamowicz, W. Gebicki, J. Crystal Growth **212**, 39 (2000)

35. C. Wetzel, D. Volm, B. Meyer, K. Pressel, S. Nilsson, E. Mokhov, P. Baranov, Appl. Phys. Lett. **65**, 1033 (1994)

36. A. Nikolaev, I. Nikitina, A. Zubrilov, M. Mynbaeva, Y. Melnik, V. Dmitriev, MRS Proceedings **595**, W6.5.1 (2000)

37. V. Soukhoveev, V. Ivantsov, Yu. Melnik, A. Davydov, D. Tsvetkov, K. Tsvetkova, I. Nikitina, A. Zubrilov, A. Lavrentiev, V. Dmitriev, Phys. Stat. Sol. (a) **188**, 411 (2001)

38. R. J. Molnar, W. Götz, L.T. Romano, N.M. Johnson, J. Crystal Growth **178**, 147 (1997)

39. W. Götz, L.T. Romano, J. Walker, N.M. Johnson, R.J. Molnar, Appl. Phys. Lett. **72**, 1214 (1998)

40. Kin-Man Yu, S.J.C. Irvine, A. Stafford, S.A. Rushworth, L.M. Smith, R. Kanjolia, J. Crystal Growth **221**, 246 (2000)

41. R.A. Fischer, A. Wohlfart, A. Devi, W. Rogge, MRS Proceedings **595**, W3.18.1 (2000)

42. J. Narayan, P. Tiwari, X. Chen, R. Chowdhury, T. Zheleva, Appl. Phys. Lett. **61**, 1290 (1990)

43. J. Narayan, U. S. Patent No. 5406123 (1995)

44. K. Dovidenko, S. Oktyabrsky, J. Narayan, M. Razeghi, J. Appl. Phys. **79**, 2439 (1996)

45. J. Narayan, K. Dovidenko, A. Sharma, S. Oktyabrsky, J. Appl. Phys. **84**, 2597 (1998)

46. F. A. Ponce, MRS Bull. **22**, 51 (1997)

47. S. Fischer, A. Gisbertz, B. K. Meyer, M. Topf , S. Koynov, I. Dirnstorfer, D. Volm, R. Uecker, P. Reiche, S. Ganschow Z. Liliental-Weber, Symp. Proc. EGN-1 (1996)

48. S. Nakamura, Appl. Surf. Sci. **113**, 689 (1997)

49. S. Nakamura, Jpn. J. Appl. Phys. **30**, L1705 (1991)

50. S. Keller, D. Kapolnek, B. P. Keller, Y. Wu, B. Heying, J. S. Speck, U. K. Mishra, S.P. DenBaars, Jpn J. Appl. Phys. **35**, L285 (1996)

51. H. Kawakami, K. Sakurai, K. Tsubouchi, N. Mikoshiba, Jpn. J. Appl. Phys. **27**, L161 (1988)

52. A. Yamamoto, M. Tsujino, M. Ohkubo, A. Hashimoto, J. Crystal Growth **137**, 415 (1994)

53. A. Kikuchi, H. Hoshi, K. Kishino, Jpn. J. Appl. Phys. **33**, 688 (1994)

54. T. D. Moustakas, T. Lei, R. J. Molnar, Physica B **185**, 39 (1993)

55. K. Uchida, A. Watanabe, F. Yano, S. Kouguchi, T. Tanaka, S. Minagawa, J. Appl. Phys. **79**, 3487 (1996)

56. B-Y. Tsaur, R. W. McClelland, J. C. Fan, R. P. Gale, J. P. Salerno, B. A. Vojak, C. O. Bozler, Appl. Phys. Lett. **41** 347 (1982)

57. D. Pribat, B. Gerard, M. Dupuy, P. Legagneux, Appl. Phys. Lett. **60**, 2144 (1992)

58. K. Kato, T. Kusunoki, C. Takenaka, T. Tanahashi, K. Nakajima, J. Crystal Growth **115**, 174 (1991)

59. O. Parillaud, E. Gil-Lafon, B. Gerard, P. Etienne, C. Pribat, Appl. Phys. Lett. **68**, 2654 (1996)

60. T. Fukui, S. Ando, Electron. Lett. **25**, 410 (1989)

61. S. Ando, T. Honda, N. Kobayashi, Jpn. J. Appl. Phys. **32**, L104 (1993)

62. T. S. Zheleva, O-H. Nam, D. M. Bremser, R. F. Davis, Appl. Phys. Lett. **71**, 2472 (1997)

63. Y. Kato, S. Kitamura, K. Hiramatsu, N. Sawaki, J. Crystal Growth **144**, 133 (1994)

64. A.V. Davydov, W.J. Boettinger, U.R. Kattner, T.J. Anderson, Phys. Stat. Sol. (a), **188**, 407 (2001)

65. H.L. Lukas, E.TH. Henig, B. Zimmerman, CALPHAD **1**, 225 (1977)

66. B. Sundman, B. Janson, J.O. Andersson, CALPHAD **9**, 153 (1985)

67. A. Strittmatter, A. Krost, M. Straßburg, V. Türck, and D. Bimberg, J. Bläsing and J. Christen, Appl. Phys. Lett. **74**, 1242 (1999)

68. S. A. Nikishin, N. N. Faleev, V. G. Antipov, S. Francoeur, L. Grave de Peralta, G. A. Seryogin, and H. Temkin, T. I. Prokofyeva and M. Holtz, S. N. G. Chu, Appl. Phys. Lett. **75**, 2073 (1999)

69. M. Holtz, M. Seon, O. Brafman, R. Manor, D. Fekete, Phys. Rev. B **54**, 8714 (1996)

70. E. S. Hellman, Z. Liliental-Weber, D. N. E. Buchanan, MRS Internet J. Nitride Semicond. Res. **2**, 30 (1997)

71. F. Semond, B. Damilano, S. Vézian, N. Grandjean, M. Leroux, and J. Massies, Appl. Phys. Lett. **75**, 82 (1999)

72. F. Semond, B. Damilano, S. Vézian, N. Grandjean, M. Leroux, J. Massies, Phys. Stat. Sol. (b), **216**, 101 (1999)

73. X. Zhang, S-J. Chua, W. Liu, P. Li, Appl. Phys. Lett. **74**, 1984 (1999)

74. X. Zhang, S-J. Chua, W. Liu, P. Li, Phys. Stat. Sol. (b), **216**, 307 (1999)

75. M. A. Sánchez-García, F. B. Naranjo, J. L. Pau, A. Jiménez, E. Calleja, and E. Muñoz, J. Appl. Phys. **87**, 1569 (2000)

76. A. Strittmatter, A. Krost, M. Straßburg, V. Türck, and D. Bimberg, J. Bläsing, Christen, Appl. Phys. Lett. **74**, 1242 (1999)

77. L. Wang, X. Liu, Y. Zan, J. Wang, D. Wang, D. Lu, Z. Wang, Appl. Phys. Lett. **72**, 109 (1998)

78. N. P. Kobayashi, J. T. Kobayashi, P. D. Dapkus, W.J. Choi, and A. E. Bond, X. Zhang, H. Rich, Appl. Phys. Lett. **7**, 3569 (1997)

79. K. H. Ploog, O. Brandt, H. Yang, B. Yang, A. Trampert, J. of Vac. Sci. & Tech. B **16**, 2229 (1998)

80. B. Yang, A. Trampert, O. Brandt, B. Jenichen, K. H. Ploog, J. of Appl. Phys. **83**, 3800 (1998)

81. A. J. Steckl and J. Devrajan, C. Tran and R. A. Stall, Appl. Phys. Lett. **69**, 2264 (1996)

82. A. J. Steckl, J. Devrajan, S. Tlali, H. E. Jackson, Appl. Phys. Lett. **69**, 3824 (1996)

83. C. Yuam, A.J. Steckl, M.J. Loboda, Appl. Phys. Lett. **64**, 3000 (1994)

84. Z. Yang, F. Guarin, I. W. Tao, and W. I. Wang, S. S. Iyer, J. of Vac Sci. & Tech. B **13**, 789 (1995)

85. Y. Nakada, I. Aksenov, Appl. Phys. Lett. **73**, 827 (1998)

86. P. Kung, D. Walker, M. Hamilton, J. Diaz, and M. Razeghi, Appl. Phys. Lett. **74**, 570 (1999)

87. T. S. Zheleva, Ok-Hyun Nam, M. D. Bremser, R. F. Davis, Appl. Phys. Lett. **71**, 2472 (1997).

88. A. Sakai, H. Sunakawa, A. Usui, Appl. Phys. Lett. **71**, 2259 (1997).

89. H. Marchand, J.P. Ibbetson, P. T. Fini, P. Kozodoy, S. Keller, S. DenBaars, J. S. Speck, U. K. Mishra, MRS Internet J. Nitride Semicond. Res. **3**, 3 (1998).

90. H. Marchand, X.H. Wu, J.P. Ibbetson, P.T. Fini, P. Kozodoy, S. Keller, J.S. Speck, S.P. DenBaars, U.K. Mishra, Appl. Phys. Lett. **73**, 747 (1998).

91. O-H Nam, M.D. Bremser, T.S. Zheleva, R.F. Davis, Appl. Phys. Lett. **71**, 2638 (1997).

92. A. Sakai, H. Sunakawa, A. Usui, Appl. Phys. Lett. **73**, 481 (1998).

93. H. Marchand, N. Zhang, L. Zhao, Y. Golan, S. J. Rosner, G. Girolami, Paul T. Fini, J.P. Ibbetson, S. Keller, S. DenBaars, J. S. Speck, U. K. Mishra, MRS Internet J. Nitride Semicond. Res. **4**, 2 (1999).

94. K.J. Linthicum, T. Gehrke, D.B. Thomson, K.M. Tracy, E.P. Carlson, T.P. Smith, T.S. Zheleva, C.A. Zorman, M. Mehregany, R.F. Davis, MRS Internet J. Nitride Semicond. Res. **4S1**, 9 (1999)

95. A. Trampert, Semiconductors and Semimetals: Vol. **50**, Gallium Nitride I, Academic Press, New York (1998)

96. E. S. Hellman, MRS Internet Journal of Nitride Semiconductors **3**, 11 (1998)

97. T. Sasaki, T. Matsuoka, J. Appl. Phys. **64**, 4531 (1988)

98. M. Asif Khan, J. N. Kuznia, D. T. Olson, R. Kaplan, J. Appl. Phys. **73**, 3108 (1993)

99. E. S. Hellman, Mater. Res. Soc. Symp. Proc. **395**, N3.38 (1996)

100. Z. Liliental-Weber, S. Ruvimov, Ch. Kisielowski, Y. Chen, W. Swider, J. Washburn, N. Newman, A. Gassmann, X. Liu, L. Schloss, E. R. Weber, I. Grzegory, M. Bockowski, J. Jun, T. Suski, K. Pakula, J. Baranowski, S. Porowski, H. Amano, I. Akasaki, Mater. Res. Soc. Symp. Proc. **395**, 351 (1996)

101. F.A. Ponce, D.P. Bour, W.T. Young, M. Saunders, J.W. Steeds, Appl. Phys. Lett. **69**, 337 (1996)

102. X. H. Wu, D. Kapolnek, E. J. Tarsa, B. Heying, S. Keller, B. P. Keller, U. K. Mishra, S. P. DenBaars, J. S. Speck, Appl. Phys. Lett. **68**, 1371 (1996)

103. P. Vermaut, P. Ruterana, G. Nouet, Phil. Mag. A **76**, 1215 (1997)

104. E. S. Hellman, D. N. E. Buchanan, D. Wiesmann, I. Brener, MRS Internet J. Nitride Semicond. Res. **1**, 16 (1996)

105. F. Hamdani, A. E. Botchkarev, H. Tang, W. Kim, H. Morkoç, Appl. Phys. Lett. 71, 3111-3113 (1997)

106. M. Nagahara, S. Miyoshi, H. Yaguchi, J. Cryst. Growth **145**, 197 (1994).

107. J. W. Yang, J. N. Kuznia, Q. C. Chen, M. Asif Khan, T. George, M. DeGraef, S. Mahajan, Appl. Phys. Lett. **67**, 3759 (1995)

108. T. S. Cheng, C. T. Foxon, N. J. Jeffs, O. H. Hughes, B. G. Ren, Y. Xin, P. D. Brown, C. J. Humphreys, A. V. Andranov, D. E. Lacklison, J. W. Orton, M. Halliwell, MRS Internet J. Nitride Semicond. Res. **1**, 32 (1996)

109. T. Sasaki, T. Matsuoka, J. Appl. Phys. **64**, 4531 (1998)

110. J. L. Weyher, S. Müller, I. Grzegory, S. Porowski, J. Cryst. Growth **182**, 17 (1997)

111. J. L. Weyher, S. Muller, I. Grzegory, and S. Porowski, J. Cryst. Growth **182**, 17 (1997)

112. G. Nowak, S. Krukowski, I. Grzegory, S. Porowski, J.M. Baranowski, K. Pakula, J. Zak, MRS Internet J. Nitride Semicond. Res. **1**, 5 (1996)

113. C. J. Sun, P. Kung, A. Saxler, H. Ohsato, E. Bigan, M. Razeghi, D. K. Gaskill, J. Appl. Phys. **76**, 236 (1994)

114. J. M. Baranowski, Z. Liliental-Weber, K. Korona, K. Pakula, R. Stepniewski, A. Wysmolek, I. Grzegory, G. Nowak, S. Porowski, B. Monemar, P. Bergman, Mater. Res. Soc. Symp. Proc. **449**, 393 (1997)

115. K. Rapcewicz, M. B. Nardelli, J. Bernholc, Phys. Rev. B **56**, 12725 (1997)

116. A. Kazimirov, G. Scherb, J. Zegenhagen, T. Lee, M. J. Bedzyk, M. K. Kelly, H. Angerer, and O. Ambacher, J. Appl. Phys. **84**, 1703 (1998)

117. J. M. Baranowski, Z. Liliental-Weber, K. Korona, K. Pakula, R. Stepniewski, A. Wysmolek, I. Grzegory, G. Nowak, S. Porowski, B. Monemar, P. Bergman, Mater. Res. Soc. Symp. Proc. **449**, 393 (1997)

118. U. Karrer, O. Ambacher, M. Stutzman, Appl. Phys. Lett. **77**, 2012 (2000)

119. S. M. Sze, Physics of Semiconductor Devices, Wiley, Singapore (1981)

120. W. Johnson, J. Parsons, M. Crew, J. Phys. Chem. **36**, 167 (1932)

121. A.W. Searcy, High Temperature Technology, Butterworths, London (1964)

122. R.C. Schoomaker, A. Buhl, J. Lemley, J. Phys. Chem. **69**, 3455 (1965)

123. C.D. Thurmond, R.A. Logan, J. Electrochem. Soc. **119**, 622 (1972)

124. R.A. Logan, C.D. Thurmond, J. Electrochem. Soc. **119**, 1727 (1972)

125. G. Jacob, R. Madar, J. Hallais, Mater. Res. Bull. **11**, 445 (1976)

126. O. Ambacher, M.S. Brandt, R. Dimitrov, T. Metzger, M. Stutzman, R.A. Fisher, A. Miehr, A. Bergmaier, G. Dollinger, J. Vac. Sci. Tech. B **14**, 3532 (1996)

127. M. Fortado, G. Jacob, J. Crystal Growth **64**, 257 (1983)

128. D.D. Koleske, A.E. Wickenden, R.L. Henry, M.E. Twigg, J.C. Culbertson, R.J. Gorman, Appl. Phys. Lett. **73**, 2018 (1998)

129. A. Pisch, R. Schimd-Fetzer, J. Crystal Growth **189/190**, 730 (1998)

130. J. Hong, J.W. Lee, J.D. MacKenzie, S.M. Donovan, C.R. Abernathy, S.J. Pearton, J.C. Zopler, Semicond. Sci. Technol. **12**, 1310 (1997)

131. T. Ishii, M. Mukaida, T. Nishihara, S. Hayashi, M. Shinohara, Jpn J. Appl. Phys. **37**, L672 (1998)

132. T. Ishii, J. of Crystal Growth **189/190**, 208 (1998)

133. A. Marino, R. Hanneman, J. Appl. Phys. **34**, 384 (1963)

134. O. Kryliouk, M. Reed, M. Mastro, T. Dann, T. Anderson, B. Chai, Electrochemical Society Proceedings **98-18**, 99 (1998)

135. M. Okada, Y. Higaki, T. Yanagi, Y. Shimizu, Y. Nanishi, T. Ishii, S. Miyazawa, J. Cryst. Growth **189/190**, 213 (1998)

136. M. Reed, Ph.D. Thesis, University of Florida (2001)

137. Y. F. Wu, B. P. Keller, P. Fini, J. Pusl, M. Le, N. X. Nguyen, C. Nguyen, D. Widman, S. Keller, S. P. Denbaars, U. K. Mishra UK, Electron. Lett. **33**, 1742 (1997)

138. Q. Chen, J.W. Yang, R. Gaska, M. Asif Khan, M.S. Shur, G.J. Sullivan, A.L. Sailor, J.A. Higgings, A.T. Ping, I. Adesida, IEEE Electron Dev. Lett. **19**, 44 (1998)

139. J. Burm, K. Chu, W.J. Schaff, L.F. Eastman, M. Khan, Q. Chen, J.W. Yang, M.S. Shur, IEEE Electron Dev. Lett. **18**, 141 (1997)

140. S. Nakamura, M. Senoh, S. Nagahama, N. Iwasa, T. Yamada, T. Matsushita, H. Kiyoku, Yasunobu Sugimoto, T. Kozaki, H. Umemoto, M. Sano, and K. Chocho, Jpn. J. Appl. Phys. **36**, L1568 (1997)

141. B.V. L'vov, Thermochimica Acta **360**, 85 (2000)

142. O. Kryliouk, M. Reed, M. Mastro, T. Anderson, and B. Chai, Phys. Stat. Sol. (a) **176-1**, 407 (1999)

143. A.V. Davydov, T.J. Anderson, Electrochemical Society Proceedings **98-18**, 38 (1998)

144. B. Hannay, Treatise on Solid State Chemistry, Plenum Press, New York (1976)

145. V.A. Ryabin, M.A. Ostroumov, T.F. Svit, Thermodynamic Characteristics of Substances, Hanbook, Khimiya, Leningrad (1977)

146. B.V. L'vov, Thermochimica Acta **333**, 13 (1999)

147. B.V. L'vov, Spectrochim Acta Part B **53**, 809 (1999)

148. A. Pisch, R. Schmid-Fetzer, J. Crystal Growth **187**, 329 (1998)

149. B.V. L'vov, Thermochimica Acta **360**, 91 (2000)

150. D. Behr, J. Wagner, J. Schneider, H. Amano, I. Akasaki, Appl. Phys. Lett. **68**, 2404 (1996)

151. P. Molinas-Mata, A.J. Shields, M. Cardona, Phys. Rev. B **47** 1866 (1993)

152. R. Swalin, Thermodynamics of Solids, Wiley, New York (1972)

153. R. Schoonmaker, A. Buhl, J. Lemle, J. Phys. Chem **69**, 3455 (1965)

154. C. Lou, G. Somorjai, J. Chem. Phys. **55**, 4554 (1971)

155. G. Somorjai, J. Lester, J. Chem. Phys. **43**, 1450 (1965)

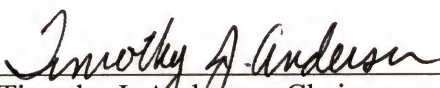156. L. Brewer J. Kane, J. Phys. Chem. **59**, 105 (1955)

157. R. Schoonmaker, A. Buhl, J. Lemley, J. Phys. Chem. **69**, 3455 (1965)

158. I. Grzegory, M. Bockowski, B. Lucznik, S. Krukowski, M. Wroblewski, S. Porowski, MRS Internet J. Nitride Semicond. Res. **1**, 20 (1996)

159. A. Adamson, Physical Chemistry of Surfaces, Interscience Publishers, New York (1967)

160. E. Guggenheim, J. Chem. Phys. **13**, 253 (1945)

161. N. B. Hannay, Treatise on Solid State Chemistry, Plenum Press, New York (1976)

162. J. J. Bikerman, Physical Surfaces, Academic Press, New York (1970)

163. G. Antonow, J. Chim. Phys. **5**, 372 (1907)

164. R. Defay, I. Prigogine, A. Bellemans, D. Everett, Surface Tension and Adsorption, Wiley, New York (1966)

165. CRC Handbook of Chemistry and Physics, CRC Press, Cleveland (2000)

166. A. Hines, R. Maddox, Mass Transfer: Fundamentals and Applications, Prentice-Hall, Englewood Cliffs, New Jersey (1985)

167. C. Brundle, C. Evans, S. Wilson, Encyclopedia of Materials Characterization (1992)

BIOGRAPHICAL SKETCH

Michael Anthony Mastro was born to Lois and Paul Mastro on April 10, 1975, in Louisville, KY. He grew up in Columbus, Ohio; South Bend, Indiana, and Greensboro, North Carolina before settling in upstate New York. Michael graduated from Pittsford (NY) Mendon High School in 1993. He then went on to the Johns Hopkins University in Baltimore, Maryland, where he graduated in 1997 with a Bachelor of Science in Chemical Engineering. While at Johns Hopkins, Michael performed two years of research in homogeneous nucleation under the advisement of Dr. Joseph L. Katz. Michael enrolled in a Ph.D. program at the University of Florida in the fall of 1997. Michael interrupted his study during the summer of 2000 to move to Phoenix, Arizona, to research silicon nitride deposition for Intel Corporation.

Michael has a sole sister, Lisa Dessecker, who lives with her family in Baltimore, Maryland.

I certify that I have read this study and that in my opinion it conforms to acceptable standards of scholarly presentation and is fully adequate, in scope and quality, as a dissertation for the degree of Doctor of Philosophy.
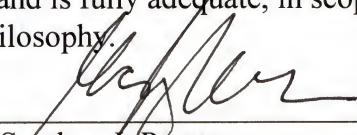
Timothy J. Anderson, Chairman
Professor of Chemical Engineering

I certify that I have read this study and that in my opinion it conforms to acceptable standards of scholarly presentation and is fully adequate, in scope and quality, as a dissertation for the degree of Doctor of Philosophy.
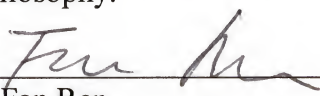
Cammy R. Abernathy
Professor of Materials Science and
    Engineering

I certify that I have read this study and that in my opinion it conforms to acceptable standards of scholarly presentation and is fully adequate, in scope and quality, as a dissertation for the degree of Doctor of Philosophy.

Stephen J. Pearton
Professor of Materials Science and
    Engineering

I certify that I have read this study and that in my opinion it conforms to acceptable standards of scholarly presentation and is fully adequate, in scope and quality, as a dissertation for the degree of Doctor of Philosophy.

Fan Ren
Professor of Chemical Engineering

This dissertation was submitted to the Graduate Faculty of the College of Engineering and to the Graduate School and was accepted as partial fulfillment of the requirements for the degree of Doctor of Philosophy.

December 2001

Pramod P. Khargonekar
Dean, College of Engineering

Winfred M. Phillips
Dean, Graduate School